TOKYO METROPOLITAN UNIVERSITY

PH.D. DISSERTATION

Time Dependent CAN Error Mitigation for EMI Noise of Switched-Mode Power Supplies

---

Author:
Ryo SHIRAI

Supervisor:
Prof. Keiji WADA

Power Electronics Laboratory
Department of Electrical Engineering and Computer Science
Graduate School of Systems Design

March 22, 2022

Acknowledgements

I would really like to to thank:

▷ **Prof. Keiji Wada**

For all of the discussions with you, for inspiring research motivations and working attitude, and for your daily supports during my 9-year lab life.

▷ **Prof. Toshihisa Shimmizu**

For your technical guidance, for teaching me essential mindsets as a researcher, and for your suggestion on my Ph.D. career.

▷ **Prof. Masahiro Yamaguchi**

For giving me proactive advice and comments on my Ph.D. dissertation, for taking the time to read my thesis, and for being a co-examiner of my Ph.D. dissertation.

▷ **Prof. Yukihisa Suzuki**

For teaching me basics of electromagnetic physics, and for being a co-examiner of my Ph.D. dissertation.

▷ **Prof. Satoshi Fukimoto**

For valuable discussions on CAN-related technologies, and for being a co-examiner of my Ph.D. dissertation.

▷ **At the Research Center for Energy Integrity Systems...**

Raito Matsuzaki and Koji Konomi, for your technical support, for teaching me basics in field of the informatics.

▷ **At the Power Electronics Research Institute of Zhejiang University...**

Prof. Mark Dehong Xu, Prof. Changsheng Hu, Prof. Henling Chen and many lab colleagues, for your daily support in China, for technical discussions, and teaching me a lot of Chinese culture and beautiful landscapes.

▷ **At the Ph.D Candidates of Power Electronics in Japan...**

Dr. Ryuji Iijima, Dr. Shunsuke Takuma, Dr. Kazuaki Tesaki, and many members, for your contributions to the team, and for giving me a lot of advice to being a representative.

▷ **At the Power Electronics Lab of Tokyo Metropolitan University...**

Prof. Hiroaki Matsumori, Prof. Shotaro Takahashi, Prof. Tomoyuki Mannen, Dr. Daiki Yamaguchi, Dr. Pin-Yu Huang, Dr. Yu Shan Cheng, Dr. Yoshihiro Miwa, Dr. Yu Yue, Dr. Yoshikazu Kuwabara, Dr. Van-Long Pham, Dr. Kazuki Matsubara, Dr. Shinichiro Hayashi, Koji Mitsui, Takaya Sekiguchi, Taro Takamori, Hisao Akiyama, Yoshio Bizen, Eiji Ikuta, Hirofumi Suda, Koji Takano, Katsuya Shingu, Kohei Yasuda, Shogo Matsuhisa, Hiroki Maeda, Kazuki Urata, Kensuke Suzuki, Ryutaro Sato, Taiki Onodera, Hiroki Masuko, Keigo Arita, Yumika Takeda, Ryota Shimamoto, Naoki Aoshima, Kyosuke Shimo, Dr. Riccardo Ruffo, and many colleagues, for your daily support, for being sincere friends, and for passing delightful moments with me.

▷ **In the world of power electronics...**

Dr. Joseph Kozak, for your contributions to the joint workshop of CPES and PPEJ, and for consulting my thesis title.

Prof. Heng Wu, Dr. Shih-Feng Chou, Prof. Huimin Wang, and Dr. Anatolii Tcai, for beneficial information exchange, and for being international friends.

Finally, my wife, parents, a brother, and grand parents, for making me everyday a better self, and for supporting me anytime. Again, I would like to appreciate families, colleagues, friends, supervisors, and everyone who have supported me to conduct this research.

This research was supported by JSPS (Japan Society for the Promotion of Science) KAKENHI Grant Number JP19J21468.

Abstract

Electromagnetic compatibility (EMC) is a major concern in modern electrical applications, such as EVs and industrial robots, where switched-mode power supplies (SMPSs) and serial communication networks operate in conjunction. SMPSs have gradually employed high-frequency and high-speed switching operations with the advent of wide bandgap semiconductor devices, which has resulted in the generation of more electromagnetic interference (EMI) noise. Moreover, for serial communication systems, high-speed and wide-bandwidth data transmission are common requirements for applications such as telecommunication, transportation, and industrial systems. To achieve the technical requirements under the robust operation, the noise immunity of communication systems is a significant concern. Hence, a large amount of effort has been implemented into suppressing electromagnetic disturbance on serial communication systems. In this context, SMPSs have been recognized as the main EMI sources that causes electromagnetic disturbance on communication systems. Therefore, this thesis covers a comprehensive study on EMC of a buck converter and controller area network (CAN) communication.

Chapter 1 presents the background and motivations for the research. After technological problems of EMC between SMPSs and serial communication systems are reviewed, Chapter 2 reviews the literature related to EMC of SMPSs and communication systems. First, the EMI noise of power electronics converters is reviewed, focusing on the conducted noise of a buck converter. State-of-the-art EMI reduction approaches for the conducted noise are described. Second, the overview of CAN summarizes the specification of standard CAN protocol and recent EMI research. Subsequently, case studies of the disturbance on serial communication systems concretize EMI problems and the potential risks are discussed.

Chapter 3 describes the time-domain analysis of the disturbance caused by a buck converter on CAN communication. As an experimental platform, the noise injection system is developed. The system consists of a buck converter and a CAN bus and it enables to perform experimental studies with high repeatability. within addition to experimental studies, simulation modeling methodologies are also discussed. In particularly, two types of parasitic impedance remain undeveloped regarding simulation modeling: parasitic impedance of an electrolytic capacitor and OFF-state MOSFET impedance. Accordingly, experimental and

simulation studies were performed to develop simulation models. Subsequently, simulation and experimental waveform comparisons of the noise injection system were performed to verify the modeling approach and unveil the mechanism of EM disturbance, followed by the CAN failure analysis.

Chapter 4 describes the time series control using an active gate driver to balance the EM disturbance reduction and converter performance. The active gate driver is one of the key technologies in controlling a switching speed of power semiconductor device. By suppressing the switching speed of the device, an EMI reduction can be achieved. However, this increases the switching power loss and results in lowering the conversion efficiency. That is, balancing the EMI reduction with the converter performance would be a technical challenge. The time series control of the active gate driver realizes an effective EMI reduction on CAN data transmission. For low-bus-traffic applications, the control method balances the EMI reduction and the conversion efficiency, which was studied experimentally.

Chapter 5 presents the timing-shift control of the buck converter that reduces the EMI using converter control. Unlike the conventional EMI reduction methods, the control scheme aims to prevent communication errors even if the buck converter induces a noise to the communication line. Despite the control suppressing the EM disturbance, shifting a switching timing potentially undermines the converter control stability. A duty compensation method is used to improve the stability.

Chapter 6, in contrast to the timing-shift control on the converter side, proposes the digital denoising technique that enables a CAN processor to digitally remove error signals. The denoising method can be applied to the communication system independently of the converter. To implement the denoising method to the noise injection system, a field programmable gate array (FPGA) is integrated with the CAN controller. The denoising process occurs on the FPGA, and the CAN controller receives the processed signals. Owing to the CAN sampling rule, modifying the communication protocol is not required. Finally, experimental results validate the denoising method. Chapter 7 provides the conclusions and future outlook of this research.

Publications

Journal Papers

1. Ryo Shirai, Toshihisa Shimizu, “Countermeasure to EMI caused by power converter on Controller Area Network,” *IEEJ Transactions on Industry Applications*, 2018, vol. 138, no. 8, pp. 713-714, Aug. 2018.
2. Ryo Shirai, Toshihisa Shimizu, “Time domain analysis of transmission failure on CAN system due to differential-mode noise emitted from a buck converter,” IEEJ Journal of Industry Applications, vol. 8, no. 4, pp. 608-614, July 2019.
3. Ryo Shirai, Keiji Wada and Toshihisa Shimizu, “Failure protection method for CAN communication against EMI noise generated by switched-mode power supplies," *IEEE Journal of Emerging and Selected Topics in Power Electronics*, vol. 9, no. 5, pp. 6152-6160, Oct. 2021.

International Conferences

1. Ryo Shirai and Toshihisa Shimizu, “Study on electromagnetic disturbance of buck chopper circuit into Controller Area Network communications,” *Symposium on Semiconductor Power Conversion 2017*, JP3, Taiwan, Oct. 2017.
2. Ryo Shirai and Toshihisa Shimizu, “Study of electromagnetic disturbance of buck chopper circuit into Controller Area Network communications,” *IEEE Workshop on Electronic Power Transmission and Distribution 2017*, E—poster session no. 11, Denmark, Nov. 2017.
3. Ryo Shirai and Toshihisa Shimizu, “Study of EMI Caused by Buck Converter on Controller Area Network,” *International Power Electronics Conference (IPEC-Niigata 2018 ECCE Asia)*, No. 0160, Japan, May 2018.
4. Ryo Shirai and Toshihisa Shimizu, “Failure protection for Controller Area Network against EMI emitted by buck converter,” *2019 IEEE Applied Power Electronics Conference and Exposition (APEC)*, CA, USA, March 2019.

5. Ryo Shirai and Toshihisa Shimizu, "Study on EMI failure of Controller Area Network caused by a buck converter," *2019 IEEE Energy Conversion Congress and Exposition (ECCE)*, MD, USA, Oct. 2019.
6. Ryo Shirai, Keiji Wada, Toshihisa Shimizu, and Dehong Xu "Suppressing EMI Noise to CAN Communication by Using Active Gate Driver," *2020 International Power Electronics and Motion Control Conferences (IPEMC)*, Online, 2020.
7. Ryo Shirai, Keiji Wada, and Toshihisa Shimizu, "CAN signal processing for EMI reduction cooperating with switched-mode power supply," *2021 IEEE Energy Conversion Congress and Exposition (ECCE)*, Online, 2021.
8. Ryo Shirai, Shinichiro Hayashi, and Keiji Wada, "Accurate MOSFET Modeling Approach with Equivalent Series Resistance of Output Capacitance for Simulating Turn-Off Oscillation," *2022 IEEE Applied Power Electronics Conference and Exposition (APEC)*, TX, USA, March 2022.

Domestic Conferences

1. Ryo Shirai, Toshihisa Shimizu, "Analysis of EMI noise caused by the stray capacitance of an electrolytic capacitor," *Joint Workshop on Electronic Devices and Semiconductor Power Conversion*, EDD—16—057, SPC—16—144, Fukuoka, Japan, Nov. 2016.
2. Ryo Shirai, Toshihisa Shimizu, Satoshi Fukumoto, Raito Matsuzaki, and Koji Konomi, "Basic study on the electromagnetic interference of semiconductor power converter to Controller Area Network," *2017 IEE-Japan Annual Meeting*, 4-141, Toyama, Japan, March 2017.
3. Ryo Shirai, "Analysis of the electromagnetic interference of power converter to CAN," *2017 IEE-Japan Industry Applications Society Conference*, R1-1, Hokkaido, Japan, Aug. 2017.
4. Ryo Shirai, Toshihisa Shimizu, "Basic study of a novel EMC solution for the electromagnetic interference of power converter to CAN," *Joint Workshop on Motor Drive and Semiconductor Power Conversion*, SPC—17—134, MD—17—085, Wakayama, Japan, Sep. 2017.
5. Ryo Shirai, Toshihisa Shimizu, Raito Matsuzaki, and Satoshi Fukumoto, "Electromagnetic interference on control communication network of power

converter," *2018 IEE-Japan Annual Meeting*, 4-114, Fukuoka, Japan, March 2018.

6. Ryo Shirai, Toshihisa Shimizu, "Cooperative control of buck converter for suppressing EMI on Controller Area Network," *2018 IEE-Japan Industry Applications Society Conference*, 1—74, Kanagawa, August 2018.

7. Ryo Shirai, Toshihisa Shimizu, "Study on differential and common mode interference on CAN communication caused by a buck converter," *Joint Workshop on Motor Drive and Semiconductor Power Conversion*, SPC—18—127, MD—18—087, Saga, Japan, Sep. 2018.

8. Ryo Shirai, Toshihisa Shimizu, "EMI suppression method using active gate driver for CAN communication," *Workshop on Semiconductor Power Conversion*, SPC—19—145, Tokyo, Japan, Nov. 2019.

9. Ryo Shirai, Keiji Wada, and Toshihisa Shimizu, "CAN signal processing cooperating with switching converter for EMI reduction," *2020 IEE-Japan Annual Meeting*, 4—079, Tokyo, Japan, March 2020.

10. Naoki Aoshima, Ryo Shirai, and Toshihisa Shimizu, "Analysis of noise waveform induced on CAN communication line by buck chopper circuit," *2020 IEE-Japan Annual Meeting*, 4—080, Online, March 2020.

11. Ryo Shirai, Keiji Wada, and Toshihisa Shimizu, "EMI reduction method for periodic noise of CAN communication line induced by power converters," *Joint Workshop on Electromagnetic Compatibility and Semiconductor Power Conversion*, SPC—20—190, EMC—20—060, Tokyo, Dec. 2020.

12. Naoki Aoshima, Ryo Shirai, and Keiji Wada, "A platform for verifying communication failures caused by high-frequency noise current generated by power conversion circuits on Ethernet communication," *2021 Joint Workshop on Electromagnetic Compatibility and Semiconductor Power Conversion*, EMC-21-038, SPC-21-158, Aichi, Japan, Dec. 2021.

13. Ryo Shirai, Keiji Wada, "CAN digital denoising technique for EMI derived from buck converter," *2021 Joint Workshop on Electromagnetic Compatibility and Semiconductor Power Conversion*, EMC-21-037, SPC-21-157, Aichi, Japan, Dec. 2021.

Contents

1 Introduction **1**
1.1 Background 1
1.2 Motivation 3
1.3 Research Objectives 6
1.4 Dissertation Outline 8

2 Literature Review **11**
2.1 EMI Noise of Power Electronics Converters 11
2.1.1 Basics on EMI of Power Electronics 11
2.1.2 EMC Standards for PE Converters 14
2.2 Overview of the Controller Area Network (CAN) 15
2.2.1 Specification of the CAN Protocol 15
2.2.2 EMI Solutions for CAN Communication Systems 17
2.3 EMC Standards for CAN 19
2.4 EM Disturbance on Communication Systems 21
2.5 Summary 22

3 Time-Domain Analysis of Electromagnetic Disturbance on CAN **23**
3.1 Introduction 23
3.2 Noise Injection System as an Experimental Platform 24
3.3 Simulation Model of the Noise Injection System 27
3.4 Modeling Methodologies: Parasitic Impedance of Capacitor 33
3.4.1 Introduction 33
3.4.2 Measurement of Conducted Noise Emission 33
3.4.3 Mechanism of Leakage Current through a Capacitor Clamp 38
3.4.4 Suppression of the Leakage Current 43
3.5 Modeling Methodologies: OFF-State Impedance of MOSFET 45
3.5.1 Introduction 45
3.5.2 Proposed MOSFET Simulation Model with R_{oss} 46

3.5.3 Mechanism of Damped Switching Oscillation 49
3.5.4 Experimental Verification of the Proposed MOSFET Model . 51
3.6 Comparison of Simulation and Experiment Waveforms 55
3.7 Time-Domain Analysis of the CAN Error Mechanism 59
3.8 CAN Error Rate Evaluation 60
3.8.1 Bit Error Rate 60
3.8.2 Measurement of Application Level Error 63
3.9 Summary 67

4 Time Series Control of Active Gate Driver 69
4.1 Introduction 69
4.2 Effects of Switching Waveform on CAN Error 70
4.3 Variable Switching Speed Gate Driver 73
4.3.1 Configuration of the Noise Injection System with Discrete Active Gate Driver 76
4.3.2 Active Gate Driver Impacts on CAN Error Rate 81
4.4 Summary 84

5 Time-Dependent Control of a Buck Converter for EMI Reduction 85
5.1 Start-Stop Synchronization Control 85
5.2 Timing-Shift Control (TSC) of a Buck Converter 89
5.2.1 Operation Principle of TSC 89
5.2.2 Experimental Verification 90
5.3 Timing-Shift Control with Pulse-Width Compensation Function . . 92
5.4 Summary 94

6 Digital Denoising Methods for the CAN Communication System 95
6.1 Synchronous Digital Denoising Method 95
6.2 Autonomous Digital Denoising Method 98
6.2.1 Implementation of the Denoising Method 98
6.2.2 Experimental Verification 100
6.3 Summary 101

7 Conclusion and Outlook 103
7.1 Conclusions of the Research 103
7.2 Future Outlook 104

Bibliography 107

Chapter 1

Introduction

1.1 Background

The harmonious cohabitation among electrical equipment is a key factor for their security and reliability. Owing to the increasing use of electrical equipment in human activities, there is a risk of harm to human beings. Thus, an engineering discipline called electromagnetic compatibility (EMC) has evolved to minimize the risk realistically and economically. Fig. 1.1 shows a categorization of EMC with sub-fields [1], [2]. EMC is divided into two fields: electromagnetic emissions (EMI) and electromagnetic susceptibility (EMS). They both have sub-fields that are classified by noise propagation mechanisms. In this thesis, a cross-category study enables us to understand the nature of electromagnetic disturbance because the phenomenon includes noise generation, propagation, and receipt.

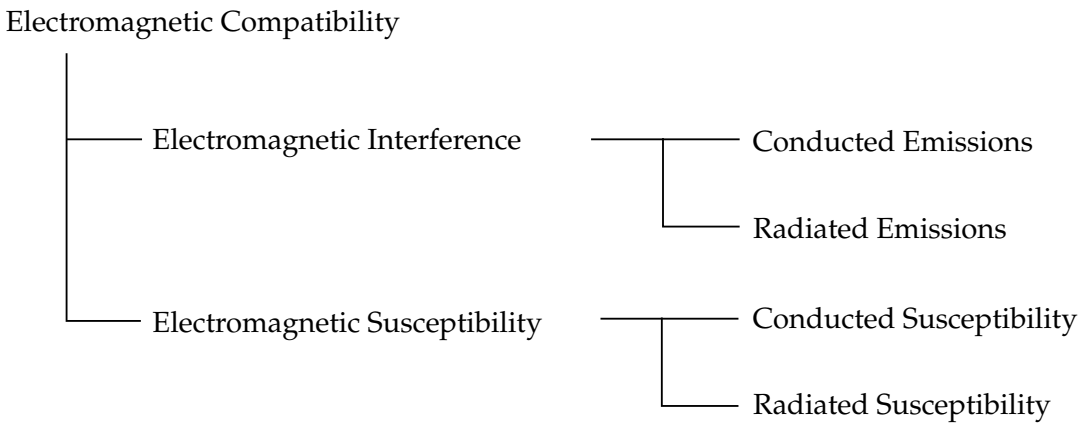

FIGURE 1.1: Sub-fields of electromagnetic compatibility

A power electronics (PE) converter is a significant source of EMI noise in modern electrical and electronic applications. Today, the progress in power semiconductors and circuit components enables the PE converter to operate at higher switching speeds and frequencies for cost and size reduction. This trend is accelerated particularly with the advent of wide-bandgap (WBG) power semiconductors such as SiC and GaN [3]–[5]. In addition, the switched-mode power supply (SMPS) often operates with a high current and voltage compared with other electronics circuits. These characteristics of the PE converter make the EMI reduction more challenging and costly. Moreover, this problem will worsen in the future because the EMI noise of PE converters is increasing and shifting to a higher frequency range.

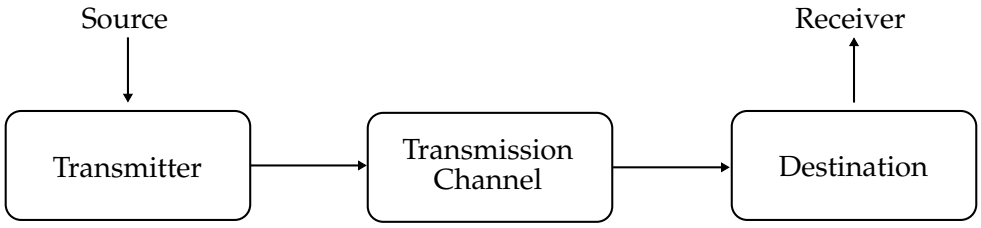

FIGURE 1.2: General topology of communication system

Fig. 1.2 shows a general topology of a serial communication system in which data is transmitted from a source to a destination. Serial communication systems have an essential role in the digitized and networked society. Their function is to transmit data among the nodes by sending bit strings. However, noise tolerance is frequently one of the concerns to ensure reliability since noise interferes with the signals in the transmission channel. If the serial communication system becomes disturbed by noise, it can cause a data transmission failure, which results in an operation delay, a halt, or even a malfunction. Therefore, EMI noise reduction and the improvement of noise tolerance are necessary for applications that require high robustness.

Considering the technological trends in PE converters and serial communication systems, PE converters may cause a disturbance in the serial communication systems, which perhaps will be more severe in the future. A system that integrates PE converters and serial communication systems, such as EVs and industrial robots, has internal electromagnetic couplings owing to the high-density

packaging. Furthermore, the widespread use of renewable energy sources and future e-Mobility will extend the application of such the integrated systems. From this context, EMI analysis and reduction are necessary for the system integrity.

1.2 Motivation

Historically, EMC problems have resulted in an accident or incident. For instance, in 2008, the Shonan Monorail in Japan caused an accident. Fig. 1.3 shows a photo of the rescue work after the accident. According to [6], the EMI noise emitted by the power supply of the inverter gate driver induced a conducted noise to a communication line, and the noise caused an illegal interruption of a CPU process. After the accident, the Japan Transport Safety Board (JTSB) recommended that railway companies and manufacturers share their EMC knowledge and take further measures to resolve the EMC problems.

FIGURE 1.3: Rescue work after the accident of Shonan Monorail [6]

In addition, Honda Motor Co., Ltd recalled more than 237,000 vehicles to repair a power supply system. According to [7], the conducted noise from the power supply affected the power control unit, which resulted in unintentional powering off of the meter panel and engine. To prevent the failure, Honda implemented a countermeasure using a clamp filter that minimized the conducted noise (Fig. 1.4).

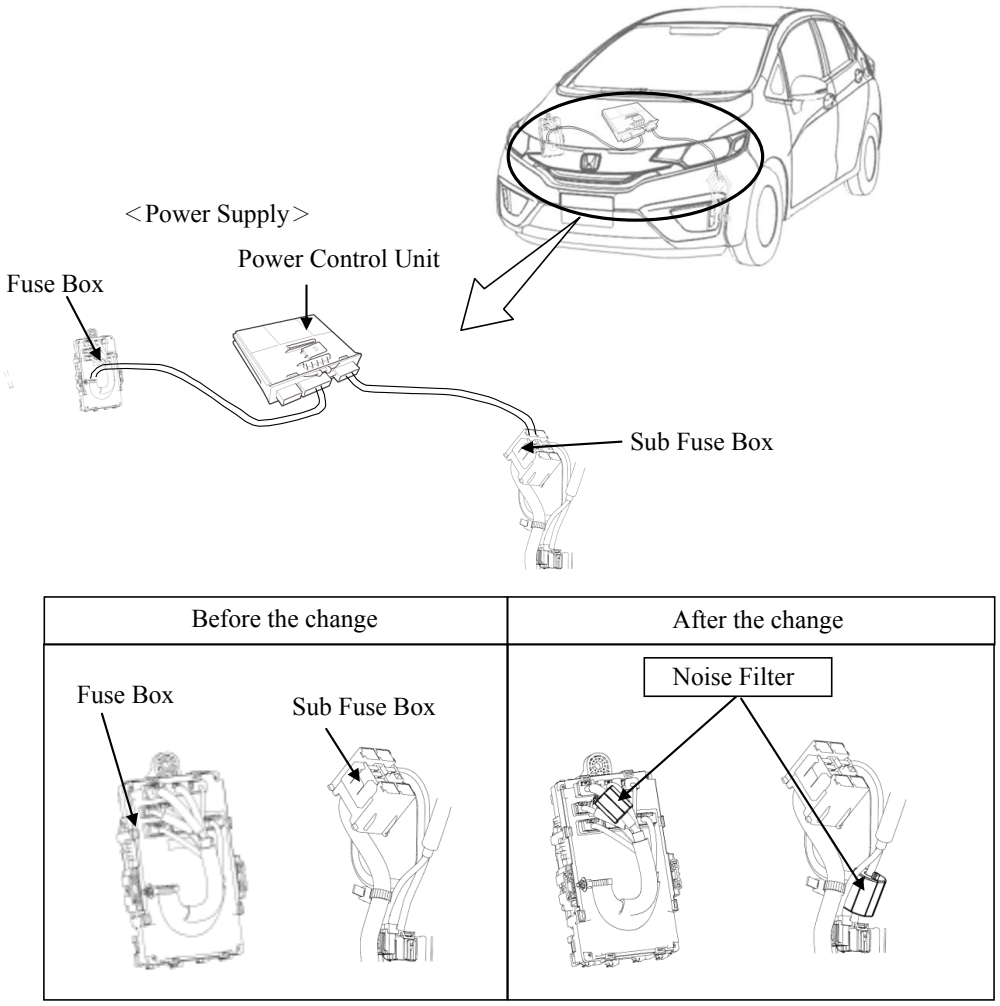

FIGURE 1.4: From Honda Motor recall report [7]

In addition to the above examples, there are many cases of EM disturbance on communication systems [8]. As observed, the disturbance on communication systems can cause harmful accidents and significant social impacts. From this perspective, EMC solutions have been taken a keen interest in minimizing the risk of EM disturbance.

Fig. 1.5 depicts a typical mechanism of EM disturbance on a serial communication system based on the literature survey of this research. Power cables in which a conducted noise from a PE converter flows often have an EM coupling with a serial communication line. Because of the coupling, conducted noise is induced into the serial communication line, resulting in a signaling error.

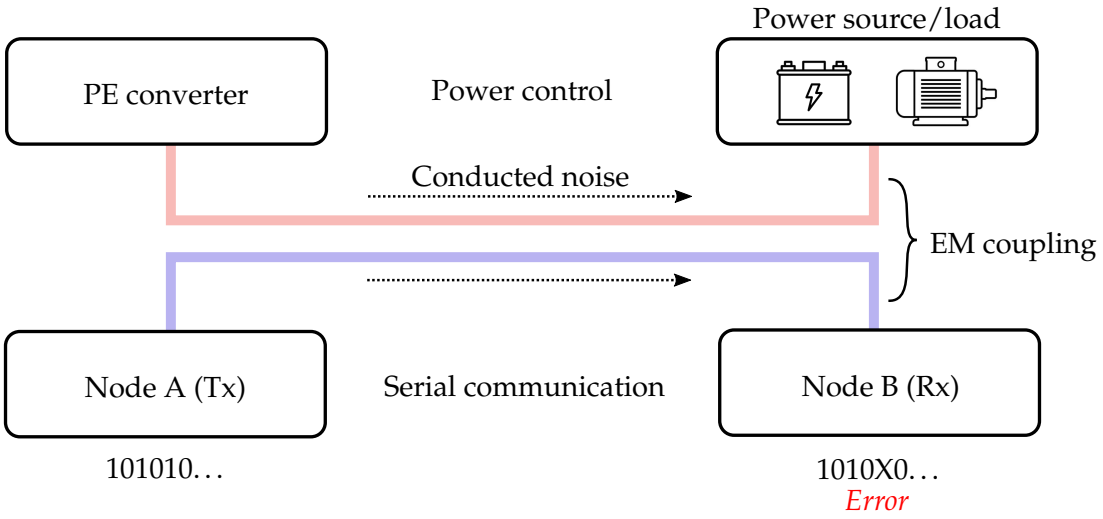

FIGURE 1.5: EM disturbance on a serial communication system

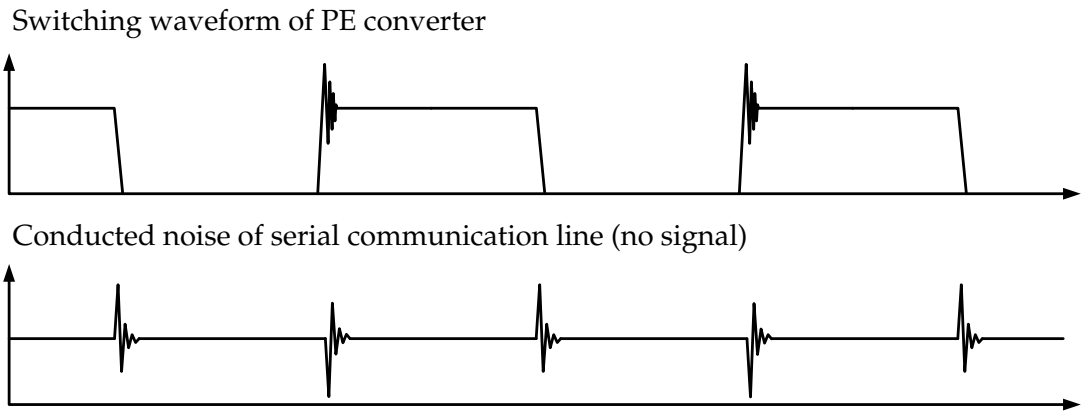

FIGURE 1.6: Conducted noise waveform in the time domain

Fig. 1.6 shows a conducted noise of a serial communication line and the switching waveform of the PE converter. The conducted noise triggers a communication error. An oscillation waveform simultaneously occurs with a switching action of the converter. This indicates that time-domain analysis is necessary to obtain the EM disturbance mechanism. Specifically, both the noise amplitude and phase relation between the PE converter and communication signal are important whether a communication error occurs or not.

1.3 Research Objectives

This research aimed to develop time-dependent EMC solutions for the EM disturbance on a serial communication system caused by a PE converter. Two main steps achieve this objective:

- **Step1**: Time-domain analysis of the EM disturbance on a controller area network (CAN) communication system caused by a buck converter
- **Step2**: Development of EMC solutions to suppress the disturbance, focusing on the disturbance mechanism in the time domain

Numerous PE converters and communication systems are in practical use. Thus, the narrowing of a target system was necessary for the EMI study. This study focused on a typical non-isolated buck converter as a noise source and a CAN communication system as a noise victim. The buck converter has an embedded MOSFET and diode for switching operations. This uncomplicated configuration is suitable for a fundamental EMI analysis. Furthermore, findings from the analysis can be extended to other PE converters such as inverters and multilevel converters. Regarding the EMI noise of buck converters, time-domain analysis and the development of simulation models revealed the mechanism of the noise generation. In particular, this research focused on the two impedance factors that impact the noise behavior: stray impedance of a capacitor and OFF-state MOSFET impedance.

The CAN is one of the major serial communication systems and is used to build up a LAN. Automobiles prevalently use the CAN system for mission-critical applications such as traction control. Reference [9] estimated that the number of CAN nodes sold per year was approximately 400 million as of 2005. The CAN has a typical bus topology and differential signaling method that has a strong immunity to common-mode (CM) noise. Nevertheless, the CAN still requires extensive efforts for EMI reduction, as observed in various EMI products on the market such as CM chokes and shielded cables. As mentioned earlier, this thesis focuses on the CAN as a noise victim because the CAN employs a typical differential signaling technique. The EMC solutions developed for the CAN can be extended to other serial communication systems such as RS-485, which has a similar physical layer. In addition, the communication baud rate is close to the switching frequency of PE converters. For high-speed CAN (ISO 11898-2 [10]), the baud

rate is set to 125 kbps-1 Mbps. For PE converters, the switching frequency is often several tens of kHz. Owing to the frequency proximity, the phase relation between a PE converter operation and communication signal is sufficiently close to be measured in the time-domain analysis.

A time-domain analysis of the EM disturbance is necessary to develop EMC solutions. To perform the time-domain analysis, an experimental platform, called a noise injection system, enables us to measure the voltage/current waveform of a conducted noise with high repeatability. The bit error rate (BER) is a suitable index to quantify the EM disturbance on a CAN communication compared with frame loss rate (FLR) under an error process of an active protocol. Thus, aiming to observe the effects of the buck converter and other factors on the disturbance, the BER was investigated under several operating conditions of the buck converter. Moreover, the results from the BER tests revealed the critical causes of errors.

For the EMC solutions, a time-series control of the active gate driver (AGD) is proposed. An AGD enables the dynamic control of MOSFET switching speed and amount of noise generation [11]–[13]. Owing to this feature, to suppress the EM disturbance on CAN, the proposed method controls the switching speed of the converter MOSFET by monitoring a CAN signal status. Static low-speed switching also results in a reduction of the disturbance. However, it has limitations in terms of conversion efficiency because the switching loss increases. To solve this problem, the proposed method suppresses the increase in the power loss.

Generally, conventional EMI reduction methods such as filter circuits attempt to minimize the noise amplitude to ensure it does not interfere with other signals and exceed the noise limits specified by EMC standards. In contrast, as clarified through the time-domain analysis, the occurrence of a CAN error also depends on the phase relation with the converter operation. Thus, focusing on the timing problem, two methods are proposed: the timing-shift control of the buck converter and digital denoising on the CAN system. Both methods enable the communication error to be suppressed regardless of the noise amplitude, and they do not require additional bulky hardware components to implement.

Through the above work, this thesis aims to present the importance of a time-domain study on EM disturbance and propose time-dependent EMC solutions.

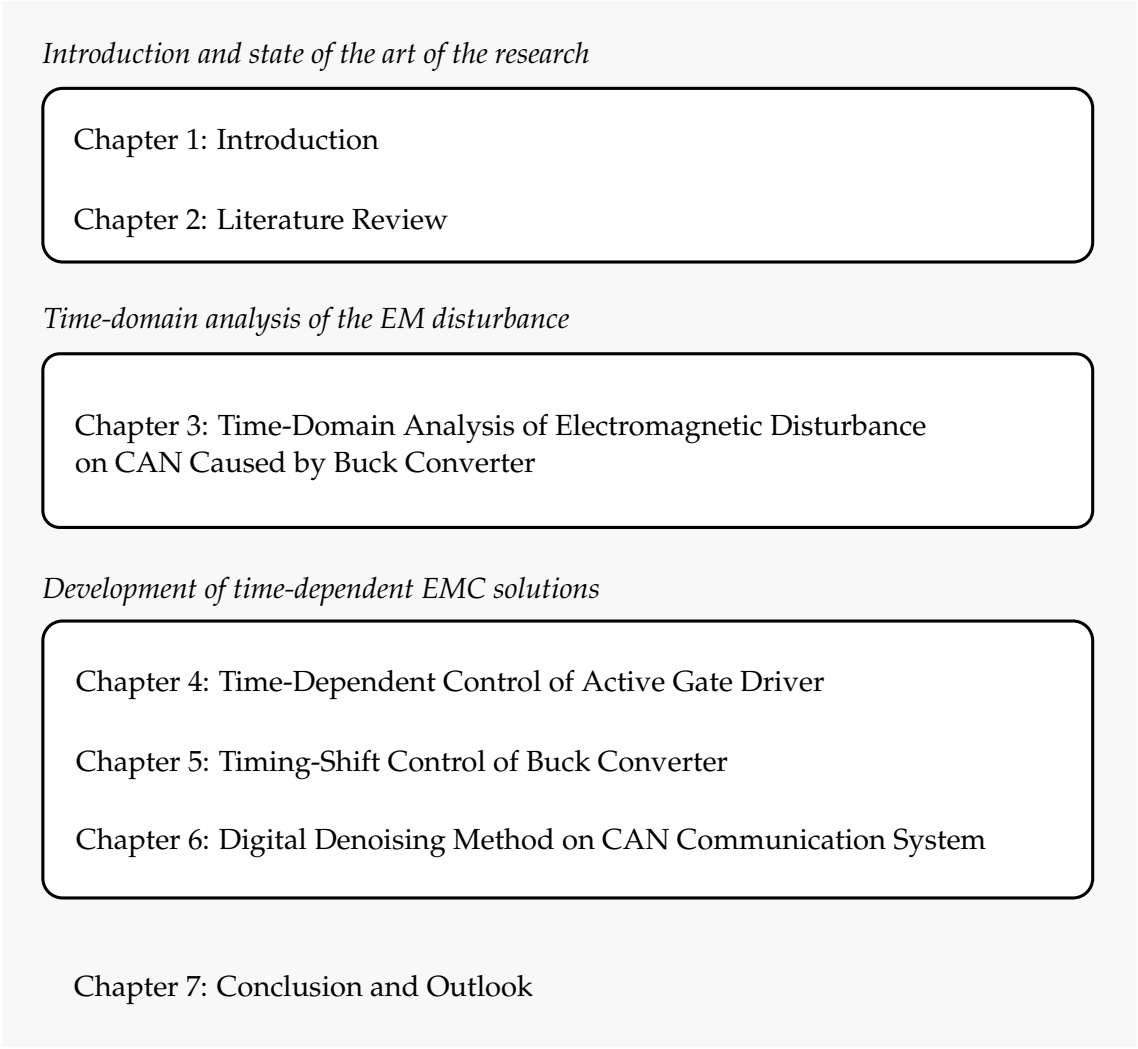

FIGURE 1.7: Dissertation outline

1.4 Dissertation Outline

Chapter 1 presents the background and motivations of the research. After reviewing the background of EMC between SMPSs and serial communication systems, this chapter provides case studies on incidents and accidents caused by EM disturbances on communication systems. Based on the studies, a statement of the problem is provided, followed by research objectives.

Chapter 2 reviews literature that is related to the EMC of SMPSs and CAN systems. The review on solving EM disturbance on CAN communication reveals that the time-domain phenomenon is a significant factor in understanding the physics underlying the disturbance and developing effective solutions. First, the EMI reduction techniques for PE converters are reviewed, with a focus on the

conducted noise. Subsequently, an overview of the specification of the standard CAN protocol, recent EMI research, EMC standards, and other communication protocols is provided. For EM disturbance, the number of time-domain studies addressing a PE converter and a serial communication system have been increasing. Most studies use time-domain waveforms to describe how a communication error occurs. Accordingly, the time-domain phenomenon is a key factor in developing EMC solutions, whereas the conventional approaches tend to focus on the noise amplitude in the frequency domain.

Chapter 3 summarizes the time-domain analysis of the disturbance caused by a buck converter on CAN communication. A noise injection system is developed as an experimental platform. The system consists of a buck converter and a CAN bus, and it can be used to perform experimental studies with high repeatability. In addition to experimental studies, simulation modeling methodologies are discussed. In particular, two types of parasitic impedance remain undeveloped regarding simulation modeling: the parasitic impedance of an electrolytic capacitor and OFF-state MOSFET impedance. Accordingly, experimental and simulation studies were performed to develop the simulation models. Subsequently, the simulation and experimental waveforms of the noise injection system were compared to verify the modeling approach and unveil the mechanism of EM disturbance, followed by an analysis of the CAN failure. Furthermore, an evaluation of the CAN error rate quantified the EM disturbance on a CAN communication. As indexes of the error rate, the BER and FLR were tested. The BER reflects the EM disturbance, whereas the FLR depends on the CAN protocol behavior. Through these studies, the mechanism of EM disturbance was unveiled to develop the EMC solutions.

Chapter 4 describes the time series control of an AGD to balance EM disturbance mitigation and converter performance. The AGD is one of the key technologies in controlling the switching speed of power semiconductor devices. By suppressing the switching speed of the device, an EMI reduction can be achieved. However, this causes an increase in the switching power loss and lowers the conversion efficiency. Thus, balancing the EMI reduction with the converter performance is a technical challenge. The time series control of the AGD realizes an effective EMI reduction focusing on the CAN data transmission behavior. For low bus traffic applications, the control method balances the EMI reduction and conversion efficiency, which was studied experimentally.

Chapter 5 presents the timing-shift control of the buck converter that realizes the EMI reduction through converter control. Unlike conventional EMI reduction methods, the control scheme aims to prevent communication errors even if the buck converter induces noise in the communication line. Despite the control suppressing the EM disturbance, shifting a switching timing potentially undermines the converter control stability. To solve this problem, a duty compensation method improves the stability.

Chapter 6, in contrast to the timing-shift control on the converter side, proposes the digital denoising technique that enables a CAN processor to remove error signals digitally. The denoising method can be applied to the communication system independently of the converter. To implement the denoising method to the noise injection system, a field-programmable gate array (FPGA) is integrated with the CAN controller. The denoising process occurs in the FPGA and the CAN controller receives the processed signals. Owing to the CAN sampling rule, the communication protocol does not require modification. Finally, experimental results validate the denoising method.

Chapter 7 provides the conclusions and future outlook of this research.

Chapter 2

Literature Review

This chapter reviews literature related to the EMC of SMPS and CAN systems. As mentioned earlier, PE converters have been sources of noise in various applications. Hence, many research efforts have been performed for the EMI analysis and reduction, focusing on each PE converter circuit. In contrast, the CAN has mission-critical functions as one of the robust communication systems. Various solutions in terms of hardware and software have been implemented to ensure highly reliable communication. Furthermore, some EMC standards specify the test procedure to evaluate the noise immunity performance of a CAN.

For the EM disturbance, the number of time-domain studies addressing the PE converter and serial communication systems has been increasing. Most studies use time-domain waveforms to describe how a communication error occurs. Therefore, the time-domain phenomenon is a key factor in developing EMC solutions, whereas the conventional approaches tend to focus on the noise amplitude in the frequency domain.

2.1 EMI Noise of Power Electronics Converters

2.1.1 Basics on EMI of Power Electronics

With the evolution of PE converters, there is an increasing concern over EMI noise. In particular, power semiconductors have been developed to achieve higher switching speeds, which results in lower power losses and the miniaturization of passive components in the circuit [14]–[18]. Over the past few decades, Si power devices such as IGBTs and MOSFETs have been the main components in the PE field. Additionally, the performance of devices has been pushed to the limit of Si [4]. To break through this limit, WBG devices have been gaining interest. WBG

devices typically use SiC and GaN as the semiconductor materials. Compared with Si, SiC and GaN exhibit higher saturation drift velocities and higher critical electric fields. These characteristics enable the performance to exceed the limit of Si devices. Accordingly, many research efforts have been performed to introduce WBG devices in practical PE converters [3], [19], [20].

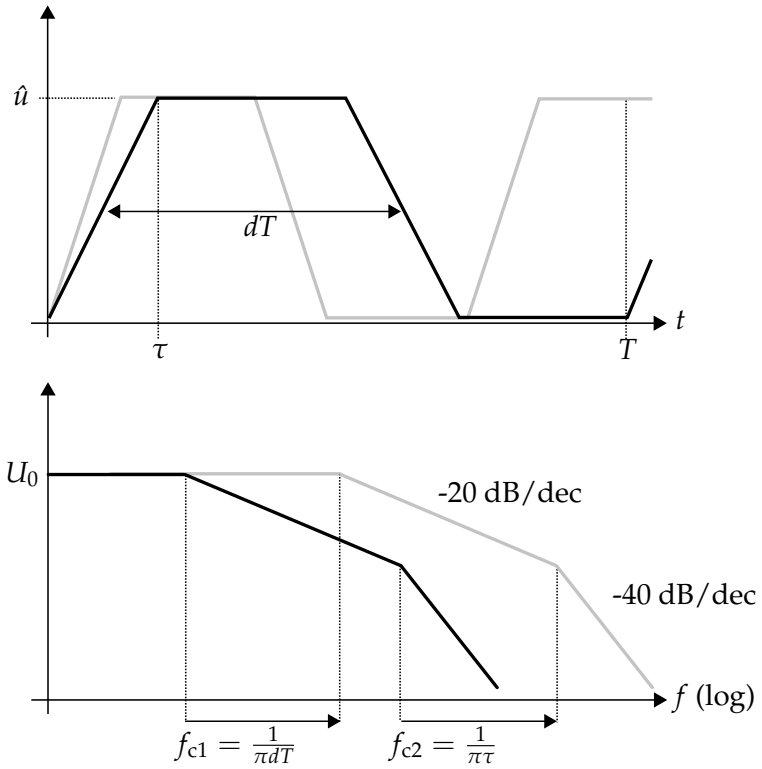

FIGURE 2.1: Spectrum of a trapezoidal waveform

Theoretically, the EMI noise of PE converters increases with the switching speed and frequency. Fig. 2.1 shows a spectrum of a trapezoidal waveform [1]. Assuming a pulse waveform in a PE converter to be trapezoidal, the pulse width (dT) provides the first cutoff frequency (f_{c1}), and the rise/fall time (τ) provides the second cutoff frequency (f_{c2}). Therefore, the two cutoff frequencies shift to higher values as the switching frequency and speed increase. Reference [17] reported an increase in the conducted EMI noise owing to a higher frequency and faster switching speed of power semiconductor devices.

TABLE 2.1: Approaches to reduce conducted EMI noise

Location	Classification	Reduction method	Examples
At the propagation path	External Filter	Passive filter	- DM/CM noise filter, Y-capacitor, etc.
		Active filter	- Active CM noise canceler
	Internal filter	Circuit layout	- Internal noise current circulation
		Circuit topology	- Symmetric topology, interleaving, etc.
At the noise source	Circuit design	PCB design	- Coupling reduction, efficient routing
		Component selection	- Selecting lower stray inductance component
	Control scheme	Low frequency switching	- Decreasing PWM carrier frequency
		PWM techniques	- Random, linear, non-linear carrier modulation
	Switching transition	Snubbers	- RC, RCD, active clamp snubber
		Active gate driving	- Current source, digital active gate driver
		Soft switching	- Zero volt/current switching

Therefore, the demand for the reduction of conducted EMI noise is increasing. Table 2.1 shows approaches to reduce conducted EMI noise in practical use [5], [21]. Indeed, passive and active filters have a remarkable role in noise reduction. Passive filters use inductors and capacitors to create an impedance mismatch in the noise path [22], [23]. Active filters sense the voltage or current at the input ports and produce voltage or current of the opposite phase to cancel the original noise [23]–[26]. Generally, active filters are more space-saving, but they have difficulty in reducing noise in high-frequency regions. Since both filters have advantages and disadvantages, [27] proposed a hybrid type filter that is compact and requires noise attenuation. These filters are applicable to the input or output sides of the PE converters, although proper filter design is required for many cases. In the design phase of a PE converter, the layout, topology, and parts selection also impact the noise behavior [28]. EMI simulation is often performed to optimize these design factors. For the switching control scheme, the switching frequency directly affects the noise spectrum of a PE converter. Hence, lowering or modulating the switching frequency facilitates a spectrum reduction [29]–[32]. For specific converters, such as three-phase inverters, the pulse width modulation (PWM) control scheme can be modified to suppress the EMI noise [33], [34]. As a root cause of the conducted noise, the switching waveform determines the noise signature in the frequency domain. Snubbers, gate drivers, and soft switching can be used to tune the dv/dt operation with some extent of flexibility [35]–[38]. These solutions often have a trade-off between a switching power loss and a lower EMI noise.

2.1.2 EMC Standards for PE Converters

EMC standards define terminology, rules, and test methods to ensure EMC. Technically, they specify limits and minimum test levels for electric and electromagnetic emissions and the immunity of electronic products. For PE converters and communication systems, manifold EMC standards have been published by the International Electrotechnical Commission (IEC) and domestic organizations. Table 2.2 provides a list of PE-related technical committees of the IEC. Each committee publishes and updates technical standards.

TABLE 2.2: Power-electronics-related committees of the IEC

Committee number	Content
TC1	Terminology
TC9	Electrical equipment and systems for railways
TC14	Power transformers
TC22	Power electronic systems and equipment
TC47	Semiconductor devices
TC47E	Discrete semiconductor devices
TC77	Electromagnetic compatibility
TC77A	Low frequency phenomena
TC77B	High frequency phenomena
TC82	Solar photovoltaic energy systems
TC88	Wind turbines
TC105	Fuel cell technologies

2.2 Overview of the Controller Area Network (CAN)

2.2.1 Specification of the CAN Protocol

> —— *The Controller Area Network (CAN) is a serial communications protocol which efficiently supports distributed realtime control with a very high level of security. Its domain of application ranges from high speed networks to low cost multiplex wiring. In automotive electronics, engine control units, sensors, anti-skid-systems, etc. are connected using CAN with bit rates up to 1 Mbit/s. At the same time it is cost effective to build into vehicle body electronics, e.g. lamp clusters, electric windows etc. to replace the wiring harness otherwise required.* (CAN Specification, Bosch GmbH, 1991)

The CAN protocol was originally developed by Robert Bosch in the 1980s [39], [40]. As of 2005, [9] estimated that the number of CAN nodes sold per year was approximately 400 million for all the application fields. Compared with other major serial communication protocols, CAN has advantages in robustness, error detection, and low cost. Furthermore, a simplified configuration and low cost have resulted in the adoption of CAN throughout automotive and automation industries. Specifically, there are several variants of CAN protocol: CAN 2.0A,

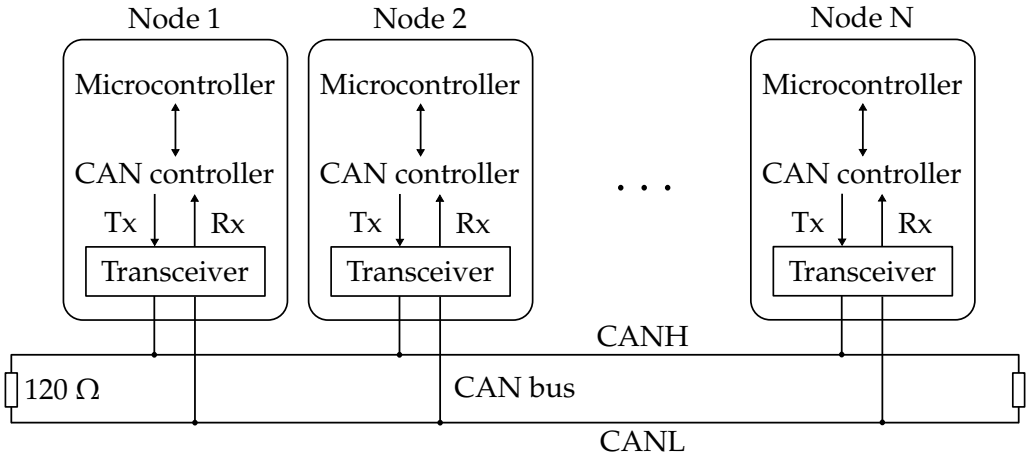

FIGURE 2.2: Configuration of the CAN system

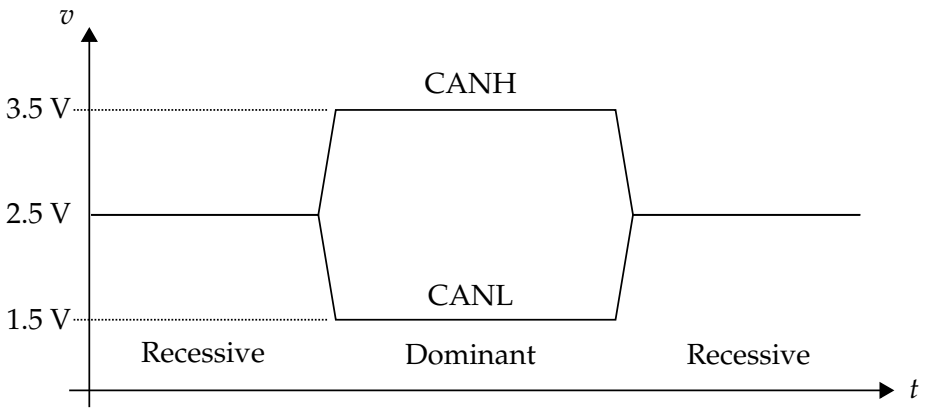

FIGURE 2.3: CAN bus state voltage

CAN 2.0B, and CAN FD. This thesis focuses on CAN 2.0B specified in CAN 2.0 part B that uses 29-bit identifiers.

Fig. 2.2 shows the configuration of a CAN system with multiple nodes. The CAN employs a differential signaling technique to transmit signals. Accordingly, the bus has CANH and CANL lines with termination resistors of 120 Ω. Each CAN node consists of a transceiver, CAN controller, and microcontroller. The transceiver is an interface to convert a differential signal of the CAN bus to a logic signal. Fig. 2.3 shows the differential signal level of the CAN bus. The transceiver drives recessive or dominant signals to the bus, and it also receives the signals from the bus. The CAN controller processes data to and from the microcontroller based on the communication protocol. Thus, synchronization with other nodes and signal sampling occur in the CAN controller. The microcontroller corresponds to the application layer of the system in which data transmission is required.

As a practical overview, serial communication systems are primarily divided into wired and wireless communication, and a wide variety of communication protocols are available. For instance, Fig. 2.4 shows the list of major communication protocols for automobile applications. Each application system employs the protocols depending on the required data rate and performance. For mission-critical applications of the power train and safety ADAS, the applications often employ the CAN communication protocol.

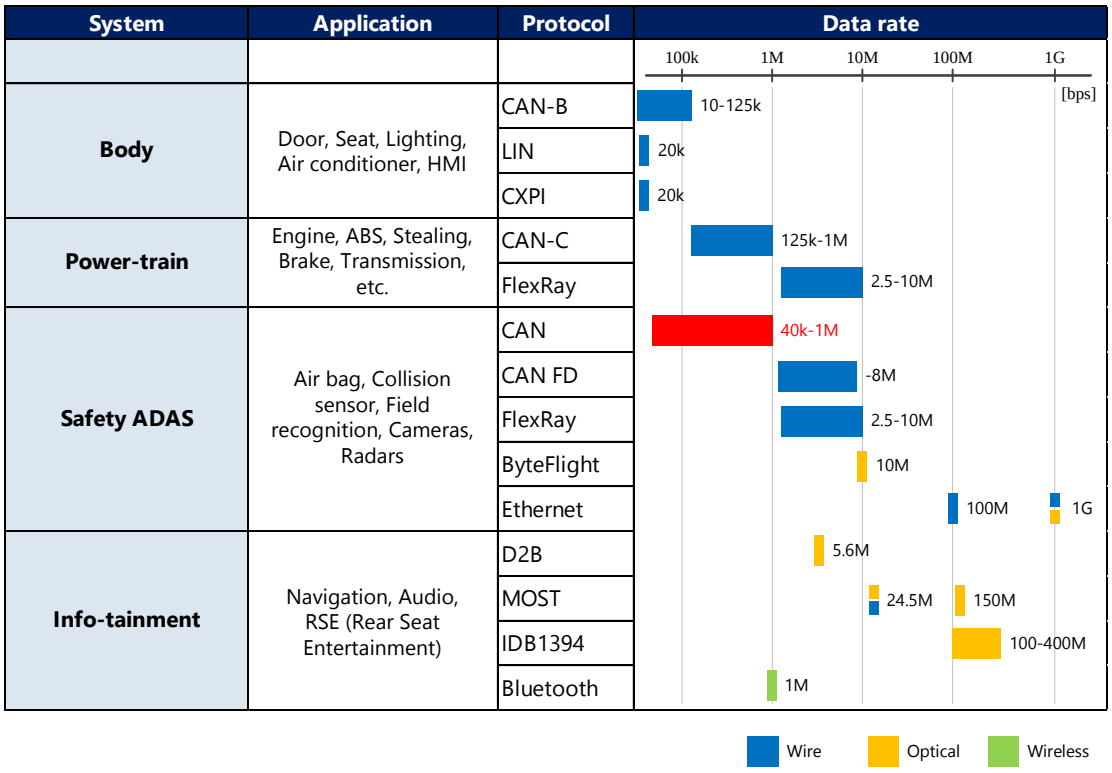

FIGURE 2.4: Communication protocols for automobile applications

2.2.2 EMI Solutions for CAN Communication Systems

While the CAN represents a robust communication system, and the EMI problem has been a significant topic, only a few studies have addressed EMI on CAN communication in practical systems [41]. Through experiments, [42], [43] reported that a DC–DC converter can cause interference on a CAN communication. Reference [44] investigated the effects of EMI on CAN performance. According to the study, the use of unshielded cables makes a bus more susceptible to noise and undermines the communication performance.

Fig. 2.5 depicts the block diagram of a transceiver (MCP2551, Microchip Technology, Inc.) as an example. Reference [45] focused on a transceiver as a key component that determines EMI behavior in a CAN system. Theoretically, a CAN bus has a symmetric impedance for the CANH and CANL lines, which results in strong CM immunity. However, an impedance analysis indicated that the CAN transceiver has an imbalanced impedance on the CANH and CANL ports. The imbalanced impedance causes a skew and a mode conversion, which undermines the communication performance.

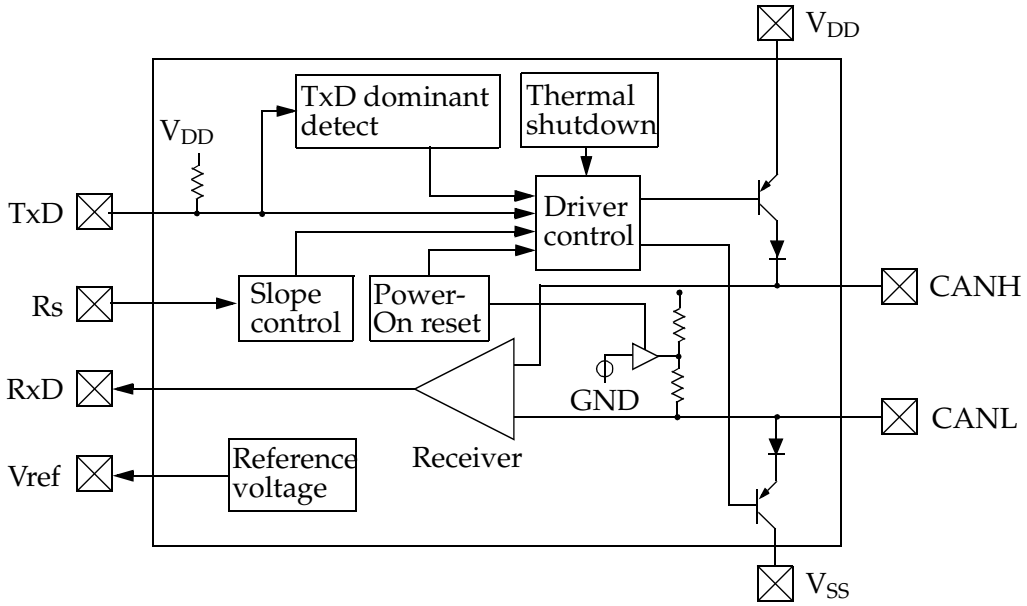

FIGURE 2.5: Block diagram of an MCP2551 CAN transceiver [46]

For applications in which CAN systems operate, CM chokes and filters are still a major solution [47]. Certainly, such additional components result in a cost increase. To reduce costs, some semiconductor companies have developed low-CM noise transceiver integrated circuits (ICs). According to [48], CM chokes can be omitted by using transceivers that have low output CM noise. Similarly, in 2014, NXP Semiconductors announced that the new transceivers were officially certified for automotive use by Volkswagen [49]. The new transceivers did not require additional CM chokes in the communication line. From these trends, while many EMI products are available on the market, more cost-effective solutions are still required.

TABLE 2.3: Standardized EMC evaluation methods for transceivers

IEC62228 series	Subject	Status
Part 1	Generation and definition	Published
Part 2	LIN transceivers	Published
Part 3	CAN transceivers	Published
Part 4	FlexRay transceivers	In progress
Part 5	Ethernet transceivers	Published
Part 6	CXPI transceivers	Started
Part 7	PSI5 transceivers	In progress
Part 8	SENT transceivers	In progress

2.3 EMC Standards for CAN

In contrast to the EMC standards of PE converters, more efforts on immunity evaluation methods have been implemented on the standardization of communication systems. Table 2.3 shows standardized EMC evaluation methods for communication transceivers [50]. For instance, IEC62228-3 for CAN transceivers is described as fol lows [51]:

> —— *This part of IEC 62228 specifies test and measurement methods for EMC evaluation of CAN transceiver ICs under network condition. It defines test configurations, test conditions, test signals, failure criteria, test procedures, test setups and test boards. It is applicable for CAN standard transceivers, CAN transceivers with partial networking functionality and CAN transceivers with flexible data rate capability and covers*
>
> - *the emission of RF disturbances,*
> - *the immunity against RF disturbances,*
> - *the immunity against impulses, and*
> - *the immunity against electrostatic discharges (ESD).*

Similarly, other parts of the IEC62228 series cover these topics. Under increasing demand to ensure the functional safety and reliability of serial communication systems, IEC62228 has been developed for automotive applications [52].

Regarding the evaluation of noise immunity, several international standards that specify the test procedure are available. ISO 7636-3 defines test methods to evaluate the noise immunity of devices under test (DUTs) to transient pulses [53]. Figs. 2.6 and 2.7 show the measurement setup of the direct capacitive coupling

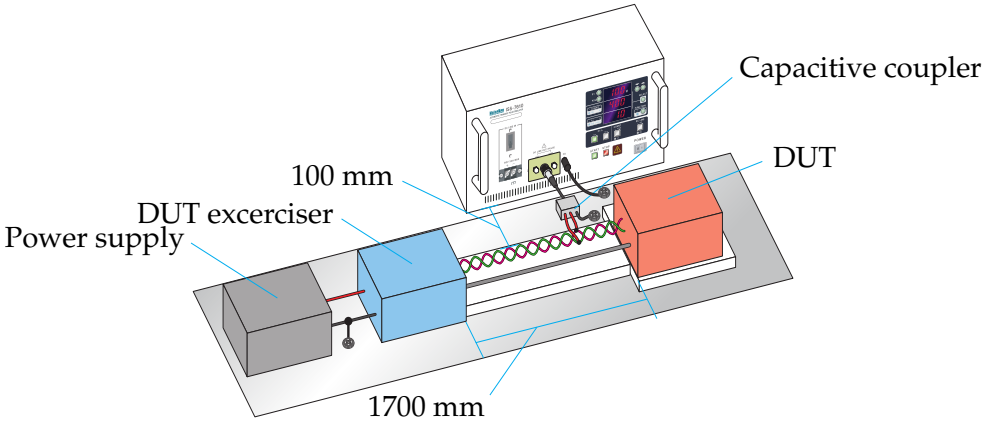

FIGURE 2.6: Direct capacitor coupling (DCC) method for Fast Pulse and Slow Pulse [54]

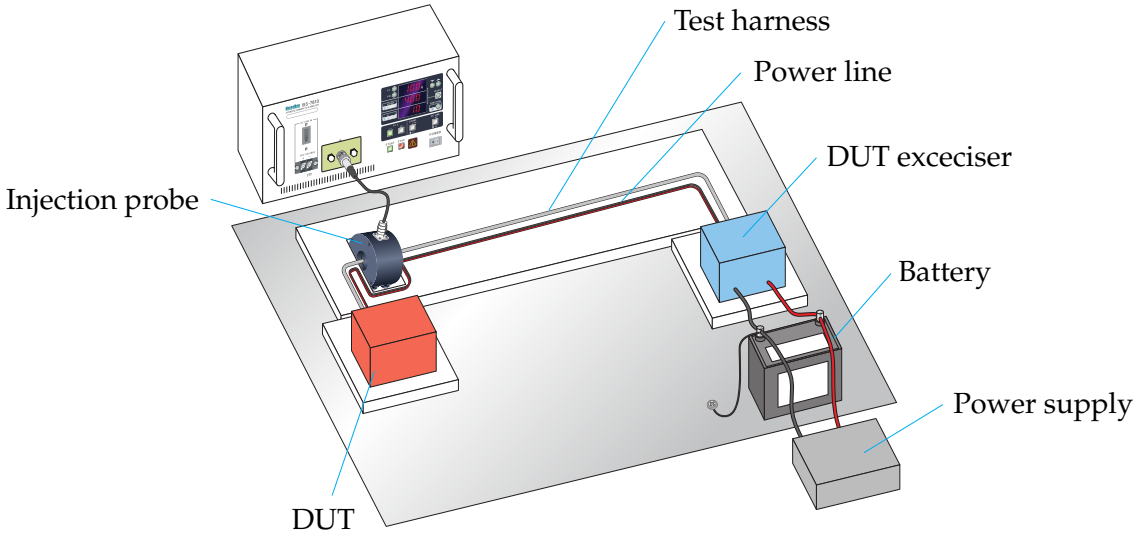

FIGURE 2.7: Inductive coupling clamp (ICC) method [54]

and inductive coupling clamp methods. Via the coupling, the test pulses simulate fast and slow transient disturbances.

As an example, Ford Motor Company published the EMC standard EMC-CS-2009. The standard defines EMC requirements, test methods, and test procedures for electrical/electronic components and subsystems for automotive use. In particular, RI 130 and 150 define requirements regarding the coupled immunity. Fig. 2.8 depicts the test fixture required to couple noise sources and DUT circuit wire/wire pairs. These immunity tests are necessary to ensure a robust operation of CAN communication. However, the measurement setups are not suitable for developing EMC solutions at the application level because the noise

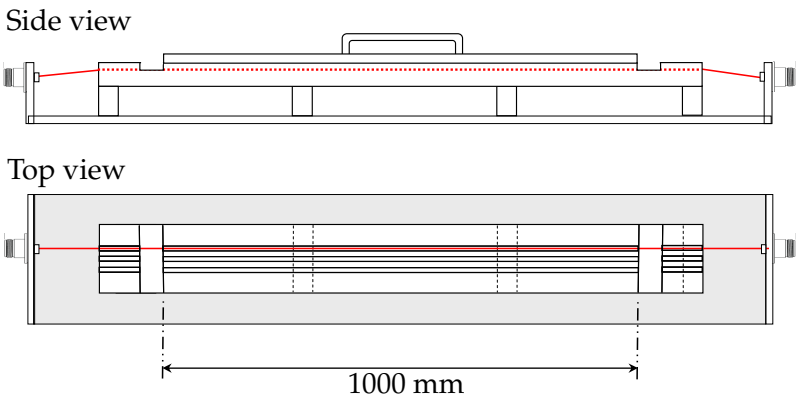

FIGURE 2.8: RI 130/150 test fixture [55]

source and coupling mechanism would differ.

2.4 EM Disturbance on Communication Systems

Fundamental studies on the EM disturbance have been presented and are increasing each year [44], [56]–[62]. Reference [29] investigated the effect of EMI on a communication channel. The BER measurement clarified that the spread-spectrum modulation scheme of a DC–DC converter significantly affects the er ror rate. This also suggests that spread-spectrum modulation is not always effective for suppressing disturbances although it is capable of spectrum reduction. Reference [56] conducted an experimental study of EMI on Ethernet communication. By injecting noise by driving a three-phase inverter nearby the Ethernet cable, the communication performance deteriorated and the data rate significantly decreased as the noise pulse amplitude increased.

Although many attempts have been performed to investigate the EM disturbance on communication systems, only a few of them have focused on the solution based on the disturbance mechanism. In other words, a mainstream solution to suppress the disturbance is applying EMI reduction techniques without testing the effects on the victim.

Reference [59] proposed an electrical falsification method of CAN data. Potentially, an adversary can tamper the CAN data by injecting pulses. To investigate the effects of the injected pulses on CAN data, time-domain analysis is necessary to unveil the mechanism. Hence, the authors measured the time-dependent waveform of the communication signals to detect points at which an error occurs.

Reference [63] addressed the EM disturbance caused by multiple DC–DC converters. If the DC–DC converters operate asynchronously, the noise waveform induced on the communication line changes with time. The authors considered a superimposed noise waveform in the time-domain and they observed the critical conditions that result in an error. Time-domain analysis is a key to understanding the mechanism of the EM disturbance. Considering a PE converter and serial communication, they are generally operated asynchronously and phase relation varies depending on their operation frequency and scheme. Hence, an error occasion can be detected only in the time domain.

2.5 Summary

This chapter has covered a literature review on EMI noise of PE converters, an overview of CAN, EMC standards for CAN, and EM disturbance on communication systems. For the EMI noise of PE, with the advent of WBG power semiconductors, the conducted EMI noise from PE converters has been increasing and will increase in the future. In this context, various solutions are available on the market and subject to research. However, most of them aim to attenuate the conducted noise, while the target of this research was the avoidance of time-based noise.

Indeed, the CAN is a prevailing serial communication protocol in various applications. Correspondingly, EMI problems are of significant concern to realize robust communication. Several standards that define the noise immunity test procedure have been published. The test platforms almost always use a function generator as a noise source and inject conducted noise into the CAN bus. The test methods are suitable for evaluating the noise tolerance level on the same ring with reference levels. However, for EMC solutions, the platforms are not appropriate because the noise waveform and pattern would differ from the practical ones.

In these contexts, studies on the EM disturbance have been gaining interest gradually. The studies commonly apply time-domain analysis to the systems in which a PE converter causes an EM disturbance on the serial communication system. Considering the mechanisms of the EM disturbance, in contrast to the amplitude-domain, the time-domain may provide a path for new solutions.

Chapter 3

Time-Domain Analysis of Electromagnetic Disturbance on CAN

3.1 Introduction

This chapter presents a time-domain analysis of EM disturbance on CAN communication caused by a buck converter. To understand the mechanism of a conducted EMI noise emitted by a buck converter, we developed an experimental platform called the noise injection system. The noise injection system consists of a buck converter as the noise source and CAN communication system as the noise victim. In addition to experimental analysis, a simulation model of the noise injection system was developed. Regarding the modeling methodology, two simulation models affecting the EMI noise are discussed:

- the stray impedance of electrolytic capacitor to be a noise propagation path in a power electronic system
- the output impedance of a MOSFET to impact a noise waveform of the CAN communication line

Compared with the simulation results, the experimental waveform of the noise injection system revealed the noise propagation mechanism and how a communication error occurs. Furthermore, measuring the CAN error rate enabled us to quantify the EM disturbance on the communication. The measurement results indicated that the error rate strongly depends on the noise waveform induced by the buck converter. In other words, the converter operation condition and other experimental setups affect the error rate.

3.2 Noise Injection System as an Experimental Platform

Figs. 3.2−3.3 and Table 3.1 show the specification of a noise injection system consisting of a buck converter and CAN bus. The noise injection system enabled us to intentionally cause CM interference on the communication system and perform EMI analysis. In this thesis, the term "noise injection system" refers to an integrated system for intentional noise injection to a communication system and for verifying EMI reduction methods. When designing the platform, various aspects were considered to ensure high repeatability.

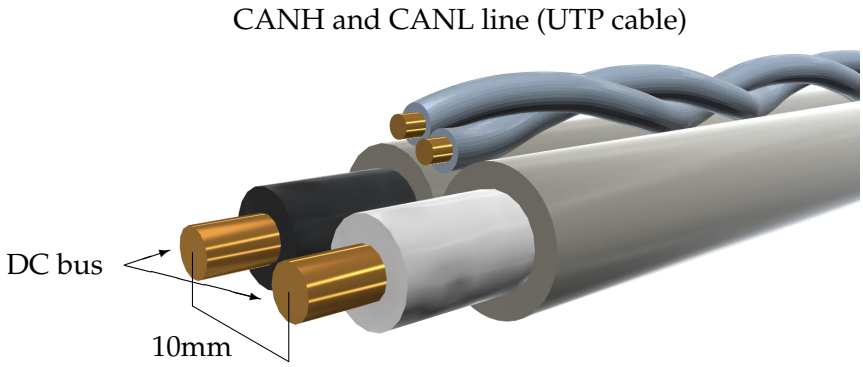

FIGURE 3.1: Configuration of the EM coupled cables

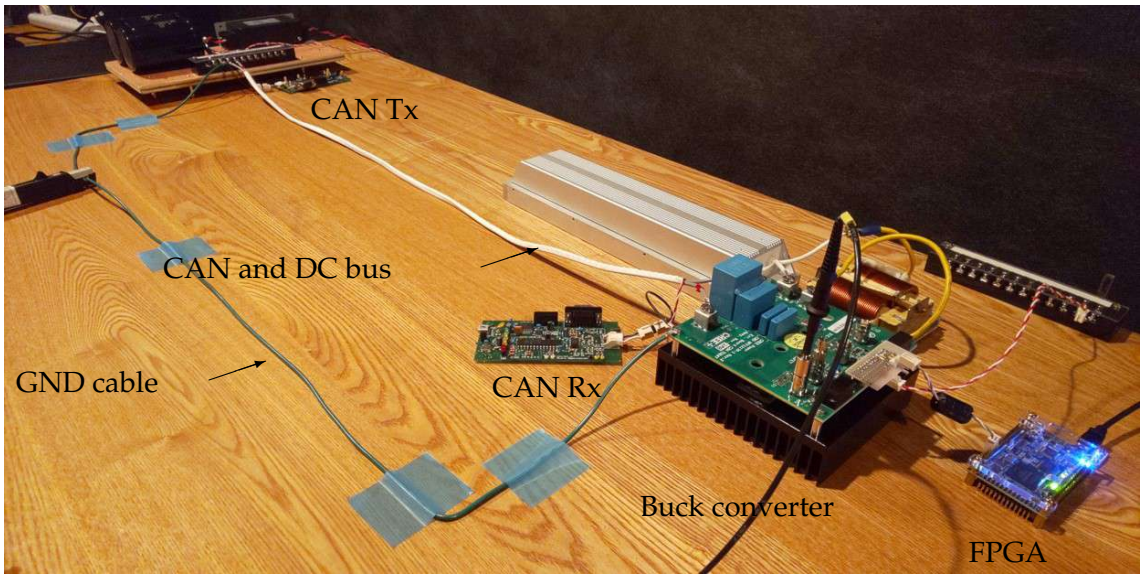

FIGURE 3.2: Experimental setup of the noise injection system

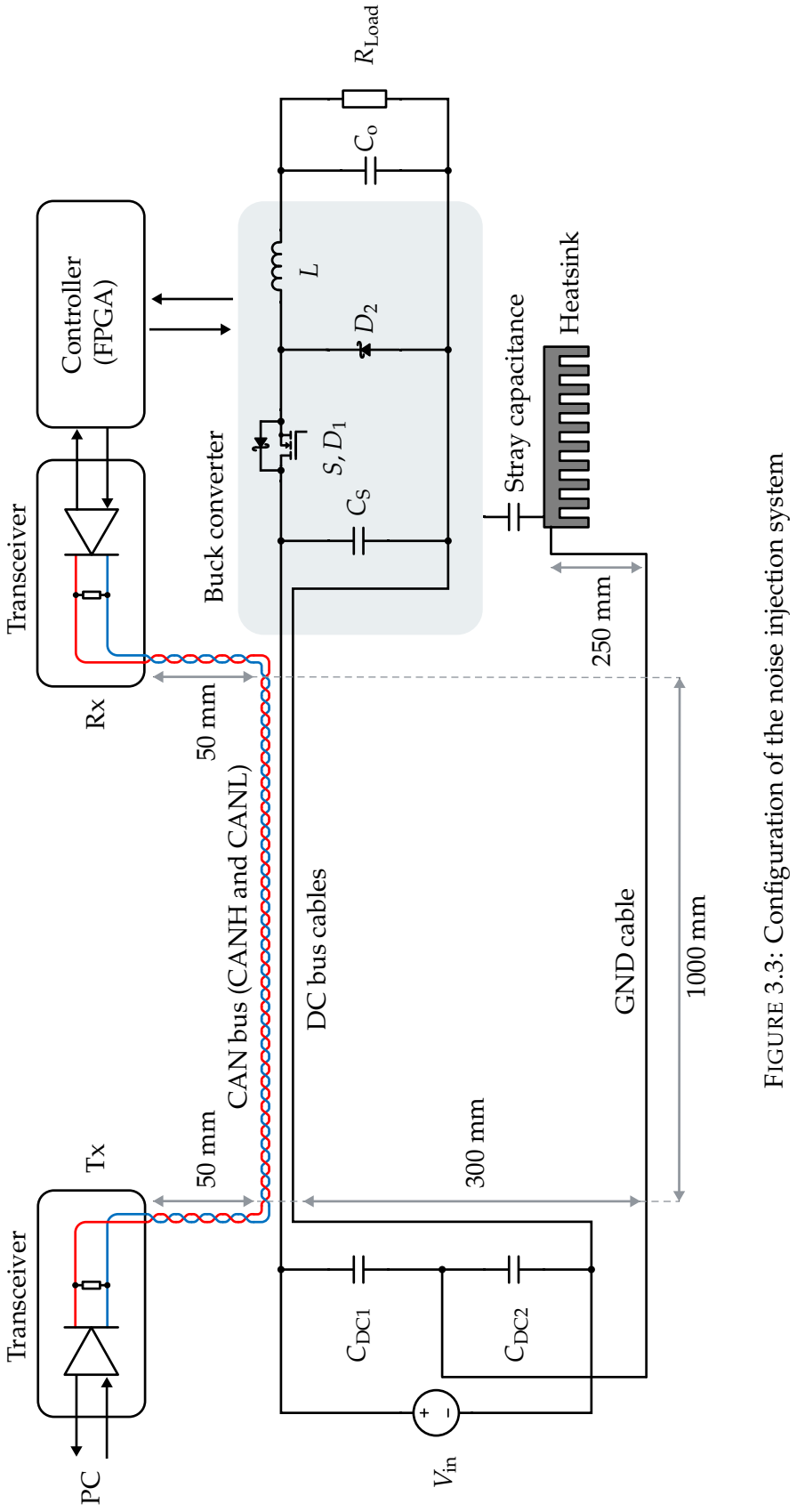

FIGURE 3.3: Configuration of the noise injection system

TABLE 3.1: Specification of the noise injection system

Symbol	Description
S	SiC-MOSFET, CREE, C3M0065090D
D_1, D_2	SiC Schottky diode, CREE, C3D20060D
C_{DC1}, C_{DC2}	1800 μF, 400 V (Electrolytic capacitor)
C_S	5.1 μF (Film capacitors)
L	288 μH (Iron core inductor)
R_{Load}	20 Ω (Metal clad resistor)
C_o	3200 μF, 1200 V (Electrolytic capacitor)

For the PE converter, the buck converter was used to generate a CM noise owing to a simple topology and versatility. In addition, the buck converter had an embedded SiC MOSFET that realized a high-speed switching operation. Regarding the CAN system, two nodes were required as a transmitter and a receiver, respectively. Thus, the CAN bus had only two nodes that did not implement EMI filters.

To integrate the buck converter and CAN system as an experimental platform, stable EM coupling between the two was necessary. Generally, uncountable forms of EM coupling between an SMPS and communication system exist in practical systems such as electric vehicles and industrial systems, and they often complicate the EMI mechanism. The noise injection system exhibited predominant inductive coupling between the DC bus and communication cables, inducing a CM noise in the communication line and resulting in an experimental verification of high repeatability. The coupled cables were bundled close together with a heat shrink tube and adjusted to a 1-m length (Fig. 3.1). This configuration made the noise injection more repeatable because the coupling factors among the cables were fixed stably.

The buck converter operated by switching a SiC MOSFET, which resulted in emitting conducted CM noise. The heat sink was connected to the neutral point of the DC link capacitors with a grounding cable. The converter operating conditions were as follows: DC bus voltage of 100 V, switching frequency of 30 kHz, and a constant switching duty ratio of 0.5.

The ohmic load was 20 Ω; hence, the average input current of the DC bus was 1.25 A. In addition, the CAN bus connected two transceivers with CANH and CANL lines, because the physical layer employed a differential signaling method. The two transceivers had a ground point at the DC link and converter

sides.

Although the CAN bus had an additional common ground wire, the absence of a ground connection between the transceivers simplified the EMI analysis because the ground cable could have electromagnetic coupling with the other cables. The high-speed CAN defined by ISO 11898 specifies the use of a shielded twisted pair (STP) or unshielded twisted pair (UTP) cable for the bus. Thus, the CAN system implemented UTP cables for the bus, which made the EMI analysis more straightforward than if STP cables were used. The CAN bus had termination resistors at both ends of cables because the CAN standard also requires a cable with a nominal impedance of 120 Ω.

3.3 Simulation Model of the Noise Injection System

A circuit simulation model of the noise injection system is shown in Fig. 3.4, which was used to investigate the CM interference mechanism. In this study, the simulation model employed 10 segments of a lumped-T model to simulate the 1-m coupled cable. The lumped-T model is suitable for connecting with low-impedance loads, such as the CAN termination resistors and DC coupling capacitors, to mask the effect of the shunt capacitance of the cable [64].

In addition to the extraction of the wire self-inductance and capacitive coupling parameters through the use of an impedance analyzer (Keysight Technologies, E4990A), the estimated mutual inductance based on the physical structure was uniformly divided by the number of segments, thereby providing the RLC network parameters. According to the measured noise waveform in the CAN bus, the maximum noise frequency was less than 50 MHz; hence, the target simulation frequency range was up to 50 MHz. According to the AC analysis of the simulation model, the 10-segment model was reasonably accurate for simulating the impedance characteristics. Mathematically, at least six segments were required to simulate the resonance/anti-resonance frequencies of the cables. Increasing the number of segments as much as possible can increase the simulation precision, but it also increases the simulation time.

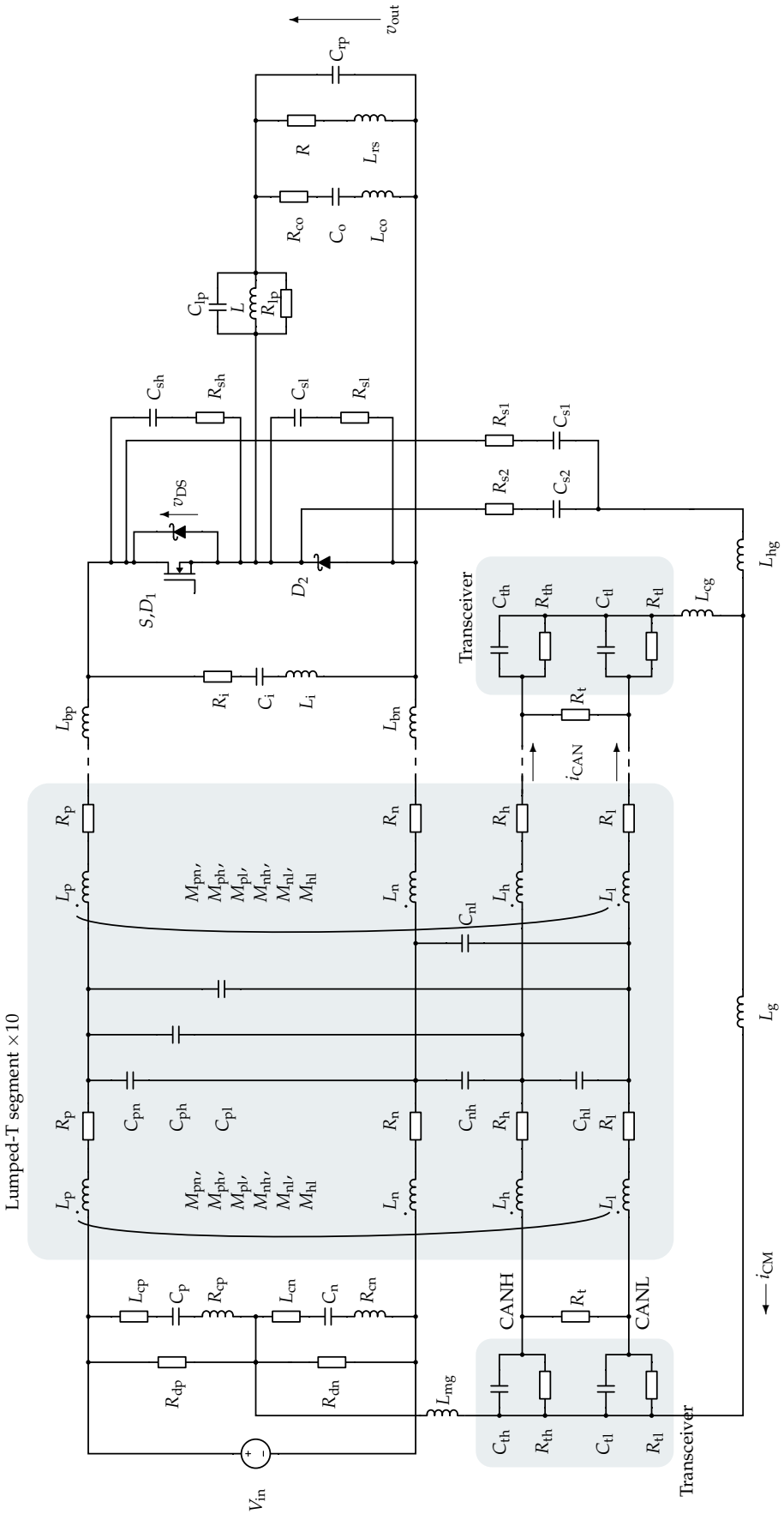

FIGURE 3.4: Simulation model of the noise injection system

TABLE 3.2. Parameters of the simulation model

Symbol	Value	Symbol	Value	Symbol	Value	Symbol	Value	Symbol	Value	Symbol	Value
V_{in}	100 V	R_p	7.65 mΩ	M_{pl}	16 nH	L_g	4.5 μH	R_{sh}	10 Ω	C_{s1}	41 pF
R_{dp}	100 kΩ	R_n	7.67 mΩ	M_{nh}	16 nH	L_{hg}	100 nH	R_{sl}	10 Ω	C_{s2}	21 pF
R_{dn}	100 kΩ	R_h	7.2 mΩ	M_{nl}	16 nH	L_{cg}	100 nH	L	290 μH	R_t	120 Ω
L_{mg}	100 nH	R_l	7 mΩ	M_{hl}	26.8 nH	L_{bp}	20 nH	C_{lp}	8.29 pF	C_{th}	28 pF
L_{cp}	20.9 nH	L_p	50.3 nH	C_{pn}	5.3 pF	L_{bn}	20 nH	R_{lp}	11.9 kΩ	C_{tl}	33 pF
L_{cn}	20.9 nH	L_n	50.4 nH	C_{ph}	3.2 pF	L_i	5 nH	L_{rs}	12.5 nH	R_{th}	280 kΩ
C_p	1.83 mF	L_h	63.5 nH	C_{pl}	3.96 pF	C_i	5.12 μF	R	22.6 Ω	R_{tl}	180 kΩ
C_n	1.83 mF	L_l	65 nH	C_{nh}	4 pF	R_i	100 mΩ	C_{rp}	16.3 pF	L_{co}	30.4 nH
R_{cp}	42.1 mΩ	M_{pn}	16 nH	C_{hl}	8.3 pF	C_{sh}	220 pF	R_{s1}	80 Ω	C_o	3.12 mF
R_{cn}	42.1 mΩ	M_{ph}	16 nH	C_{nl}	3.9 pF	C_{sl}	220 pF	R_{s2}	80 Ω	R_{co}	53 mΩ

Most of the other components of the noise injection system, except the CAN transceiver and some parasitic impedance, were determined using impedance extraction through the use of an impedance analyzer and simple hand calculation. The values of the stray capacitances C_{s1} and C_{s2} between the power devices and heat sink and electromagnetic couplings among the DC bus and communication cables were derived using a mathematical estimation based on the physical structure. The stray capacitance values of the power devices were estimated assuming parallel metal plates. For self-inductance and dumping resistors R_{s1} and R_{s2}, the inductance value was estimated based on the cable length; furthermore, the resistance value was derived from the dumping factor of a measured noise waveform.

For the CAN transceiver model, shown in Fig. 3.5, the intrinsic impedance of the transceiver IC impacted the noise propagation mechanism in the CAN bus [65], [66]. Therefore, precise modeling of the transceiver was necessary to simulate the noise accurately. A measuring circuit was used to obtain the impedance characteristics of the transceiver at power-on, and it consisted of DC-blocking capacitors (0.1-μF ceramic capacitors) and a voltage supply to keep the transceiver IC active. The DC-blocking capacitors, which passed only AC components for the measurement, were required because the CANH and CANL ports had a DC offset. According to the measured impedance curves, shown in Fig. 3.6, the ohmic characteristic appeared under several kHz, and capacitive behavior was observed in the higher frequency range. Additionally, the two impedance curves were not congruent, which resulted in noise mode conversion.

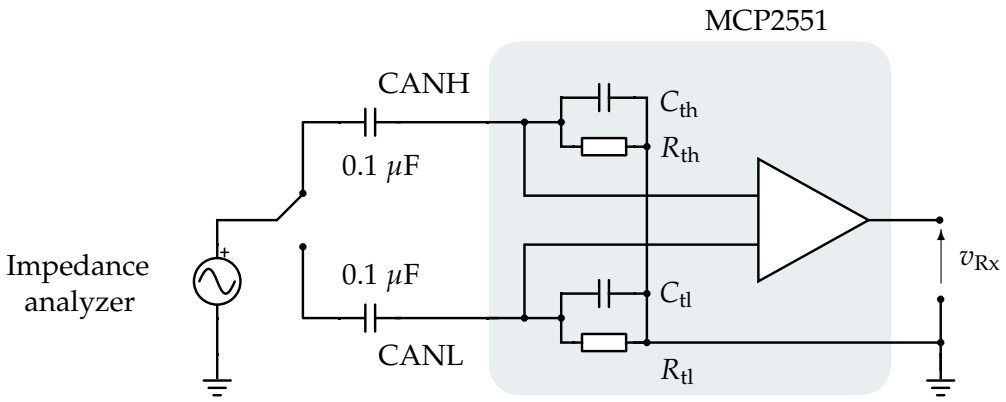

FIGURE 3.5: Circuit diagram for describing impedance measurement of the transceiver IC

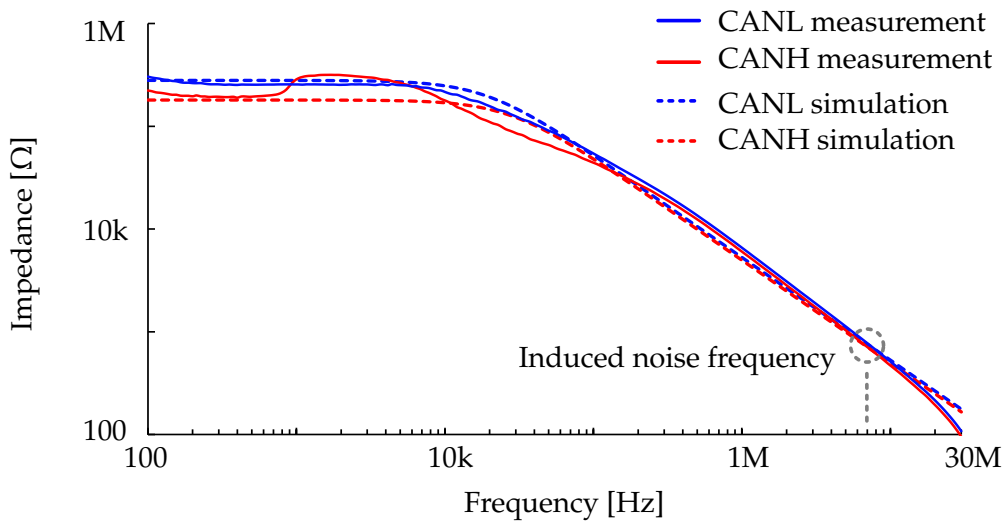

FIGURE 3.6: Measured and simulated impedance characteristics of the transceiver IC

Since the error pulse in the Rx output results in EMI failure on CAN communications, CM noise current in the power earth cable should be reduced to avoid the error pulse. Hence, it is important to specify the boundary where the error pulse appears using the CM noise current in the CAN bus. The CM noise susceptibility of the CAN transceiver was difficult to calculate based on the impedance curves of the CANH and CANL ports since the transceiver IC also had a response delay for an input signal. Therefore, it was better to obtain the threshold level based on experiments. In this study, only the recessive-to-dominant error was studied because the dominant-to-recessive error is relatively EMI resistant, which has been clarified through experimental studies. Fig. 3.7 shows the experimental setup for injecting a CM current into the CAN transceiver IC. The function generator was used to inject a sinusoidal current from 1 to 20 MHz by varying the current amplitude in each frequency. To obtain a threshold level, we measured the CM peak current in the CAN bus when a recessive-to-dominant error occurred in the Rx output voltage, and the minimum value of the CM noise current was measured as a peak current. Thereby, the negative CM current was converted to a positive DM noise since the CANH port impedance was smaller than the CANL port impedance in the transceiver IC.

Fig. 3.7 shows the configuration of the measurement circuit for a CAN transceiver. Fig. 3.8 shows that the measured threshold level depended on the frequency, and the tolerable noise level decreased with frequency. Furthermore, the measured

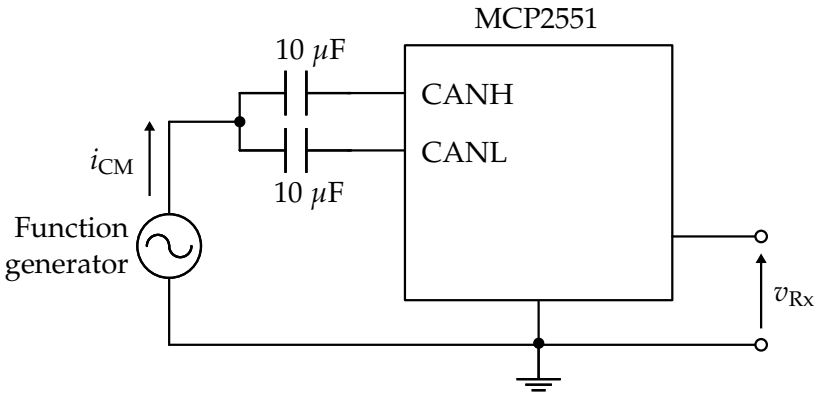

FIGURE 3.7: Configuration of the experimental system

threshold level was verified by plotting the CM peak current under the converter operation, as depicted by the red dots in Fig. 3.8. Considering the noise mechanism, the threshold level was also effective in revealing the correlation between the converter operating condition and CAN errors. Under a converter input voltage higher than 60 V, the CM peak current exceeded the threshold level, and CAN communication failure occurred. In contrast, when the CM peak current was lower than the threshold level, no CAN errors were detected. Hence, for EMI reduction on the CAN communication, a CM peak current should be suppressed lower than the threshold level. These observations indicated that the transceiver IC may cause a noise mode conversion owing to the unbalanced impedance.

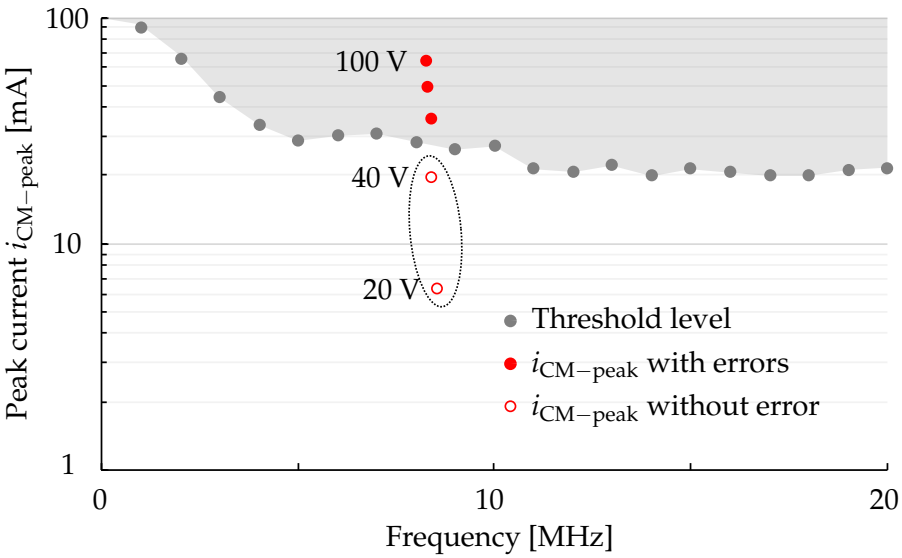

FIGURE 3.8: Measured threshold level of $i_{CM-peak}$

3.4 Modeling Methodologies: Parasitic Impedance of Capacitor

3.4.1 Introduction

Conducted noise commonly propagates through a parasitic and stray impedance that exists unintentionally [62], [67]. The unintentional impedance often results from the physical structure of the circuit and components. Often, the impedance can be suppressed by modifying the structure, such as decreasing the proximity and shielding, which results in noise reduction. For instance, [68] presented a method of canceling the parasitic capacitance of a three-phase CM inductor. In addition to passive components, power devices also have structural problems such as parasitic capacitance between a semiconductor die and package baseplate [69]. Understanding such parasitic impedances is important for simulation modeling and EMI reduction.

Electrolytic capacitors have a key role in PE converters, particularly to smooth a DC bus voltage [70]. However, owing to the size of the package, an electrolytic capacitor has a parasitic capacitance to the grounding frame and other components. For example, for electrolytic capacitors of railway applications, IEC 61881-2 specifies quality, test, and safety requirements and describes installation and operation information [71]. Based on the standard, metal packages of an electrolytic capacitor must be grounded to a chassis to fix the electrical potential of the package and pass through an accident current. Similarly, electrolytic capacitors are fixed to a grounded chassis using a metal clamp in many scenarios. Thus, an electrolytic capacitor often has a parasitic capacitance between the package and chassis. The parasitic capacitance may feed a CM noise current, which perhaps results in amplifying the noise. Therefore, this section presents an experimental study to investigate the effects of the parasitic capacitance and develop an EMI simulation modeling method.

3.4.2 Measurement of Conducted Noise Emission

Table 3.3 shows the specifications of the electrolytic capacitors under test. In this research, two electrolytic capacitors were used for the experimental studies. The DUTs had a different structure although the rating capacitance and size were the same. In the aluminum container of the standard type, the outermost layer of the electrolytic capacitor was connected to the aluminum container by an impedance

derived from an electrolyte and oxide film [72]. For the heat dissipation type, the top side of the cathode foil was connected to the aluminum container to make the cathode and aluminum case thermally conductive.

TABLE 3.3: Specification of the electrolytic capacitors

DUT	1	2
Type	Standard	Heat dissipation
Rating voltage	450 V	450 V
Nominal capacitance	630 μF	630 μF
Size	ϕ35 $\times$ 50L	ϕ35 $\times$ 50L
Outer sleeve	PET	PET

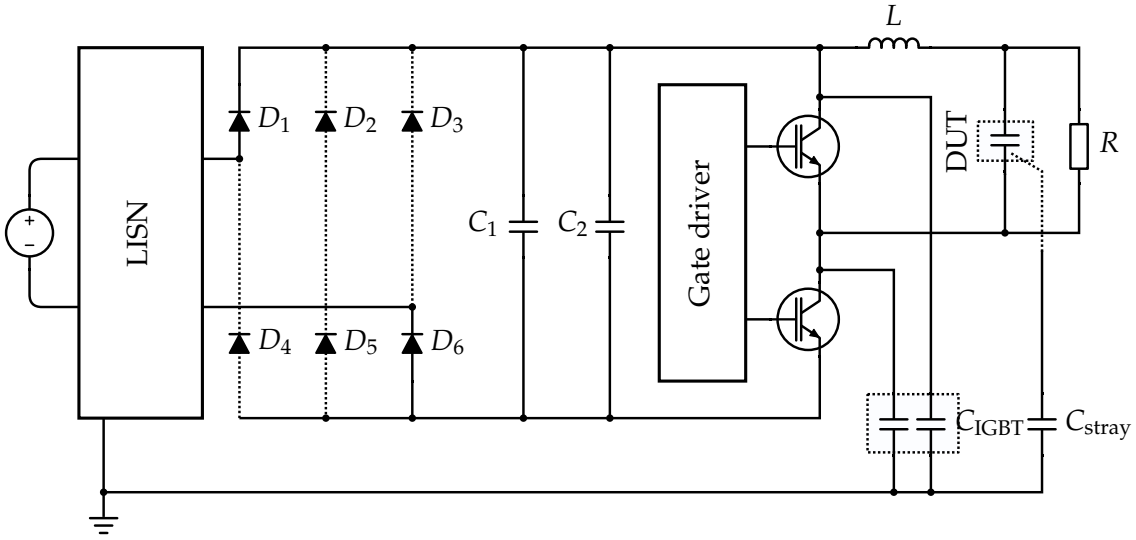

FIGURE 3.9: Configuration of the experimental system

Fig. 3.9 shows the configuration of the experimental system. A buck converter that included the DUT as the output capacitor was used in the experiments to test the impact of a parasitic impedance of the electrolytic capacitor. The three-phase diode rectifier circuit (D_1 to D_6) was embedded in the input side of the converter, and two IGBTs (FGW30N60VD) were used as switching devices. Additionally, snubber capacitors (C_1, C_2) were connected in parallel. The smoothing inductor L at the output side was 450 μH, and the load resistance R was 47 Ω.

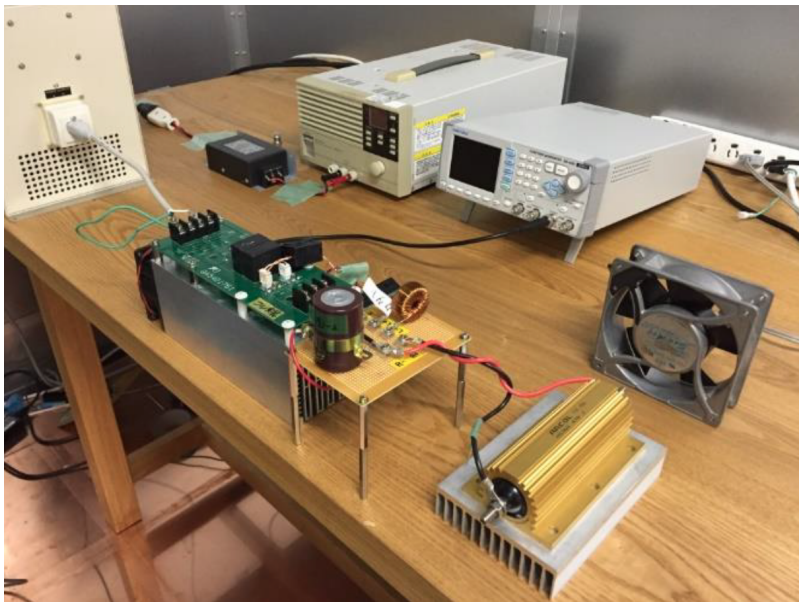

FIGURE 3.10: Experimental setup of the system

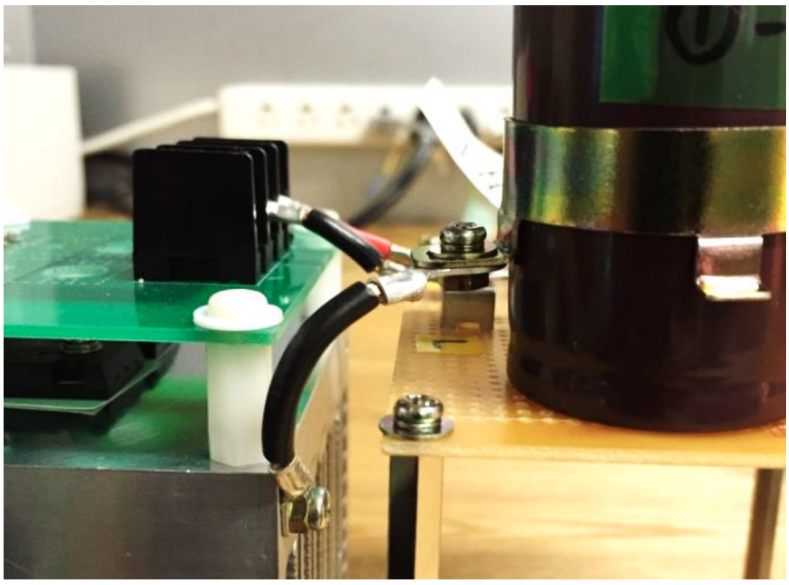

FIGURE 3.11: Grounding of the capacitor clamp

Fig. 3.10 shows the experimental setup, and Fig. 3.11 shows a connection between the capacitor clamp and heatsink. The electrolytic capacitor was mounted on the circuit board for high-repeatable measurements since the physical distance with other devices affected the parasitic impedance. The EMI filter (HF2030AUPF, Soshin) enabled the effects of noise from the DC power supply to be minimized, and the gate drive circuit fed the power from a 9 V battery to suppress the influence of external noise as much as possible. In addition, a metal-clad resistor was

used as the load because of the better impedance characteristics compared with other types such as carbon films. The operating condition of the buck converter was an input voltage of 100 V, switching frequency of 25 kHz, and switching time ratio of 50%. The conducted noise voltage in the frequency domain was measured under the following conditions:

- Condition A: Heat dissipation type (DUT 2) with a grounded clamp
- Condition B: Standard type (DUT 1) with the grounded clamp
- Condition C: Standard type (DUT 1) without floating the clamp

By feeding DC power at the input port of the buck converter, diodes D_2 to D_5 were constantly turned off. Furthermore, owing to the dependency of the stray capacitance between the electrolytic capacitor and capacitor clamp on the tightness of the capacitor clamp, the same type of capacitor band was attached to each capacitor and never adjusted until the measurement was completed. A line impedance stabilization network (LISN) (KNW-403D, Kyoritsu Electronics) and a spectrum analyzer (ESR Test Receiver, Rode and Shwarz) were used to measure the peak spectrum measurement to measure the conducted noise emission. KNW-403D is a V-type LISN and can measure the noise terminal voltage separately for differential and common modes.

Figs. 3.12 and 3.13 show the measurement results of the noise terminal voltage. The measurement results confirmed that both the CM and DM noises increased when the capacitor clamp was grounded. In particular, the CM noise increased in almost all frequency bands. In the high-frequency band, the increase in the noise terminal voltage for both CM and DM was remarkable. In addition, the increase amount was larger for the heat dissipation structure than for the standard structure. The reason for this was considered to be that the impedance from the cathode to the capacitor clamp reduced because the cathode was directly connected to the aluminum container.

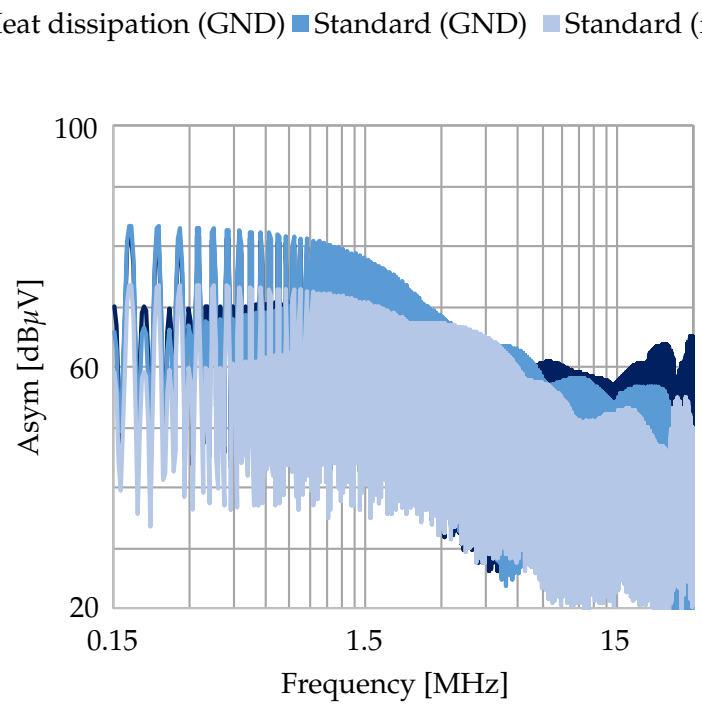

FIGURE 3.12: Measured asymmetrical noise spectrum

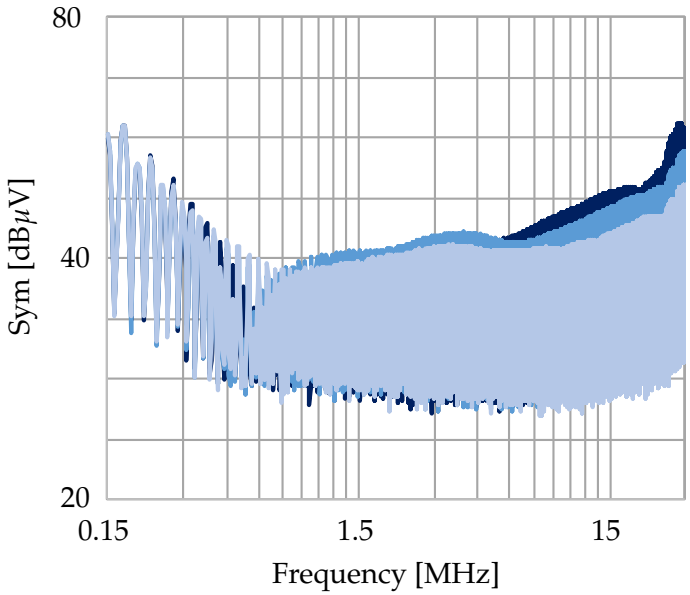

FIGURE 3.13: Measured symmetrical noise spectrum

3.4.3 Mechanism of Leakage Current through a Capacitor Clamp

An equivalent circuit of the electrolytic capacitor, including the capacitor clamp, is discussed here to establish a modeling approach and understand the EMI mechanism. To achieve this objective, this section presents a simple equivalent circuit that is easy to understand and enables rapid simulation, rather than a high-precision equivalent circuit that considers the chemical characteristics of the electrolytic capacitor.

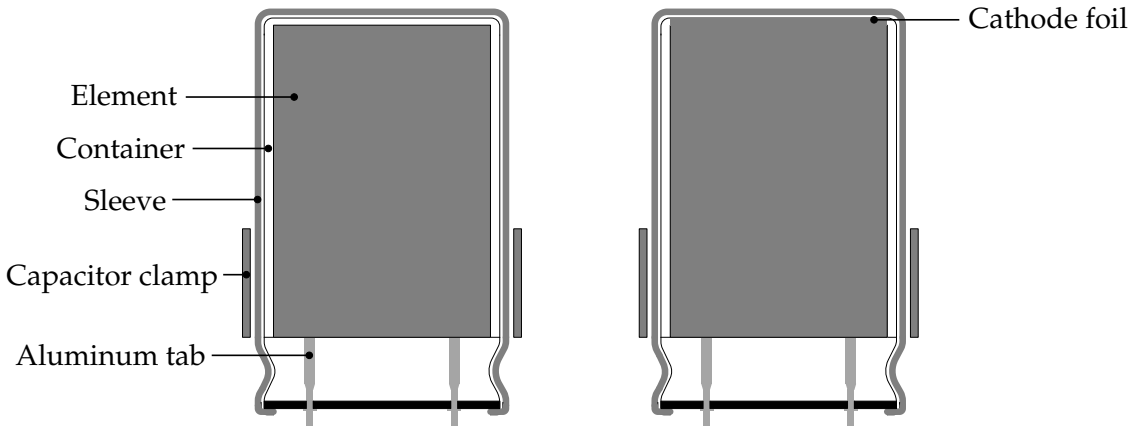

FIGURE 3.14: Cross-sectional view of the electrolytic capacitor

Figs. 3.14 (a) and (b) show a cross-sectional view of the electrolytic capacitor. When a metal capacitor clamp was attached to the electrolytic capacitor, a stray capacitance was formed between the metal container of the electrolytic capacitor and the capacitor clamp. The value of the floating capacitance depended on the thickness of the outer sleeve, dielectric constant of the sleeve, and tightness of the capacitor clamp. For an electrolytic capacitor with a standard structure, a relatively large resistance component is generally considered to exist between the outermost layer of the element and the container; therefore, it can be expressed as a series circuit of stray capacitance and resistance. For the heat dissipation structure, part of the cathode foil was in contact with the metal container. The above indicates that a simple equivalent circuit for both structures can be expressed by using a series circuit of stray capacitance and parasitic resistance.

Fig. 3.19 shows the simulation model of the experimental system with the grounded capacitor clamp. Since all the elements were considered ideal elements in the circuit simulation, it was necessary to make a simple equivalent circuit for

each component. Several reports have shown that the simulation accuracy is improved by using simple equivalent circuits, and this is considered to be appropriate under several MHz simulations [73], [74]. Parasitic inductance was also considered for the wiring structures such as the DC bus. For the values of each element, the parameters were calculated by fitting them to the impedance frequency characteristics measured using an impedance analyzer (E4990A, Keysight).

Figs. 3.15 and 3.16 show the measured cathode voltage and leak current via the capacitor clamp. A high-frequency current was generated when the cathode voltage of the electrolytic capacitor changed rapidly in both turn-on and turn-off conditions. Additionally, more high-frequency current was generated during turn-on when the change was more rapid. This was because the high-speed switching operation induced a resonance current in many resonance paths. Therefore, when the cathode-to-ground voltage changed rapidly, the high-frequency current increased. This can be observed in Figs. 3.15 and 3.16, where the turn-on time, when the switching was relatively fast, was larger than the turn-off time.

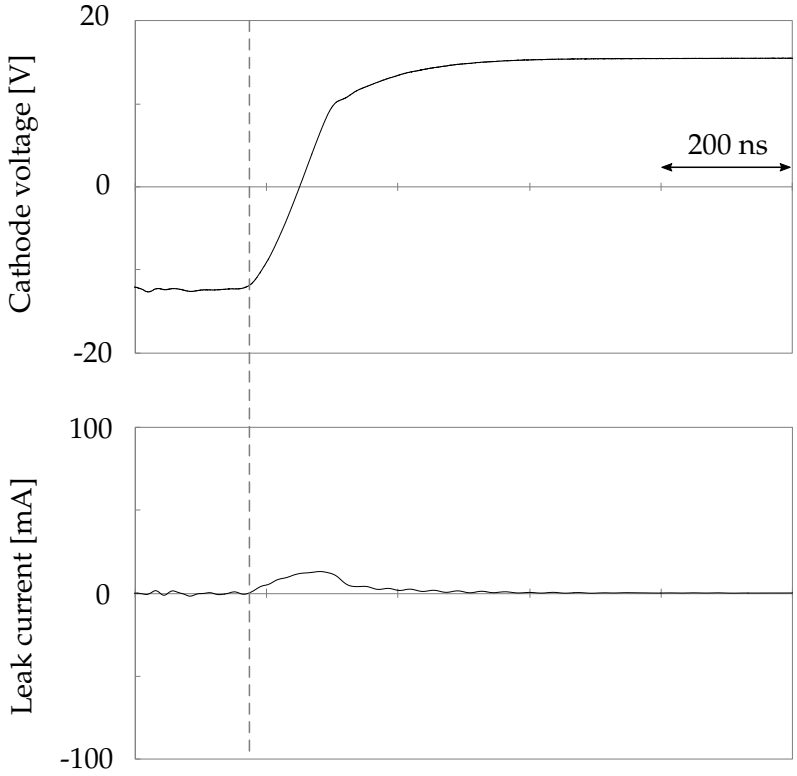

FIGURE 3.15: Measured turn-off leak current

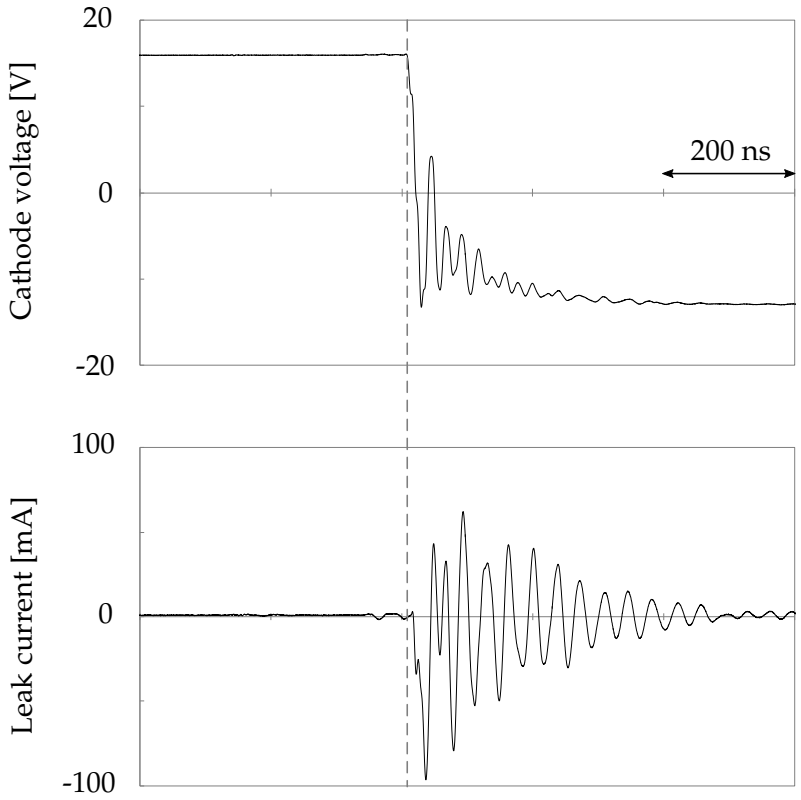

FIGURE 3.16: Measured turn-on leak current

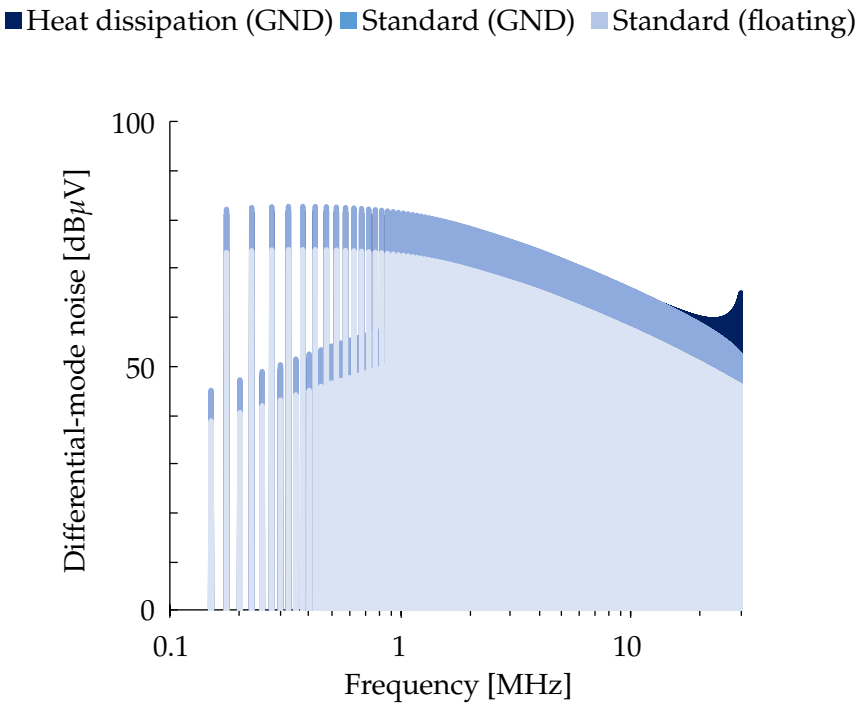

FIGURE 3.17: Simulation differential-mode noise spectrum

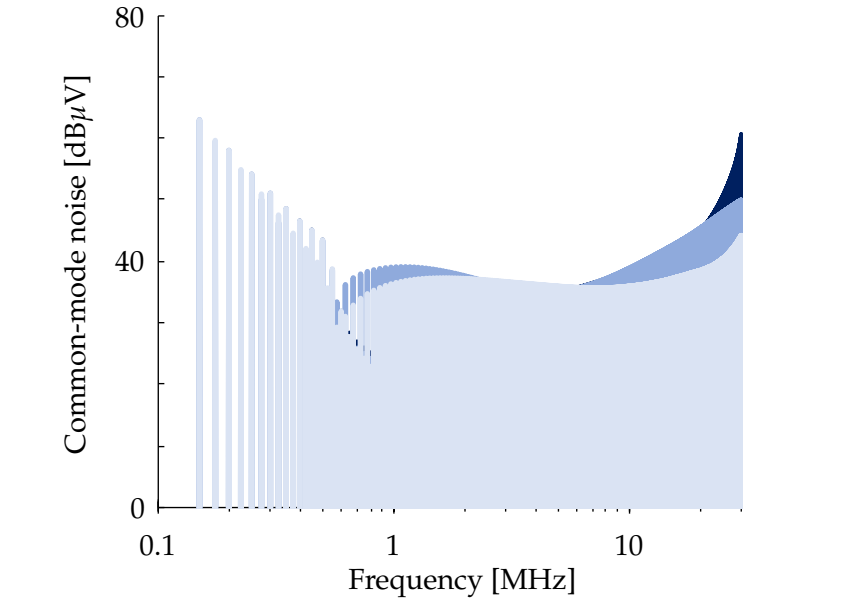

FIGURE 3.18: Simulation common-mode noise spectrum

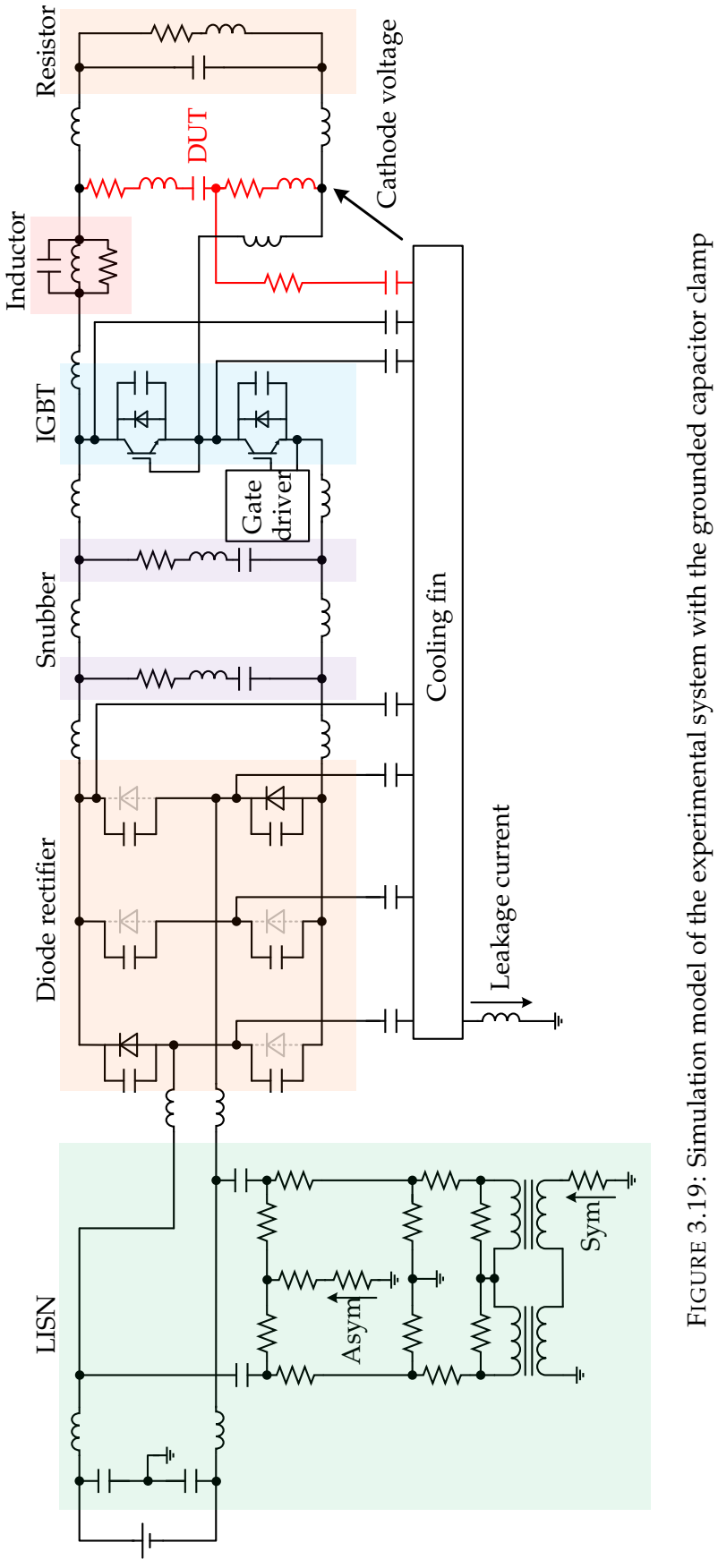

FIGURE 3.19: Simulation model of the experimental system with the grounded capacitor clamp

3.4.4 Suppression of the Leakage Current

The parasitic capacitance should be reduced to suppress the leakage current. Assuming the dielectric constant of the capacitor sleeve is ε, the stray capacitance (C_S) can be expressed by the following equation:

$$C_S = \varepsilon \frac{S}{d} \tag{3.1}$$

where d is the thickness of the sleeve, and S is the contact area. To reduce C_S, d should be made thicker. In this study, the sleeve was made thicker by wrapping a common vinyl tape around the outside of the capacitor sleeve. The thickness of the wrapping was approximately 1 mm.

Figs. 3.21 and 3.22 show the measured conducted noise spectrum with and without taping. In both results, the noise terminal voltage was reduced in almost all frequency bands. For more EMI reduction, non-conductive materials can be used for the clamp. For instance, nylon-made clamps are available on the market, although they have limited thermal conductivity.

FIGURE 3.20: Picture of an electrolytic capacitor with taping

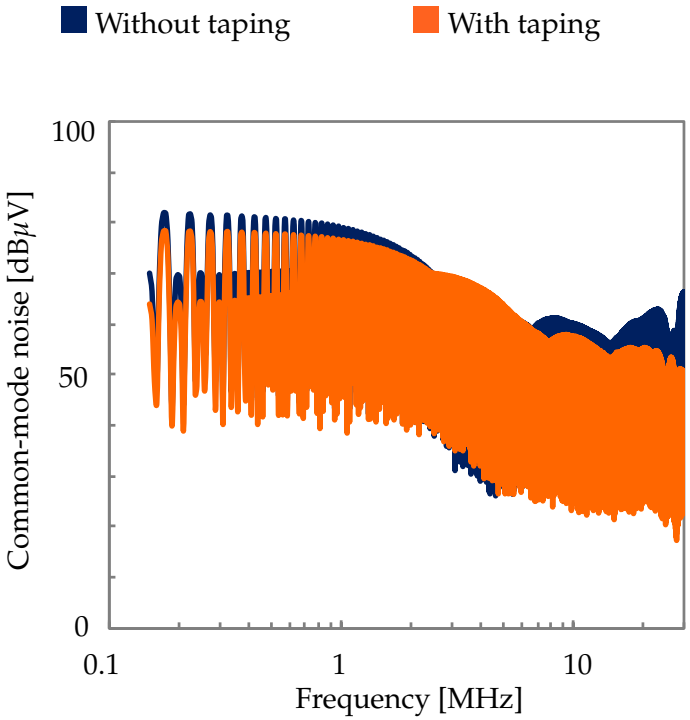

FIGURE 3.21: Simulation common-mode noise spectrum

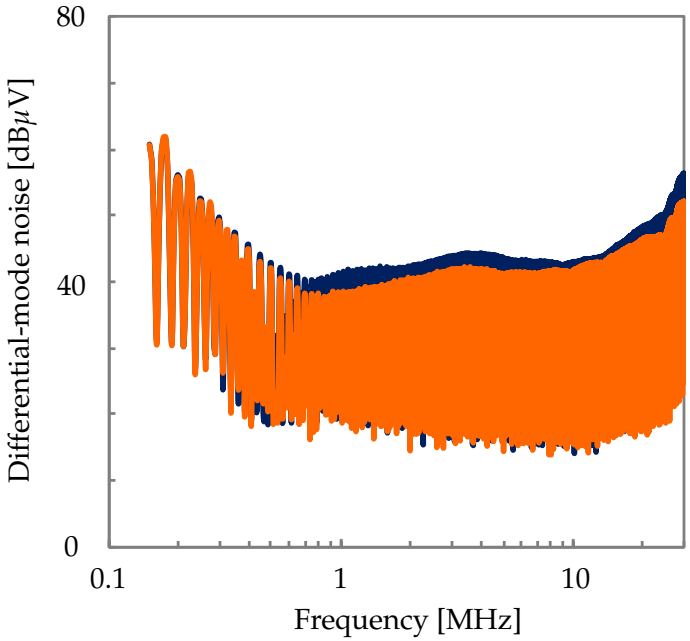

FIGURE 3.22: Simulation common-mode noise spectrum

3.5 Modeling Methodologies: OFF-State Impedance of MOSFET

3.5.1 Introduction

The high-speed switching of power semiconductors is a key factor toward next-generation power converters [75]. For instance, WBG power devices, including SiC MOSFETs and GaNFETs, have the potential to achieve higher speed switching compared with conventional Si MOSFETs. However, a high dv/dt switching often causes a switching oscillation [76]. Negative aspects of switching oscillation primarily include power loss, voltage overshoot, and EMI noise. Hence, it is necessary to understand the switching oscillation mechanism to introduce theoretical guidelines in oscillation suppression.

In this context, MOSFET simulation models have been receiving increasing interest to understand the oscillation mechanism or predict oscillation waveforms. Conventional simulation models primarily consist of on-resistance, parasitic capacitance, and wiring inductance, which are added to an ideal switch [77]–[79]. However, the models do not consider the R_{oss} of MOSFETs when simulating an oscillation waveform, although it affects the oscillation waveform. The R_{oss} of a MOSFET is defined as an equivalent series resistance of output capacitance (C_{oss}) that impacts on power loss during a switching transient [80], [81]. Moreover, MOSFET datasheets commonly do not indicate the parameter, and only a few application notes mention R_{oss} [82], [83]. Thus, the impact of R_{oss} on a switching oscillation is still unclear and requires further investigation.

This section presents a MOSFET model including R_{oss} and quantifies the impact on a damped oscillation waveform experimentally. After a characterization of the R_{oss} value using an impedance analyzer, the proposed MOSFET model was used to create a buck converter simulation model. Subsequently, a comparison between simulation and experimental waveform revealed the impact of R_{oss} on a switching oscillation waveform and validated the proposed MOSFET simulation model. For the experimentation, two MOSFETs were implemented into identical buck converters, respectively, and a dedicated test setup enabled a switching oscillation waveform without disturbance to be obtained, resulting from electromagnetic couplings. Finally, a comparison of the waveform and damping factor quantified the impact of R_{oss} on the oscillation waveform. The damping factor

comparison indicated that the proposed simulation model suppressed deviation by 87% at maximum.

3.5.2 Proposed MOSFET Simulation Model with R_{oss}

TABLE 3.4: MOSFET Specification

	Device	Type	Manufacturer	Specification
DUT A	C2M0280120D	SiC MOSFET	CREE, Inc.	1200V, 10A, 0.28 Ω
DUT B	C2M0080120D	SiC MOSFET	CREE, Inc.	1200V, 36A, 0.08 Ω

Table 3.4 lists the specifications of the MOSFETs for the simulation and experimentation. Fig. 3.23 shows a conventional and the proposed MOSFET models to simulate a turn-off switching oscillation. The proposed model included R_{oss} in parallel with an ideal switch that synchronizes with the on/off states of the MOSFET because R_{oss} only affects the off state. For C_{ds}, C_{gd}, and C_{gs}, a CV curve analyzer (CS-603A, IWATSU) was used to characterize C_{iss}, C_{oss}, and C_{rss}, and enable each capacitance to be calculated using the following equations:

$$C_{iss} = C_{gs} + C_{gd}, \qquad C_{oss} = C_{ds} + C_{gd}, \qquad C_{rss} = C_{gd} \tag{3.2}$$

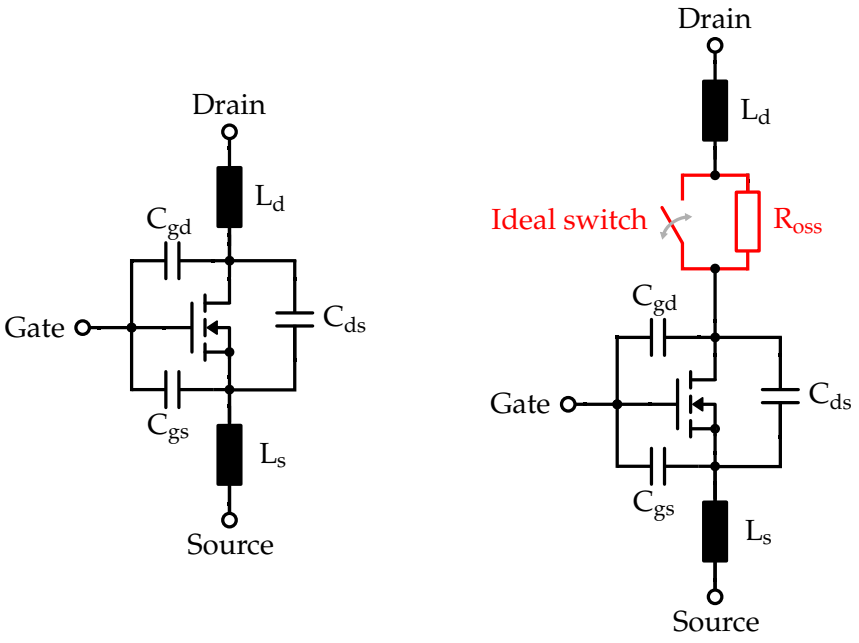

(A) Conventional (B) Proposed

FIGURE 3.23: MOSFET simulation model

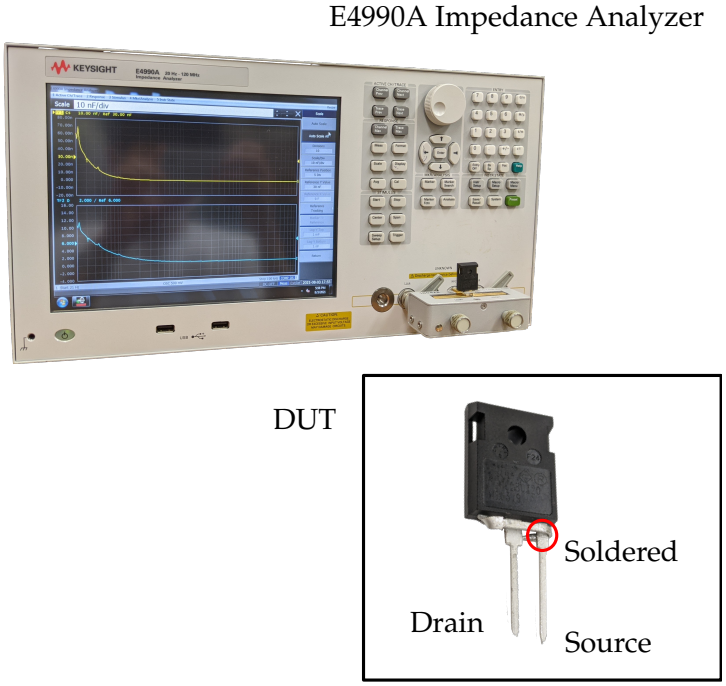

FIGURE 3.24: R_{oss} measurement setup

Fig. 3.24 shows the R_{oss} measurement setup. Figs. 3.27 and 3.28 show the measured R_{oss} characteristics of devices A and B. Several methods can be used to measure and model the R_{oss} or C_{oss} loss of a MOSFET [80], [81], [84]. R_{oss} was measured using an impedance analyzer (E4990A, Keysight), which meant a small-signal measurement. Regarding the measurement setup, the gate- and source-terminal of the MOSFET were connected directly through soldering to maintain an off-state. Using a function of the impedance analyzer, R_{oss} curves were obtained under a DC bias voltage in the range from 10 to 40 V. The frequency sweep started from 100 kHz and stopped at 50 MHz.

The measured results indicated that the R_{oss} curves depended on frequency rather than a bias voltage. For the simulation model, a R_{oss} value was extracted at the resonant frequency of an oscillation waveform. If the switching oscillation is not constant, the R_{oss} should be modeled as a frequency-dependent component, which can be realized by using a function of circuit simulator or modeling in the form of an equivalent circuit. However, for simplification, this thesis presents results simulated using PSIM (Powersim, Inc.) software under the assumption that the oscillation switching was constant.

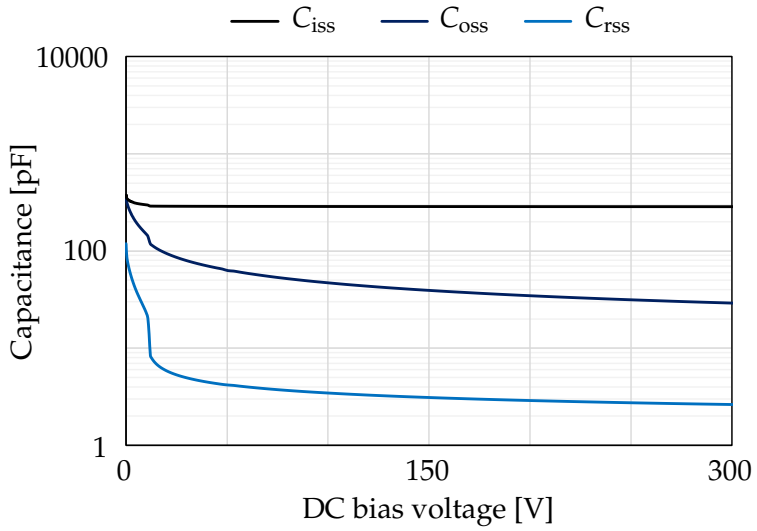

FIGURE 3.25: CV curves of DUT A

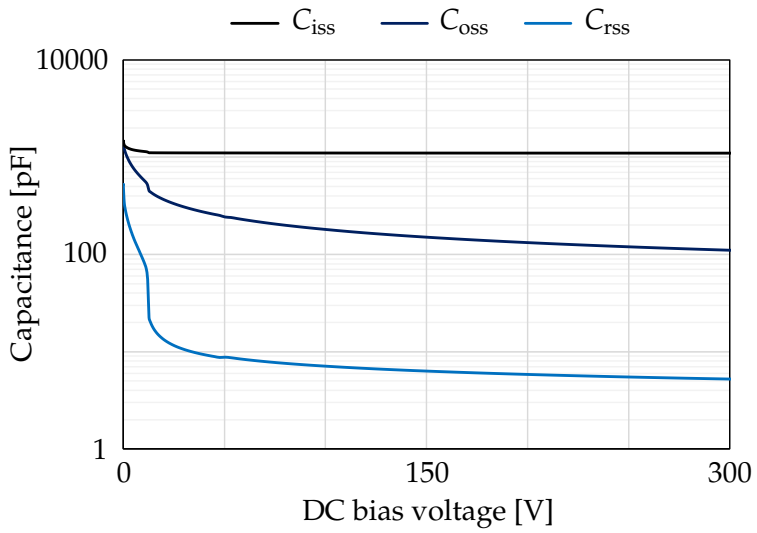

FIGURE 3.26: CV curves of DUT B

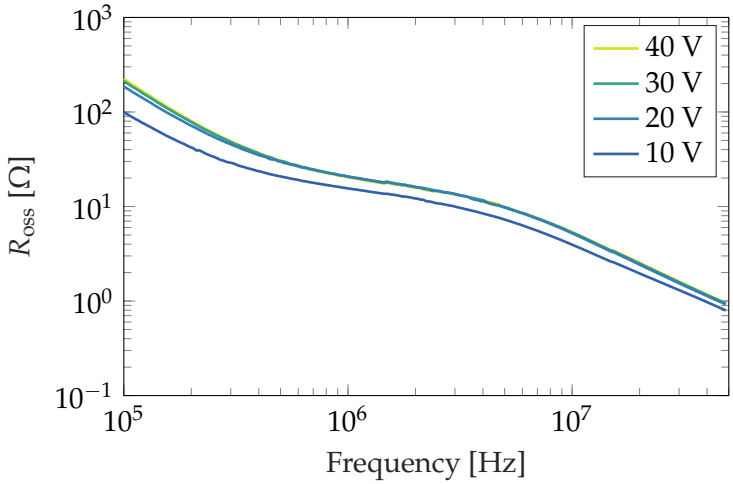

FIGURE 3.27: Measured R_{oss} of DUT A

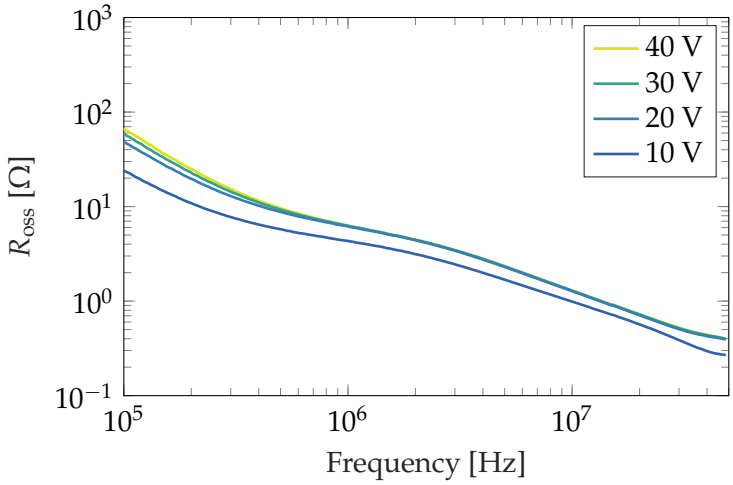

FIGURE 3.28: Measured R_{oss} of DUT B

3.5.3 Mechanism of Damped Switching Oscillation

Fig. 3.29 shows a simulation model of the buck converter for experimental studies. The buck converter consisted of a MOSFET, a freewheeling diode, an external inductor L, and an input capacitor C_{in} mounted on the main circuit board (KIT8020CRD8FF 1217P-1, CREE, Inc.). The input capacitor C_{in} with L_{in} and R_{in} represents multiple film capacitors for model simplification. For the DUT of the simulation model, conventional and proposed MOSFET models (Fig. 3.23) were used to compare the effect of R_{oss}.

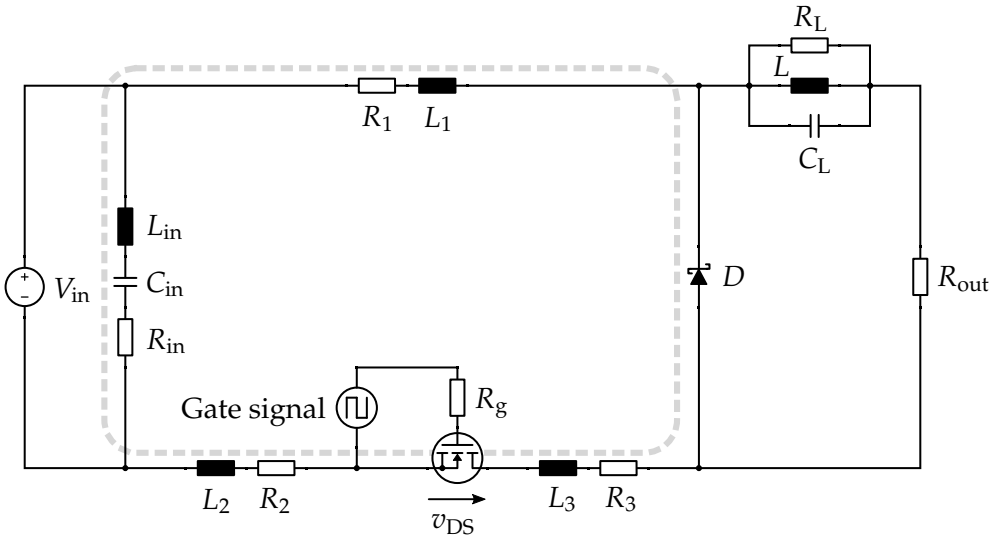

FIGURE 3.29: Simulation model of the buck converter

TABLE 3.5: Parameters for the simulation model

Symbol	Value	Symbol	Value	Symbol	Value
V_{DC}	120 V	L_1	6.93 nH	R_1	96.4 mΩ^{*a}/94.7 mΩ^{*b}
R_{in}	32 mΩ	L_2	173 nH	R_2	105 mΩ^{*a} /102 mΩ^{*b}
C_{in}	5.12 μF	L_3	6.19 nH	R_3	93.5 mΩ^{*a}/91.0 mΩ^{*b}
L_{in}	7.8 nF	L_d	9 nH	R_{out}	30 Ω
L	182 μH	L_s	9 nH	R_{oss}	2.4 Ω^{*a}/0.9 Ω^{*b}

*a for DUT A, *b for DUT B

Table 3.5 presents the parameter list of the simulation model. According to prior studies, there are two types of switching oscillations: damped and undamped [85]. This study focused on the damped oscillation in a turn-off process to investigate the damping effect of the R_{oss} of a MOSFET. The damped oscillation phenomenon is commonly due to an RLC resonance caused by a switching transient. In Fig. 3.29, the dotted line represents a primary oscillation current path. Parasitic impedance in the current path, such as wiring inductance and parasitic capacitance of a MOSFET, determines the damped oscillation waveform. Accordingly, the simulation model of the buck converter included the main parasitic parameters extracted by the impedance analyzer. Since the resonant frequency of a turn-off switching oscillation was 23 MHz for DUT A and 19 MHz for DUT B, the R_{oss} values of the MOSFET model were set to 2.4 Ω and 0.9 Ω, respectively.

Regarding the wiring resistances R_1, R_2, and R_3, each resistance value was extracted at the resonance frequency of oscillation waveform, which was given by a measured waveform, to consider the conductor skin effect.

3.5.4 Experimental Verification of the Proposed MOSFET Model

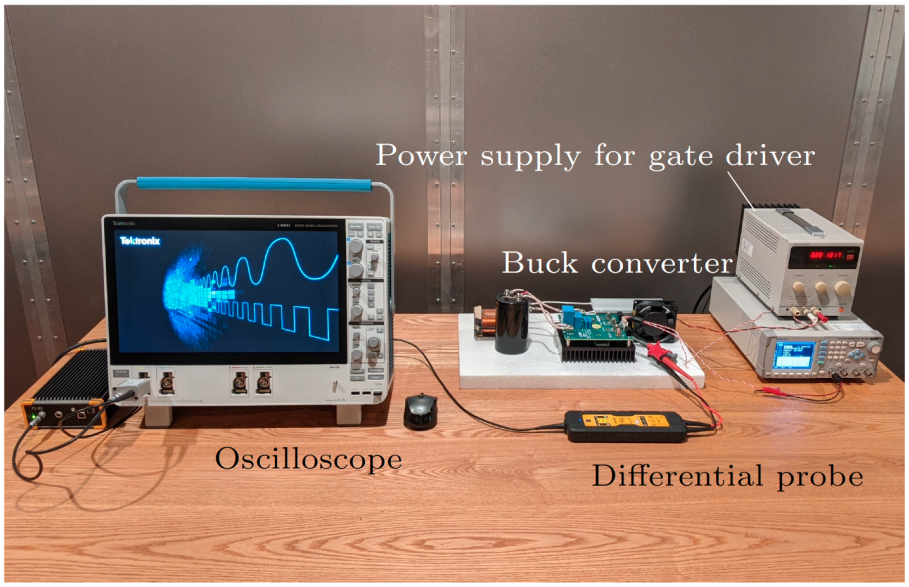

FIGURE 3.30: Measurement setup

Fig. 3.30 shows the experimental setup of the buck converter in a shielded room for a lower EMI environment. Measuring a switching oscillation waveform requires careful attention to the probe setup [86]. A differential probe (Bumblebee, 400 MHz, PMK), which has a high CM rejection ratio, was used to avoid distorting the oscillation waveform. It was directly connected to the leads of the MOSFET. For the operating condition of the buck converter, the switching frequency was 50 kHz, and the duty ratio was 0.3. The input voltage (V_{DC}) was set to 120 V. For the experimentation of DUTs A and B, the two buck converters had an identical configuration.

Figs. 3.31 and 3.32 show damped oscillation waveforms to compare the simulation and measurement results. For the simulation waveform without the R_{oss} of the MOSFET, the waveform amplitude had a noticeable deviation in the oscillation amplitude compared with the experimental waveform. In contrast, for the proposed model, the oscillation simulation was in better agreement with the measured waveform.

TABLE 3.6: Damping factor comparison

	DUT A			DUT B		
V_{DC}	40 V	80 V	120V	40 V	80 V	120V
Simulation w/o R_{oss}	0.05	0.05	0.05	0.07	0.07	0.07
Experiment	0.19	0.19	0.20	0.15	0.15	0.15
Proposed model	0.23	0.21	0.22	0.16	0.14	0.14

Table 3.6 lists the damping factors that were calculated from the positive side envelope of the oscillation. In addition to the measurement conditions of Figs. 3.31 and 3.32, V_{DC} was also set to 40 and 80 V to compare the damping factor under several oscillation amplitudes. For the calculation, logarithmic decrements obtained using ten peaks of an oscillation waveform were used to quantify the damping factor. As observed in the waveform comparison, regardless of the V_{DC} value, the simulation results of the proposed model were in better agreement with the measured ones compared with the simulation model without R_{oss}. Particularly for DUT A at 120 V, compared with the simulation without R_{oss}, the proposed model suppressed the deviation with the experiment to 0.02, which was equivalent to an 87% error reduction. Therefore, the proposed simulation model was validated and feasible for simulating a damped oscillation waveform.

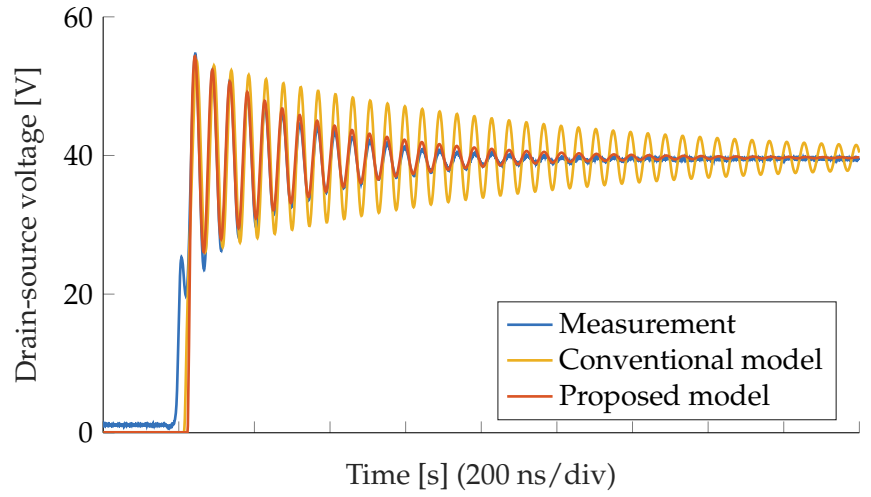

(A) DUT A, $V_{DC} = 40V$

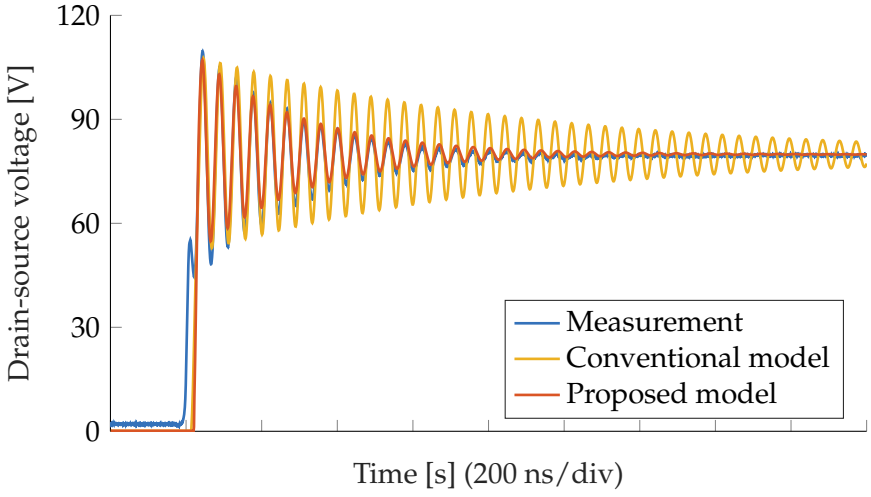

(B) DUT A, $V_{DC} = 80V$

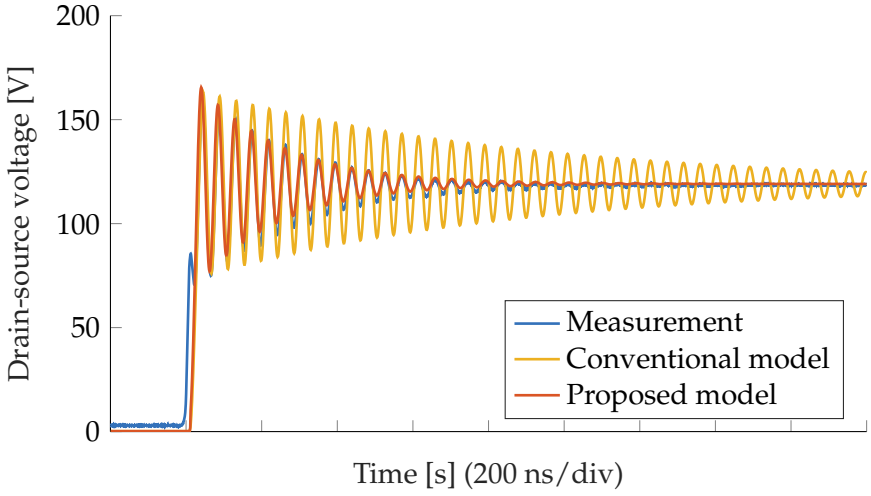

(C) DUT A, $V_{DC} = 120V$

FIGURE 3.31: Turn-off oscillation waveform of DUT A

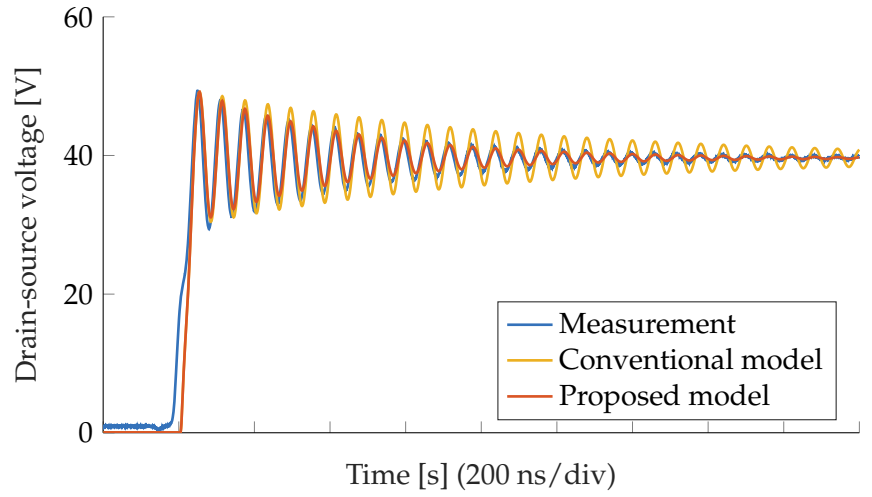

(A) DUT B, $V_{DC} = 40V$

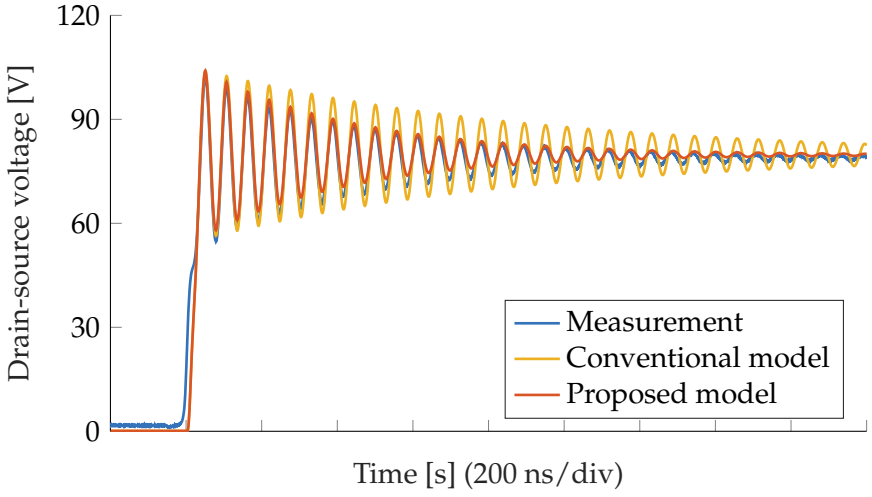

(B) DUT B, $V_{DC} = 80V$

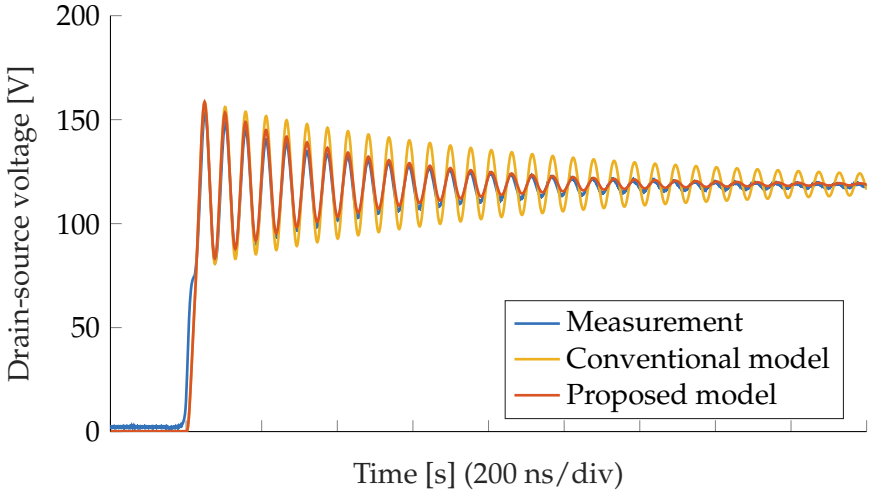

(C) DUT B, $V_{DC} = 120V$

FIGURE 3.32: Turn-off oscillation waveform of DUT B

3.6 Comparison of Simulation and Experiment Waveforms

The measured and simulated waveforms of the noise injection system were compared to validate the simulation model of the noise injection system and investigate the EMI mechanism. Figs. 3.33 (a)-(e) and 3.34 (a)-(e) show the waveform comparisons between the measurement and simulation, respectively, during a switching action of the converter MOSFET. A conducted noise appeared in the CAN bus owing to the switching action of the converter MOSFET and diodes. Thus, the waveform comparisons were confined to a switching transient of the converter MOSFET. The drain–source voltage of the MOSFET, CM current of the ground line, induced noise of the CAN bus, DM noise in the communication line, and receiver (Rx) output signal of the transceiver were measured with an oscilloscope (Teledyne Lecroy, WaveRunner 8254-MS). Figs. 3.4 and 3.5 indicate all the measurement points. For the DM noise in the communication line, only the simulated waveforms are shown because a passive/active probe for measuring the voltage would change the impedance of the communication line and skew the waveforms.

For the CM current of the ground line, as shown in Figs. 3.33 (b) and 3.34 (b), a damped oscillation occurred with the converter switching transition observed in Figs. 3.33 (a) and 3.34 (a). This oscillation occurred because the CM voltage fluctuation of the converter caused a resonance current in the CM noise loop; the resonance frequency depended on the parasitic impedance of the loop [3], [87]. Thus, as shown in Figs. 3.33 (c) and 3.34 (c), a ringing waveform also appeared in the CAN bus, and the ringing frequency was identical to that of the ringing noise of the ground line. The ringing noise flowed into the transceiver as CM noise. Subsequently, the CM noise was converted to a DM noise Figs. 3.33 (d) and 3.34 (d). According to the Rx output signal of the transceiver shown in Figs. 3.33 (e) and 3.34 (e), logical flips corresponding to the “dominant” state of the communication line occurred simultaneously with the ringing noise. In the experimental condition, the CAN controller maintained a “recessive” signal state, which corresponded to 5 V of the Rx output. In other words, the logical flips resulted in transmitting error signals because the receiver read them as different data from the original. In other words, the logical flips of Rx output occurred with the switching transient of the converter MOSFET.

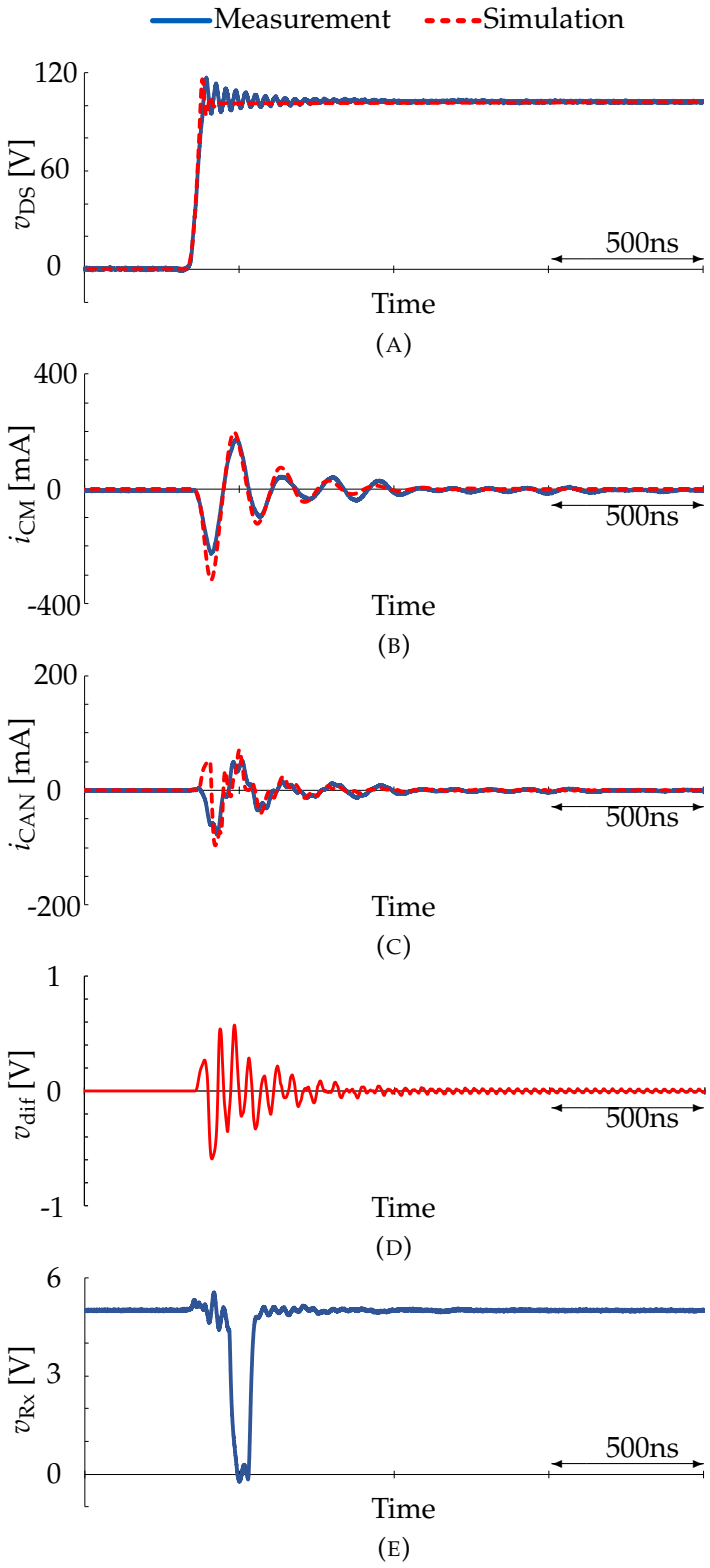

FIGURE 3.33: Measured and simulated waveforms of the noise injection system with the MOSFET turned off: (A) Drain-source voltage, (B) CM noise current in the ground line, (C) induced noise in the CAN bus, and (D) DM voltage at the transceiver inputs (E) CAN Rx output signal of the transceiver

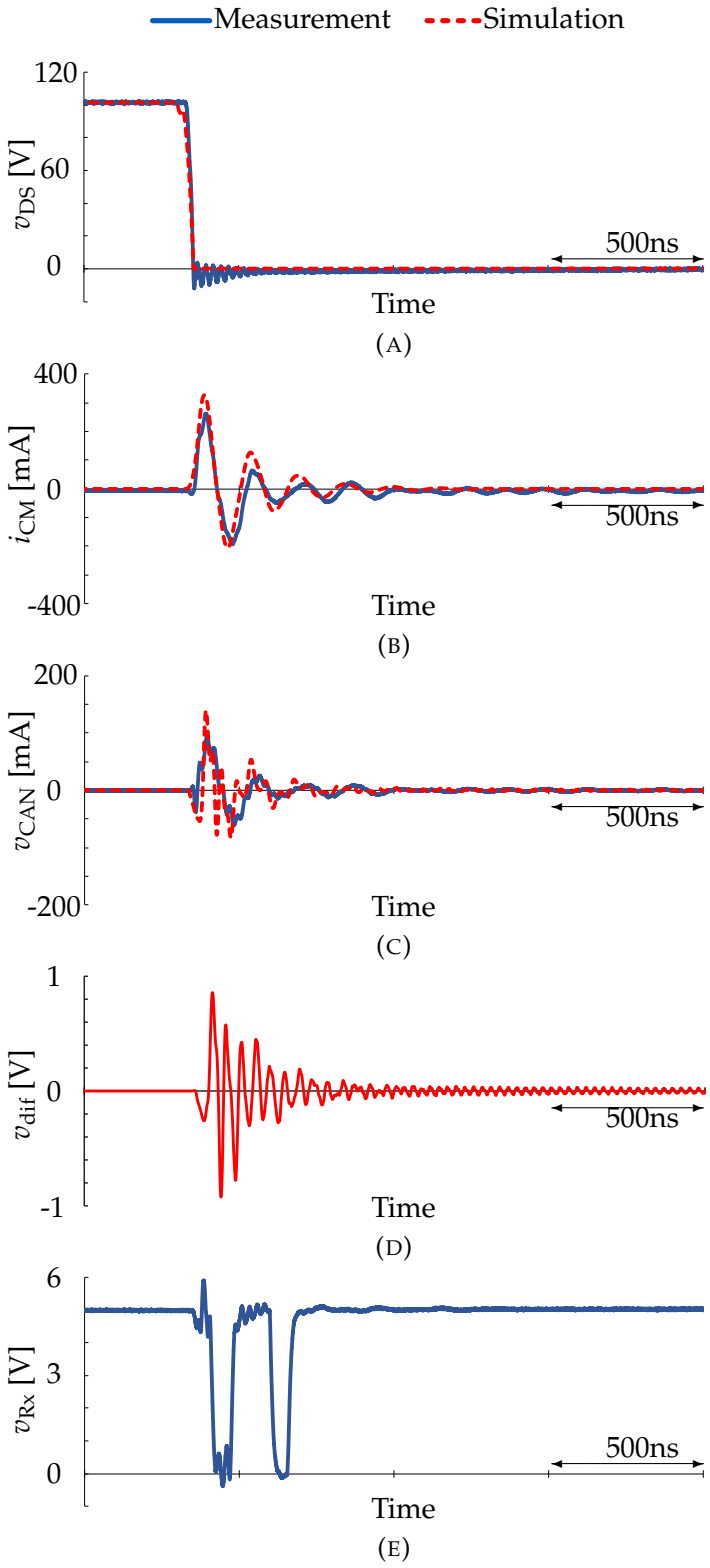

FIGURE 3.34: Measured and simulated waveforms of the noise injection system with the MOSFET turned on: (a) Drain-source voltage, (b) CM noise current in the ground line, (c) induced noise in the CAN bus, and (d) DM voltage at the transceiver inputs (e) CAN Rx output signal of the transceiver

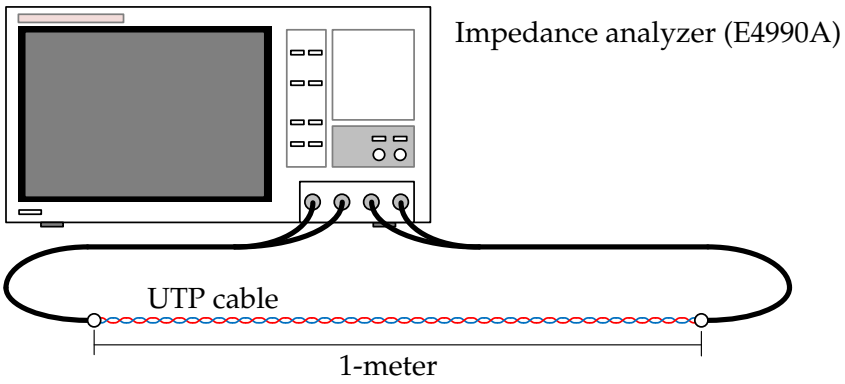

FIG. 3.35. Measurement setup to obtain an impedance characteristics of the UTP cables

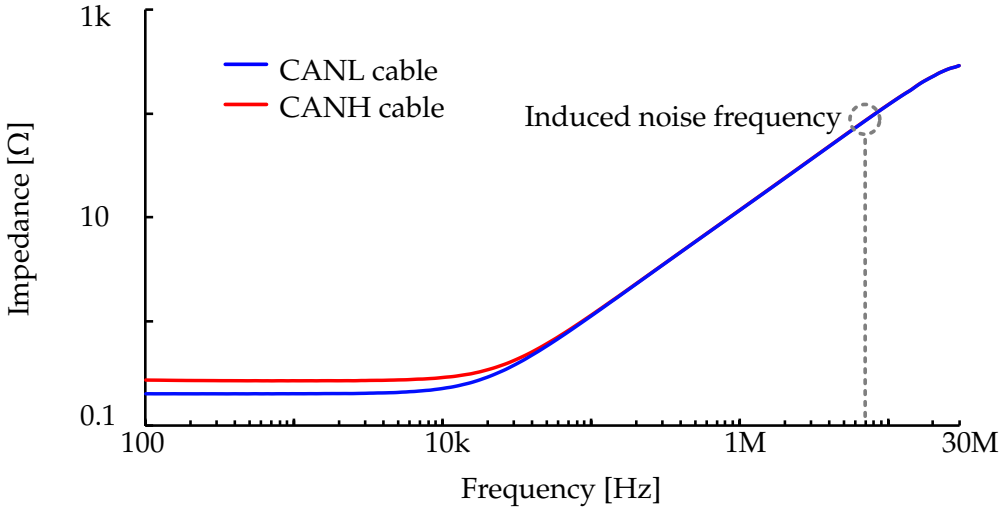

FIGURE 3.36: Measured impedance characteristics of the CANH and CANL communication cable

As a further concern, assuming that the CANH and CANL ports of the transceiver and the communication cables have balanced impedance characteristics, a CAN has a strong immunity to CM noise in a communication line because it employs a differential signaling method. However, practically, the transceiver has an intrinsic impedance and it is unbalanced at the induced CM noise frequency (Fig. 3.6). In contrast, the impedance of the communication cables, which was measured as shown in Fig. 3.35, is almost balanced at the noise frequency (Fig. 3.36). The CM noise is partly converted to DM noise and may affect the communication signal, which is called the "mode-conversion" phenomenon [88], and results in communication failure.

3.7 Time-Domain Analysis of the CAN Error Mechanism

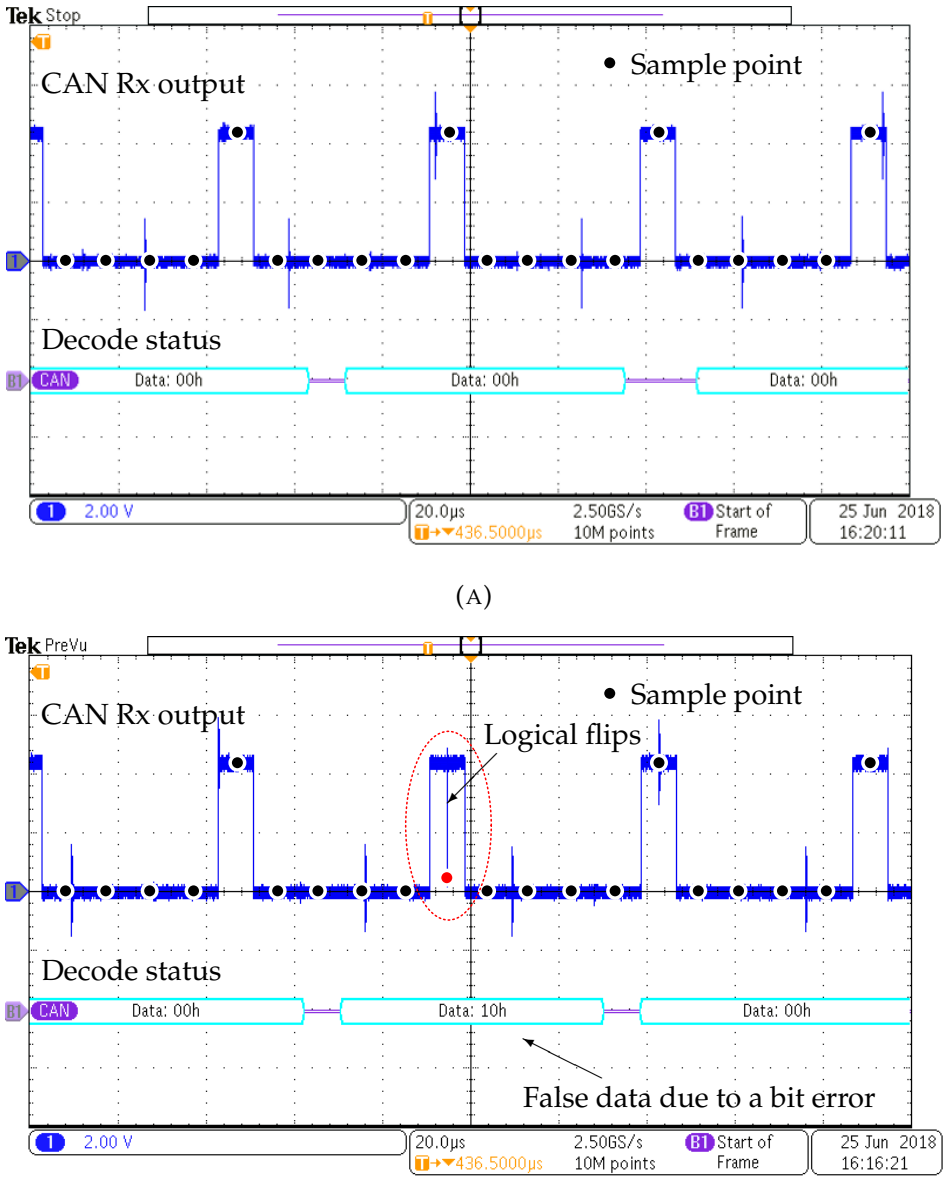

FIGURE 3.37: Measured CAN Rx output under operation of the buck converter and decoded signal state: (a) Without bit error, (b) captured bit error

In addition to discovering how the logical flips occur, the CAN error mechanism should be investigated. The Tx node transmits units of a bit array, and the receiver reads bit logic samples a single point per bit. Generally, the sample point

is located from 60% to 80% of the bit time length; the sampling timing varies slightly with each bit depending on the communication signal. Therefore, CAN errors occur when the logical flips coincide with a sample point.

Fig. 3.37 shows the measured Rx output of the transceiver under the operation of the converter and its decoded data. To verify the EMI mechanism experimentally, we measured the Rx output signal with an oscilloscope (Tektronics, MDO3054), which had a decode function enabling it to capture the bit logic. During the measurement with the noise injection system, the buck converter operated at a constant switching frequency and duty ratio (30 kHz, 0.5), and the CAN system repeatedly transmitted data frames containing identical data. Capturing the same segment of the data frame enabled the acquisition of the normal and error signal waveforms because switching noise randomly spiked in the communication signal. When no error occurred, all the bytes indicated "00h," referring to the decoded data (Fig. 3.37 (a)). This corresponded to the transmitter (Tx) node sending 8 bits of "00h." However, according to Fig. 3.37 (b), the middle byte indicated "10h," where the original byte was "00h." This result occurred because the logical flips occurred coincidentally with a CAN sample point, and the error bit was read by the Rx node. Generally, a bit error causes the Rx node to detect communication failure and degrades the communication speed and reliability.

3.8 CAN Error Rate Evaluation

3.8.1 Bit Error Rate

The BER is an index used to evaluate the robustness of serial communication [89], [90]. If the number of bits transmitted in a communication system is N_{tx} and the number of bits that cannot be received normally is N_{error}, the BER is calculated using Equation 3.3.

$$BER = \frac{N_{\text{error}}}{N_{\text{tx}}} \cdot 100 \tag{3.3}$$

In the CAN standard defined in ISO11898, the signal level of the bus is read at the sample point set by the arbitrary bit timing. As a result of the verification described in the previous section, if a logic inversion caused by noise voltage is read at the CAN sample point, an error state different from the original transmission signal will occur. In addition, the CAN protocol detects bit errors, staff errors,

cyclic-redundancy-check (CRC) errors, form errors, and acknowledgment (ACK) errors, and transmits error flags and increments the error counter. Therefore, when measuring the FLR and other parameters with the CAN protocol applied, it is difficult to ensure reproducibility because the measured values vary depending on the type of error that occurs and the timing. To solve this problem, we have developed a system that can measure the BER using only the physical layer without applying a communication protocol. Fig. 3.38 shows the configuration of the BER measurement system. Although ITU Recommendation O.150 recommends measuring the BER using a pseudo-random pattern, this study used the standard pattern (1010...) for simplicity. A microcontroller (RX62T, Renesas) was used to measure the BER and generate the test pattern, and a PWM module was used to generate the test pattern and output it to the Tx port. We also sampled the Rx port signal at any bit timing and compared the logic value with the original signal sent to detect bit errors. In this study, a square wave of 62.5 kHz, which corresponded to a baud rate of 125 kbps, was output by the PWM module, and the BER for 10 s was measured. The sample point was set at 70% of the bit width. In addition, the measured BER was evaluated using the confidence level (CL). Using the bit rate and measurement time (T), the CL satisfies the relationship in Equation 3.4.

$$T = \frac{-\ln(1 - CL)}{bitrate * BER} \tag{3.4}$$

To understand the trend of the BER depending on the operating conditions of the buck converter, we measured the BER when the load current and switching frequency were changed. The load current was measured by adjusting the pseudo-resistance value of the electronic load. The switching frequency was measured by changing the frequency of the square wave with the function generator that generated the gate drive signal. We also verified how the bit error changes depending on the distance between the power cable and communication line. In this verification, the DC input voltage of the buck converter was assumed to be constant at 100 V.

TABLE 3.7: BER dependency of the load current

Load current [A]	2.0	2.5	3.0	3.5	4.0	4.5	5.0
Bit error rate	16.3%	16.3%	18.4%	19.4%	21.5%	22.4%	23.5%

Table 3.7 shows the transition of the BER against the load current of the buck converter. The switching frequency of the buck converter was set to 100 kHz, and the switching duty ratio was set to 0.5. The measurement results indicated that the BER tended to increase as the load current increased. This was because the switching speed of the MOSFET in the buck converter increased as the load current increased, and the amplitude of the noise voltage induced in the communication line increased. The switching transient was not only caused by the load current, but also by the gate resistance of the MOSFET and the characteristics of the device.

TABLE 3.8: BER dependency of the switching frequency

Switching frequency [kHz]	50	60	70	80	90	100
Bit error rate	19.7%	22.9%	16.0%	19.1%	16.0%	18.6%

Table 3.8 shows the transition of the BER against the switching frequency of the buck converter. The operating conditions of the buck converter were a load current of 3.0 A and a constant switching duty ratio of 0.5. The BER changed irregularly as the switching frequency increased. The error rate was particularly large under a switching frequency of 60 kHz. This was considered to be because the frequency was close to the baud rate of the CAN communication signal (125 kbps, 62.5 kHz), and thus repetitive errors were more likely to occur.

TABLE 3.9: BER dependency of the cable distance

Cable distance [cm]	5.0	6.0	7.0	8.0	9.0	10
Bit error rate	20.8%	18.3%	15.7%	13.1%	11.0%	8.3%

Table 3.9 shows the transition of the BER against the distance between the power cable and communication line. The operating conditions of the buck converter were assumed to be a switching frequency of 50 kHz and a constant load current of 3.0 A. As the distance between the power cable and communication line increased, the electrostatic and magnetic couplings between the cables decreased. Therefore, the BER tended to decrease as the distance between the cables increased.

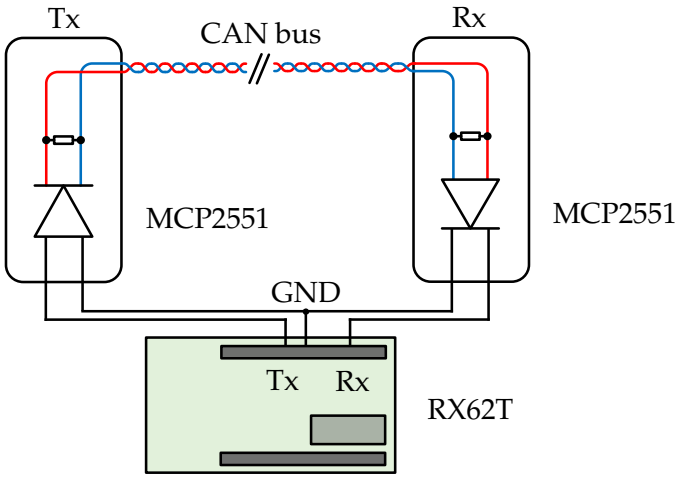

FIGURE 3.38: Configuration of the bit error rate tester

The CL of the measured BER values was calculated, and they were all confirmed to be above 0.999, which was sufficiently accurate. These verification results confirmed that the electromagnetic disturbance that occurs in CAN communication depends on the operating conditions of the buck converter and setup of the circuit.

3.8.2 Measurement of Application Level Error

The CAN communication process occurs by transmitting data frames at a constant interval. When the EMI noise of a buck converter produces critical error signals in a CAN data frame, the frame fails to transmit its data, which is known as frame loss.

Frame losses occur when a noise voltage is induced in a CAN communication line and error pulses appear in the signal output. Hence, CAN errors were observed using a serial bus analysis under the operation of a buck converter. The serial bus analysis was performed by varying the input voltage of buck converter V_{in} in the range of 0–200 V using a serial bus analyzer (MDO3054, Tektronix, Inc.). The transmitting CAN node continuously transmitted data frames to the receiving node at 125 kbps. The frame interval was set at 50 ms and measurement was performed for 2.0 s. The measured errors were classified as CRC, data, end-of-frame (EOF), and frame errors, which were detected using the respective functions of the serial bus analyzer.

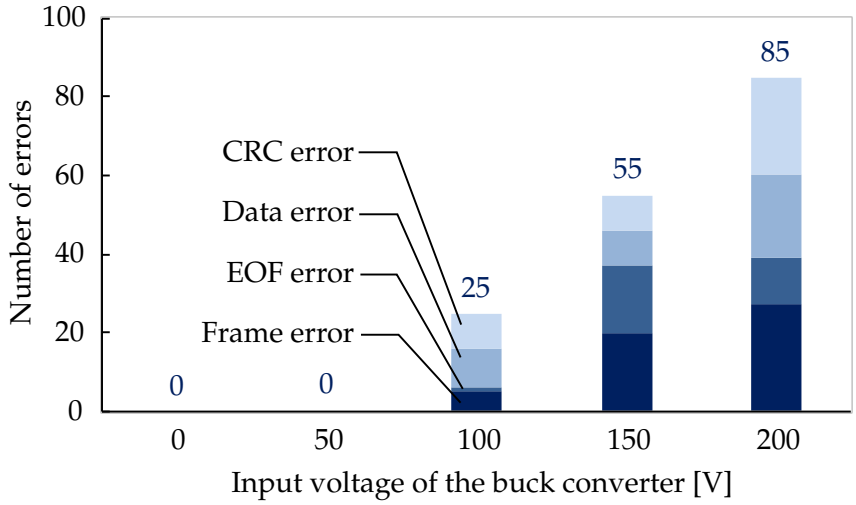

FIGURE 3.39: Measurement result of the serial bus analysis

Fig. 3.39 shows the results of serial bus analysis in the V_{in} range of 0–200 V. The results indicated that the overall number of errors gradually increased as V_{in} and the time width of the error signal increased. The measurement results indicated that the number of CAN errors was proportional to the total time width of the error signals during one switching period of the buck converter.

Many papers have reported that the noise level expressed by a frequency component is reduced by applying spread-spectrum modulation to a switching converter. If the switching frequency of the power converter is kept constant, the EMI noise caused by the power converter tends to occur at some specific frequency with a relatively high noise peak. In contrast, when spread-spectrum modulation is applied, the EMI noise is distributed to a wide frequency range, and the noise peak at a specific frequency is reduced.

However, it is unclear whether the spread-spectrum modulation realizes effective EMI mitigation in CAN communication because the voltage or current amplitude of switching noise is not reduced and the timing of switching noise is diffused. In other words, the CAN frame error caused by switching noise may not be reduced even if spread-spectrum modulation is applied to a switching converter because the average number of switching noises per switching period is still the same as that in the constant switching frequency operation. Hence, spread-spectrum modulation is seemingly not effective for improving CAN communication performance.

To verify the effectiveness of the spread-spectrum technique for improving the

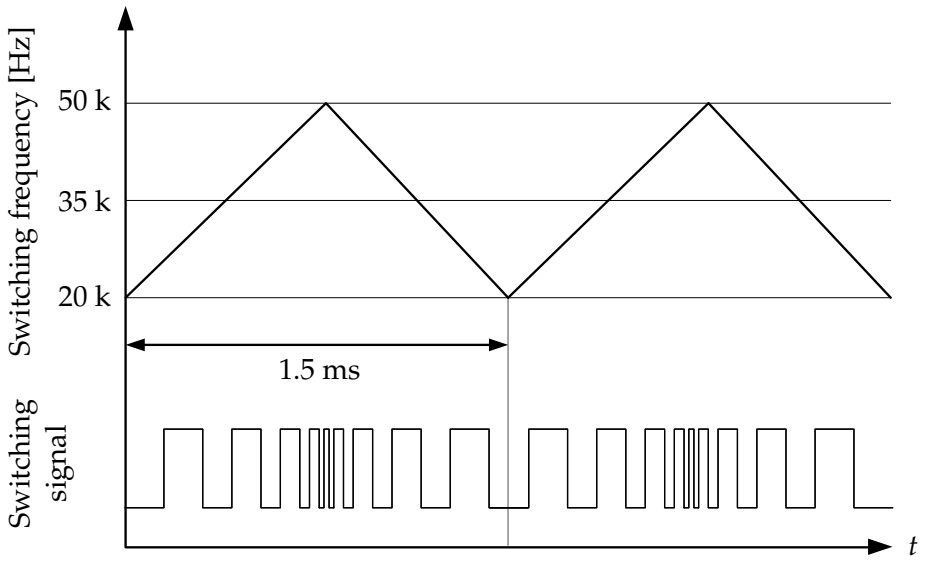

FIGURE 3.40: Modulation pattern for the switching frequency of buck converter

performance of CAN communication, we applied frequency-modulation control to a buck converter in the noise injection system. In this study, the triangular modulation method was employed to incorporate its simplicity into the system [31]. The switching frequency of the buck converter was linearly modulated in the range of 20–50 kHz in a 1.5-ms cycle (Fig. 3.40).

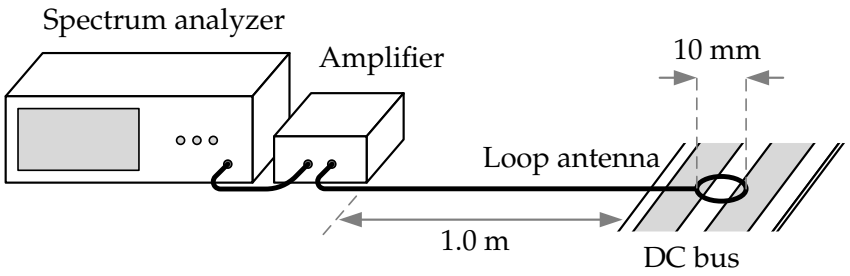

FIGURE 3.41: Measurement setup of the near magnetic field

The measurement setup is shown in Fig. 3.41. The vertical near-magnetic field at the center of the DC bus line was measured using a spectrum analyzer with a 10-mm loop antenna probe. The measurement frequency range was 10–100 MHz to observe the spectral characteristic of the parasitic-oscillation current in the DC bus. Fig. 3.42 shows the measurement result of the near-magnetic field of the DC bus line. The result indicated that frequency-modulation control reduced the EMI noise of a buck converter in the frequency domain compared with constant frequency operation at 35 kHz, which was the center frequency of spread-spectrum modulation.

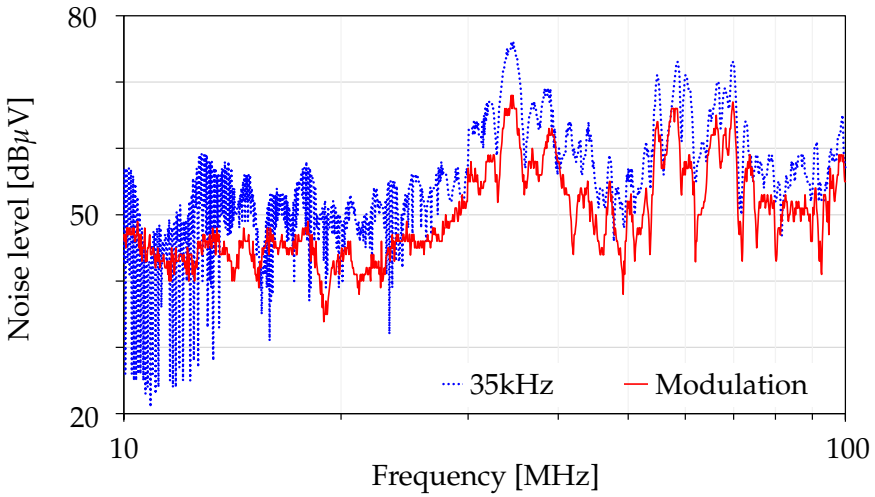

FIGURE 3.42: Measurement result of vertical near-magnetic field at the center of the DC bus

Serial bus analysis was performed while applying frequency modulation control to the buck converter under the same operating condition as the measurement of near-magnetic field. Several switching frequencies were used in the range of 20–35 kHz at constant frequency switching conditions for comparison with the frequency modulating condition.

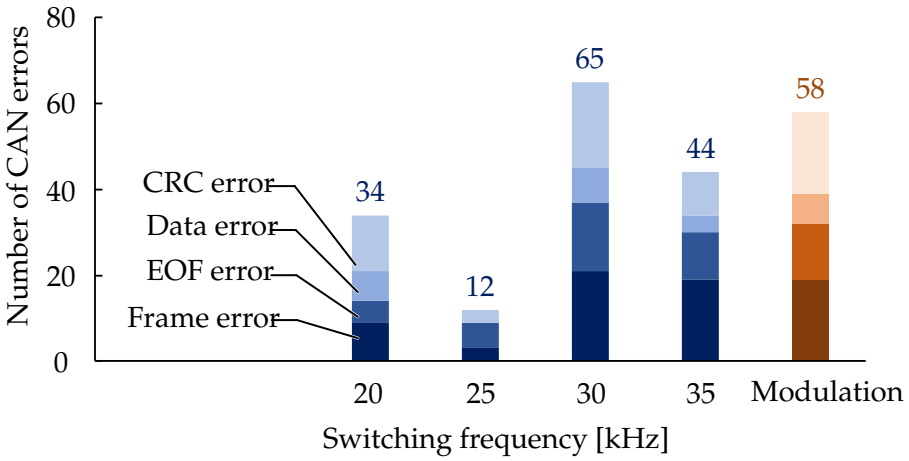

FIGURE 3.43: Measurement result of the serial bus analysis with the switching frequency modulation

As shown in Fig. 3.43, for the constant switching frequency, the number of CAN errors varied depending on the switching frequency. The probability of the switching timing and CAN sample timing coinciding was considered to depend on the switching frequency. In contrast, CAN errors were not sufficiently

mitigated compared with those under constant switching frequency conditions even when frequency modulation was applied to the buck converter. The frequency modulation method was expected to diffuse the switching timing of the converter, but the probability of both timings coinciding could not be consistently reduced; it occasionally increased or fortunately decreased depending on the frequency modulating conditions. The results indicated that the spread-spectrum modulation technique is not a promising method of improving the robustness of the CAN communication line against the EMI noise of a power converter.

3.9 Summary

This chapter describes the noise injection system as an experimental platform and time-domain analysis to study the CAN error mechanism in detail. The noise injection system consisted of a buck converter and a CAN bus with two nodes. The system achieved experimentation with high repeatability. The following were the key findings of the experimental study with the noise injection system:

- the buck converter induces a CM conducted noise into the communication cable at a switching timing
- the CM conducted noise is converted to a DM noise owing to impedance imbalance of the differential communication line
- the terminals of the transceiver have an unbalanced impedance
- the DM conducted noise flowing into the transceiver cause logical flips
- if the logical flip coincides with a CAN sample, a bit error would occur

Furthermore, the noise simulation verified the above items through waveform comparisons. In particular, for modeling methodologies, OFF-state impedance of MOSFET and stray impedance of electrolytic capacitor affect the conducted noise waveform. Accordingly, simplified models are proposed and they realize accurate estimation of the conducted noise. Additionally, the CAN error evaluation enables us to quantify the EM disturbance on communication. The BER measurement reflects the events on the physical layer directly. Moreover, serial bus analysis is a more application-level evaluation. Owing to these characteristics, the experimental results can aid in determining the parameters that influence the number of error events.

Chapter 4

Time Series Control of Active Gate Driver

4.1 Introduction

This chapter describes experimental studies on the time series control of the converter switching speed to suppress the EM disturbance on CAN. As mentioned earlier, switching waveforms of power semiconductor devices affect the noise emission level. Accordingly, an AGD is a strong candidate technique for controlling the noise emission level by changing the switching waveform. The AGD can control voltage and current slopes of power semiconductor devices by adjusting the profile of the gate signal to suppress the EMI since the switching waveform of a power device impacts the switching noise waveform. To employ the capability of gate slew rate control, we studied two types of AGDs:

- a variable switching speed gate driver
- a slew-rate controlled gate driver

Both drivers were applied to the noise injection system, and the effects of switching speed on the EM disturbance were experimentally investigated by measuring the FLR or BER of the CAN.

First, the effects of switching speed on the EM disturbance are discussed. Using Si and SiC MOSFETs, the converter switching waveform was changed and the CAN error condition was clarified. Next, for the variable switching speed gate driver, a multi-channel gate driver changed the converter switching speed. By switching high-speed and low-speed modes, the driver enabled effective EMI

reduction. In contrast, the slew-rate controlled gate driver adjusted the gate current to change the switching speed. Through the experimental verification, the error rate distribution indicated that dynamic control of the gate driver makes the CAN communication more robust.

4.2 Effects of Switching Waveform on CAN Error

TABLE 4.1: MOSFET specification

Devise number	Device type	V_{DS}(max)	I_D(max)	$R_{DS(on)}$
FCH072N60	Si MOSFET	600 V	52 A	66 mΩ
C2M0080120D	SiC MOSFET	1200 V	36 A	80 mΩ

As a fundamental study, the experimental study of the effect of switching waveform on CAN errors is summarized here. Most recent studies have reported that a faster switching of power semiconductor devices increases the conducted noise [91]–[93]. However, only a few studies have experimentally investigated the effects of EM disturbance on serial communication. In this context, this section first presents a noise waveform comparison between Si and SiC MOSFET to investigate the EM impacts on CAN communication.

Si and SiC MOSFET-based buck converters were applied to the noise injection system to generate different EMI noise waveforms for experimental comparison, and several measured voltage and current waveforms were compared. The buck converters had an identical circuit topology and physical structure for the waveform comparison. No snubber circuits were implemented for both MOSFETs.

The specifications of the MOSFETS were significantly different and were suitable for comparing the switching behavior (Table 4.1). In the comparison, the operating conditions of the buck converters were set as follows: the switching frequency was 30 kHz, the switching duty ratio was 0.5, and the input voltage was set to 100 V. The comparing waveforms were the drain–source voltage of MOSFET (v_{DS}), the CM switching noise current (i_{CM}) in the CAN communication cables, and Rx output voltage (v_{Rx}).

Figs. 4.1(a)–(c) show measurement waveforms when the Si MOSFET was turned off, and Figs. 4.2(a)–(c) show those of the SiC MOSFET. As v_{DS} in Figs. 4.1(a) and Fig. 4.2(a) show, the switching speed changed considerably: 1.03 V/ns

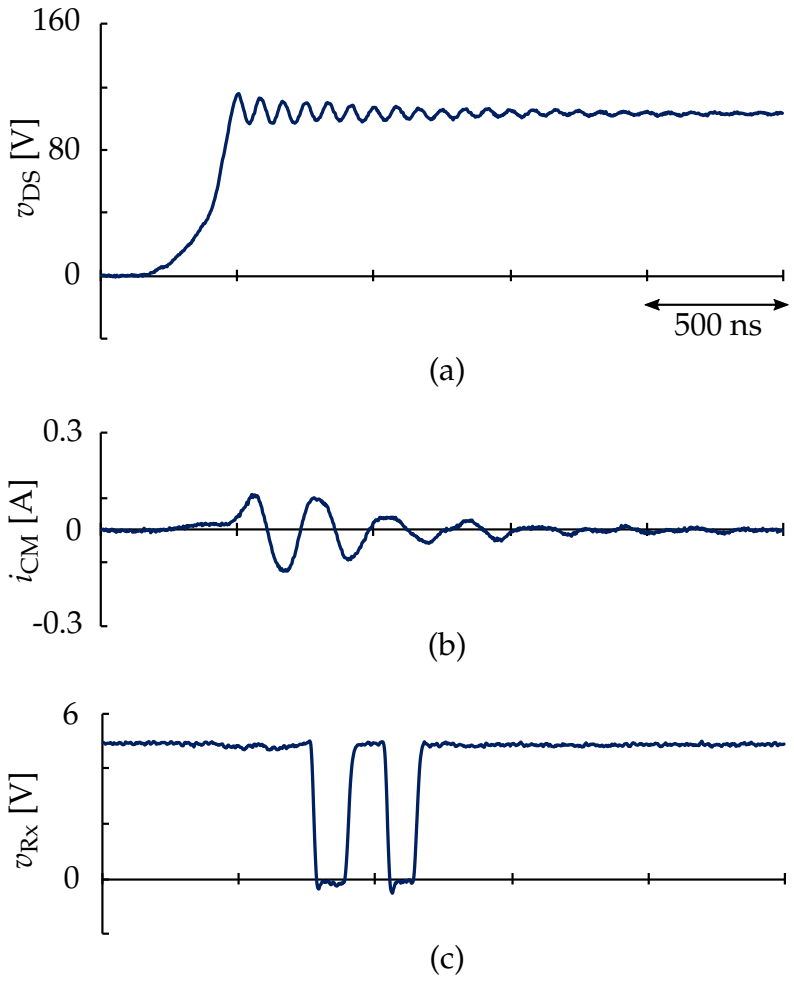

FIGURE 4.1: Measured waveforms when the Si MOSFET is turned off. (a) Drain source voltage of MOSFET v_{DS}. (b) CM noise current in the CAN bus i_{CM}. (c) Rx output voltage v_{Rx}.

for the Si MOSFET and 2.38 V/ns for the SiC MOSFET on average. In particular, the Si MOSFET gradually increased the dv/dt during the switching transient. The amplitude of CM noise current also changed (Figs. 4.1(b) and Fig. 4.2(b)). Subsequently, error pulses were caused in v_{Rx} (Figs. 4.1(c) and Fig. 4.2(c)), and the number of error pulses was largely different.

From the measured waveforms, we considered that there is a strong correlation between converter switching behavior and EMI failure on CAN communications. Accordingly, CAN bus analysis was performed to verify that the switching behavior influences CAN performance. In the CAN bus analysis, the CAN Tx sent data frames at 125 kbps and all data frames were monitored using the CAN bus analyzer. For the buck converter with embedded Si and SiC MOSFETs, the

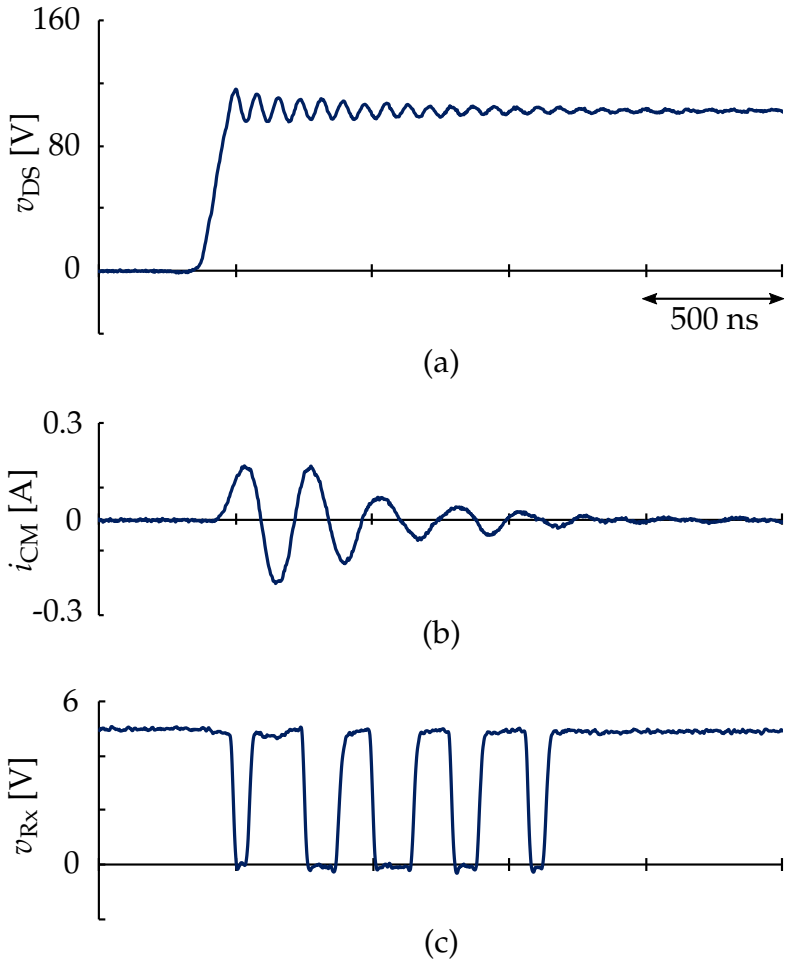

FIGURE 4.2: Measured waveforms when the Si MOSFET is turned off. (a) Drain source voltage of MOSFET v_{DS}. (b) CM noise current in the CAN bus i_{CM}. (c) Rx output voltage v_{Rx}.

operating condition was identical to the waveform measurements, as mentioned earlier. As shown in Table 4.2, under the operation of the SiC MOSFET buck converter, the frame error rate (FER) was larger than that of the Si MOSFET buck converter. This corresponded to the measured tolerable noise level for the CAN transceiver. The CM noise peak current ($i_{CM-peak}$) under the operation of both converters is depicted in Fig. 4.3. The result of CAN bus analysis and Fig. 4.3 show that the tolerable noise level indicated when the CAN operated without errors, and the threshold noise level was verified.

TABLE 4.2: Measurement result of frame loss rate test

Input voltage V_{in} [V]	0	20	40	60	80	100
Si MOSFET	0%	0%	0%	0%	0%	3.3%
SiC MOSFET	0%	0%	0%	0.6%	2.3%	6.2%

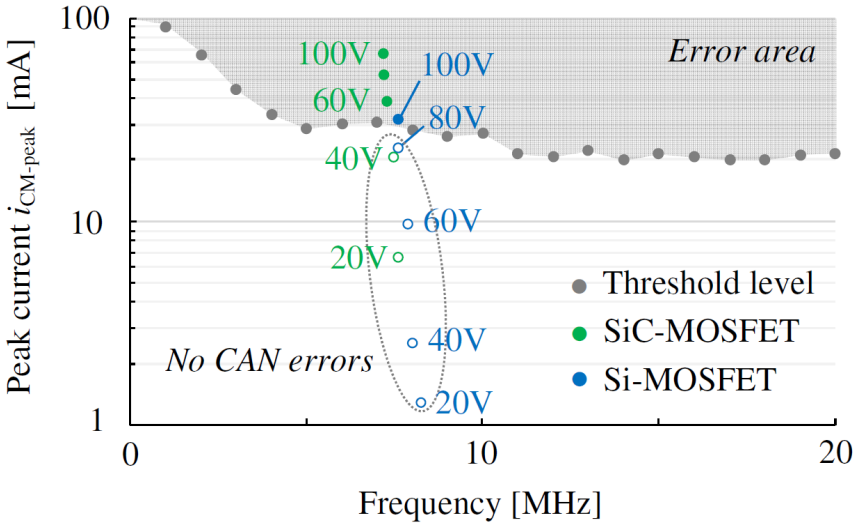

FIGURE 4.3: Experimental result of CM noise injection into the transceiver

4.3 Variable Switching Speed Gate Driver

The switching dv/dt of the MOSFET should be slowed down to reduce the noise voltage induced in the CAN communication line. A straightforward method to achieve the slowing down is to increase the gate resistance of MOSFET and reduce the gate current slew rate (di/dt). However, this method increases the switching loss of the MOSFET and reduces the power conversion efficiency.

Fig. 4.4 shows the configuration of a variable switching speed driver. Three parallel gate drive circuits were connected to the MOSFET of the buck converter, and the gate resistance was switched by monitoring the CAN signal state using the monostable multivibrator. The gate resistance was increased only when the CAN signal was being transmitted to minimize the switching loss. The gate resistance value during the low dv/dt operation was selected based on the experimental verification of the noise injection system to prevent CAN communication errors.

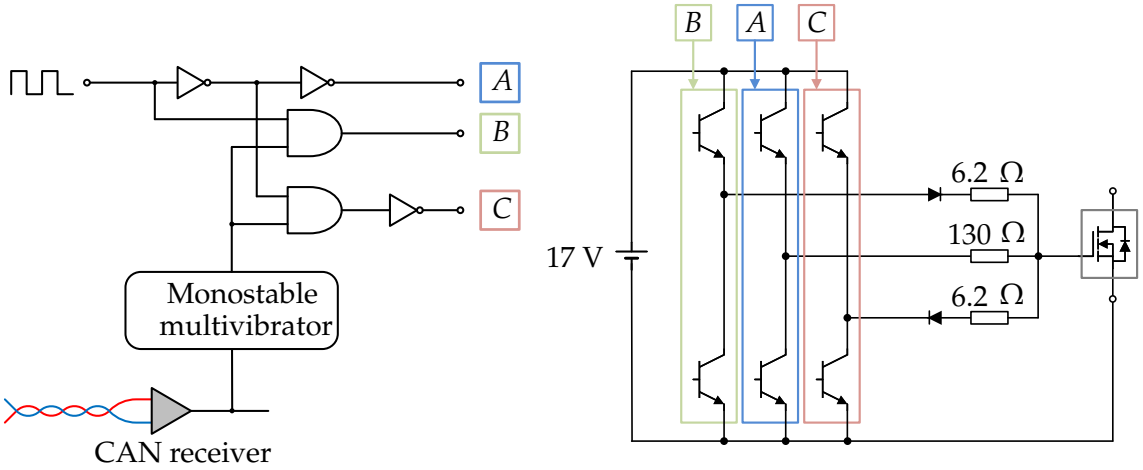

FIGURE 4.4: Configuration of the variable switching speed driver

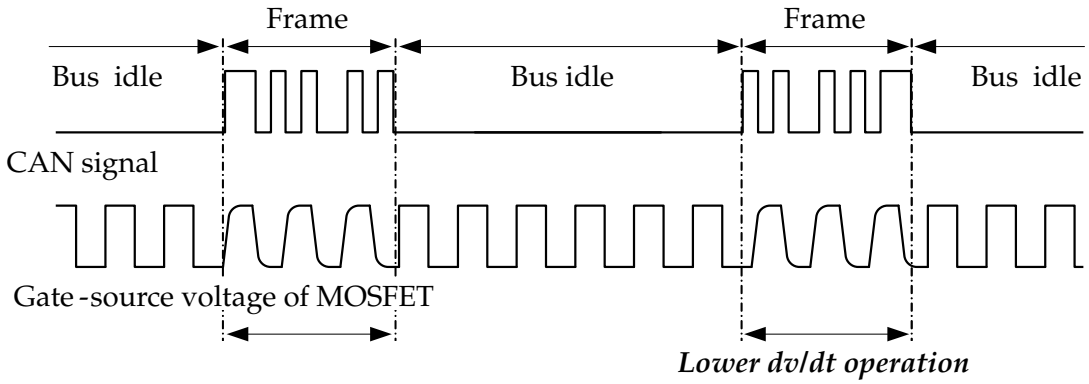

FIGURE 4.5: Schematic waveform of CAN signal and gate-source voltage of MOSFET with the variable switching speed driver

Fig. 4.5 shows a schematic waveform of the CAN signal and gate–source voltage of the MOSFET with the variable switching speed driver. The time ratio between the frame period and the bus idle period varied depending on the CAN bus traffic, but in this study, the frame transmission interval was set to 50 ms and the frame time length was approximately 1.1 ms.

Fig. 4.6 shows operating waveforms of the proposed system, switching signal, gate–source voltage of the MOSFET, and CAN communication signal. The measurement condition was as follows: a switching frequency of 20 kHz, and a duty ratio of 0.5. As shown in Fig. 4.6, the gate resistance was switched from 6.2 to 130 Ω at the start of frame (SOF) bit transmission in the CAN communication, and a low dv/dt operation was performed. In addition, the amplitude of the noise voltage induced in the CAN communication line was sufficiently suppressed during the low dv/dt operation.

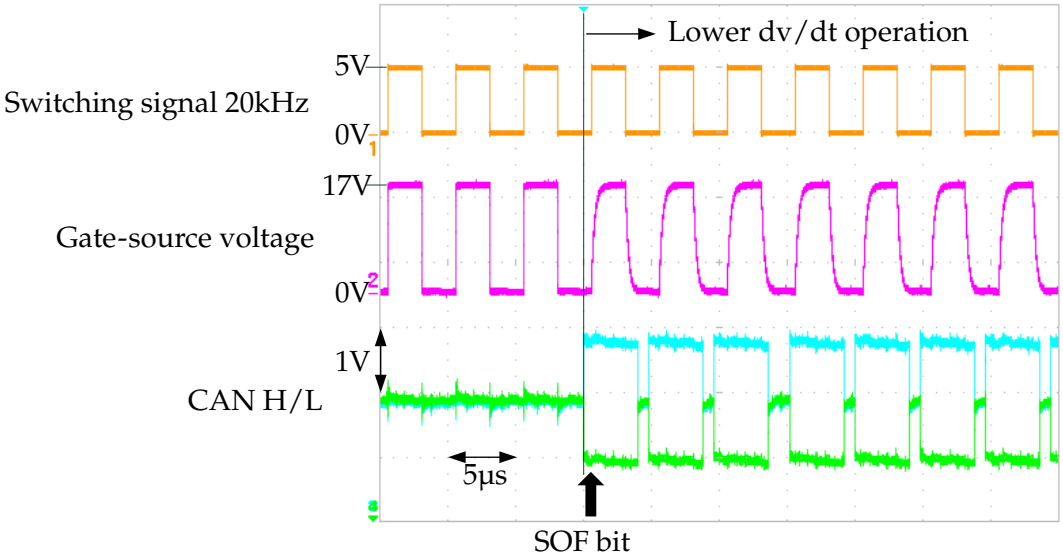

FIGURE 4.6: Measured waveforms in the proposed system

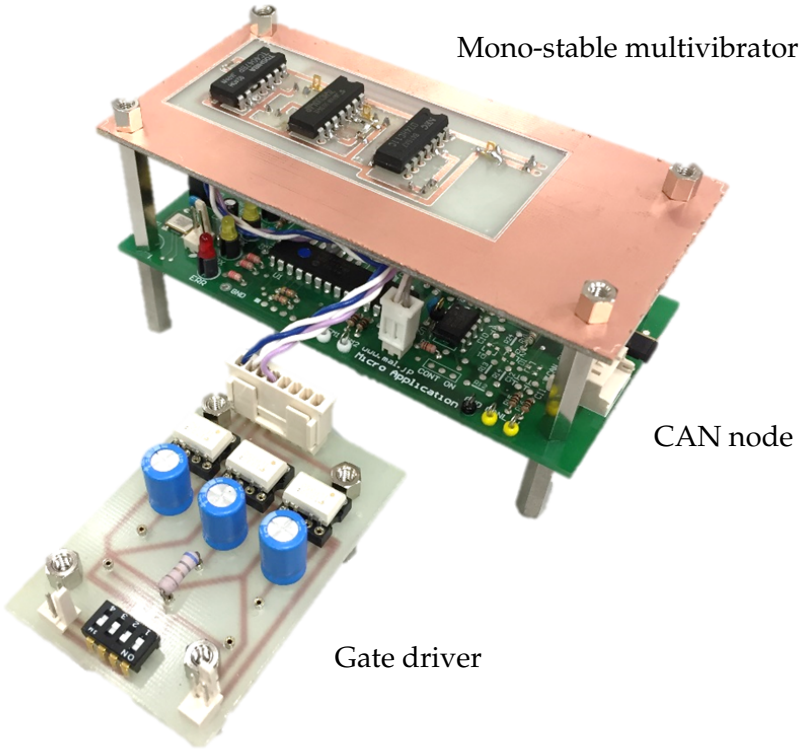

FIGURE 4.7: Experimental setup of the variable switching speed gate driver

To verify the performance of the communication error reduction of the variable switching speed driver, we measured the CAN FLR using a CAN bus analyzer (Tektronix MDO3054). The input voltage of the buck converter was set to 100 V, the switching frequency was 20 kHz, and the switching duty ratio was 0.5. When the gate resistance was 6.2 Ω, the CAN FLR was 3%. In contrast, the variable switching speed driver suppressed the CAN FLR to 0%, which indicated that the method is effective in suppressing CAN communication errors.

In addition, to evaluate the performance of the variable switching speed driver in maintaining power conversion efficiency, we compared the method with that for a constant gate resistance value of 130 Ω. The difference in power conversion efficiency was measured under feeding the output current of the buck converter at a constant 3.0 A (output power 90 W). When the gate resistance value was changed from 6.2 Ω (constant) to 130 Ω (constant), the conversion efficiency decreased by 0.8%, whereas when the variable switching speed driver was applied, the decrease in power conversion efficiency was only 0.1%, confirming that the method can mitigate the deterioration of power conversion efficiency while suppressing CAN communication errors.

4.3.1 Configuration of the Noise Injection System with Discrete Active Gate Driver

TABLE 4.3: Specification of the noise injection system with the active gate driving function

Symbol	Description
S_1, S_2	CAS120M12BM2, CREE, 1200 V, 120 A, 0.13 mΩ
R_T	Termination resistor, 120 Ω
C_{DC}	2200 μF, 450 V (electrolytic capacitor)
L	180 μH, 10 A (iron core inductor)
R_{Load}	20 Ω, 700 W (metal clad resistor)
C_S	0.47 μF (film capacitor)

Figs. 4.8 and 4.9 and Table 4.3 depict a noise injection system composed of a buck converter and a CAN communication system with the AGD. The buck converter primarily consisted of a 2-in-1 type SiC-MOSFET module and snubber capacitor. The CAN communication system had two nodes connected with an unshielded pair cable each other and the bus topology satisfied ISO11898-2 for high-speed CAN communication. The DC bus and communication cables were

parallel and adjacent to each other. This cable configuration resulted in a relatively strong electromagnetic coupling among the cables.

Figs. 4.10 (a)–(d) and 4.11 (a)–(d) show the measured waveforms of the noise injection system when the converter MOSFET was turned off and on under the following conditions: a DC bus voltage of 100 V, converter switching frequency of 30 kHz, and a constant duty ratio of 0.5. The turn-off waveform also had a similar shape to the turn-on waveform.

Hence, this study only focused on the turn-on switching transient for simplicity. Under the CM current in the DC bus cables, shown in Fig. 4.11 (b), a damped oscillation waveform appeared. This oscillation was due to a rapid CM voltage variation of the converter, and the ringing frequency primarily depended on the wiring inductance and stray capacitance of the CM noise path. Subsequently, a CM noise current was also induced in the communication cables through the effect of electromagnetic coupling among the DC bus and communication cables (Fig. 4.11 (c)). Since the CAN system employed a differential signaling method, it had low susceptibility to CM noise.

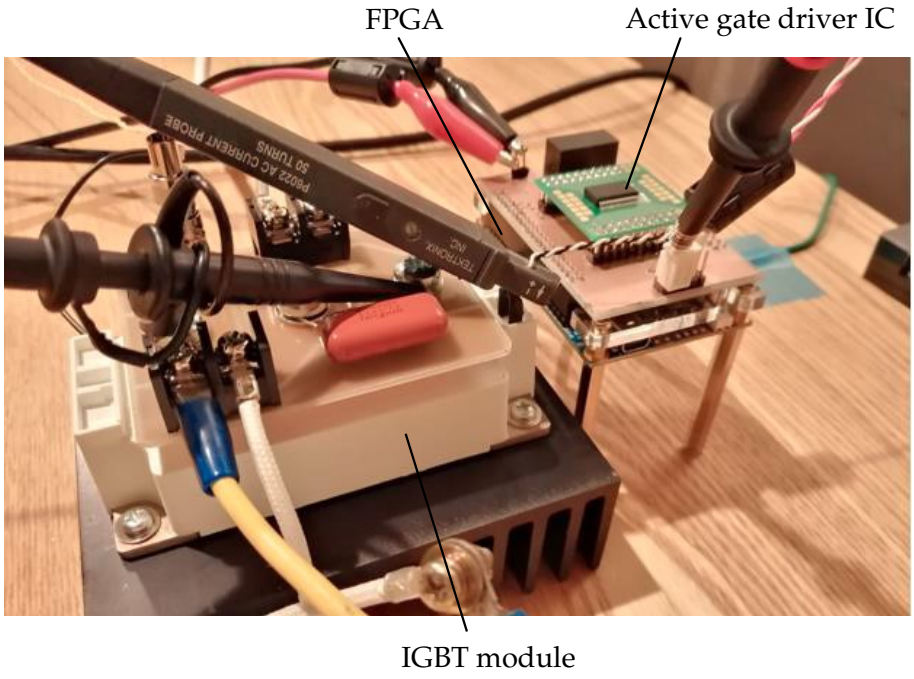

FIGURE 4.8: Experimental setup of the noise injection system

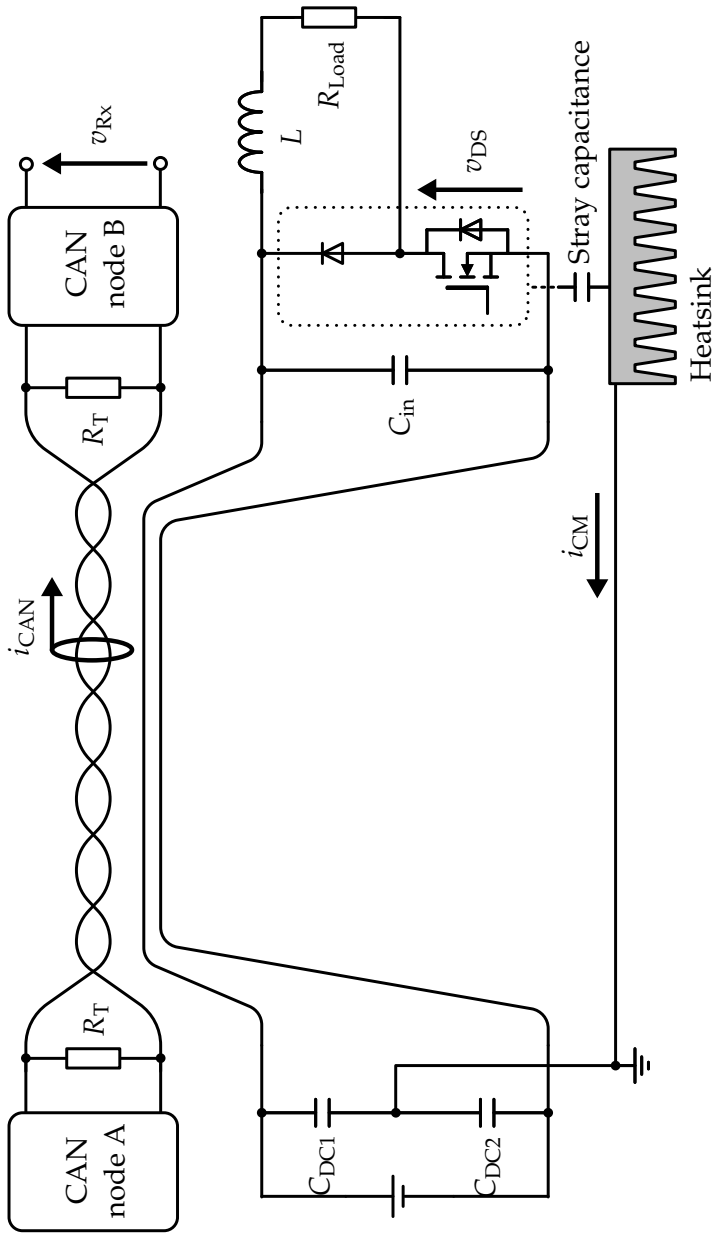

FIGURE 4.9: Configuration of the noise injection system

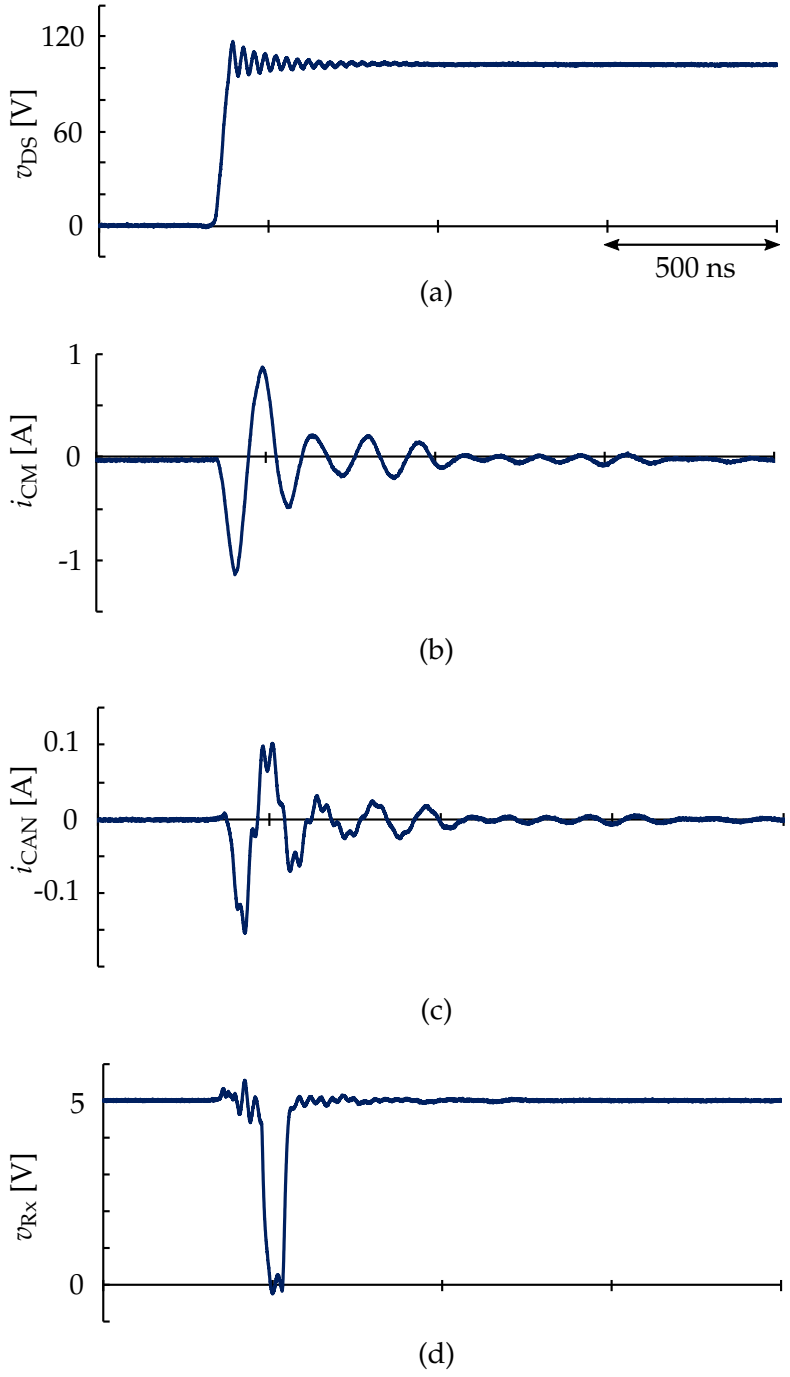

FIGURE 4.10: Measured waveforms when the MOSFET is turned off. (a) Drain-source voltage of MOSFET. (b) CM nosie current in the DC bus. (c) CM noise current in the CAN cable. (d) Receiver output voltage.

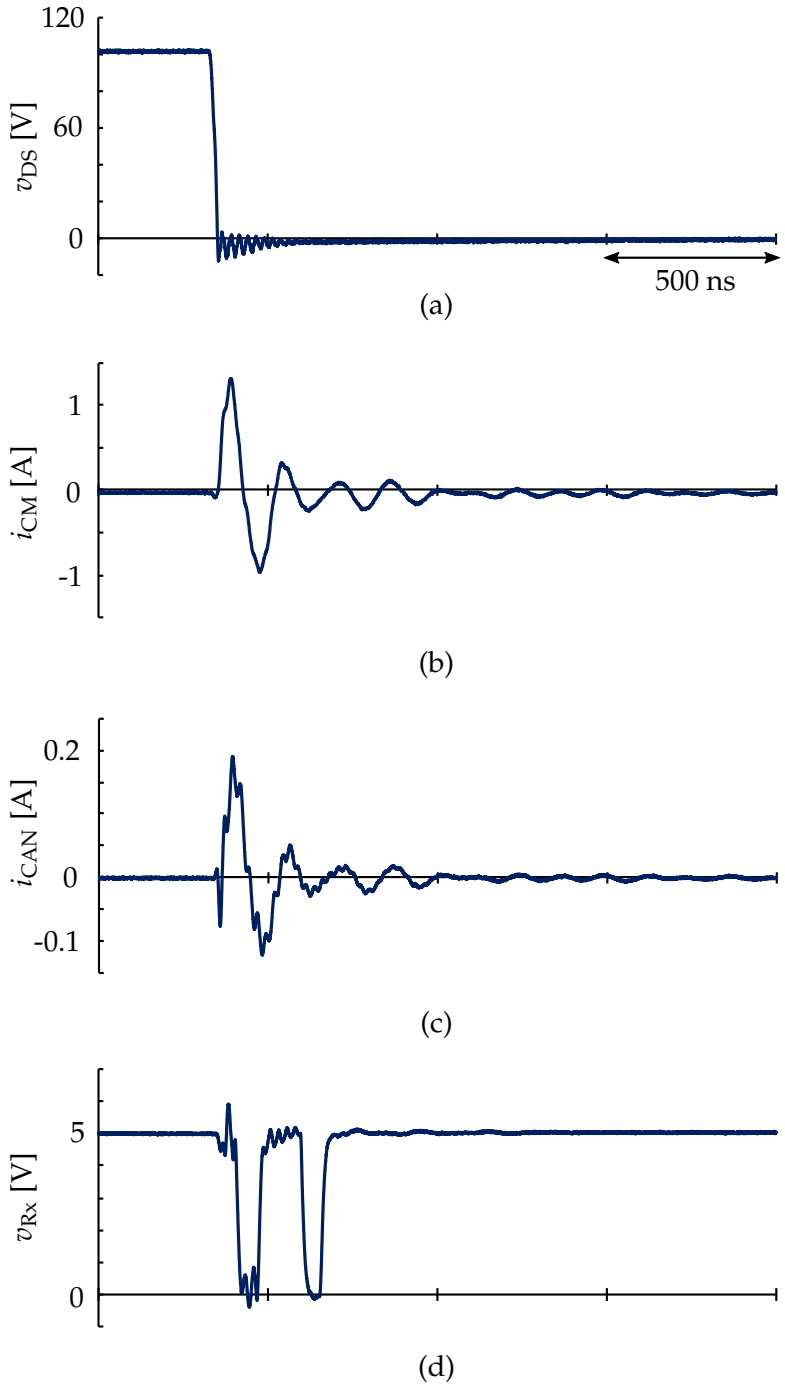

FIGURE 4.11: Measured waveforms when the MOSFET is turned on. (a) Drain-source voltage of MOSFET. (b) CM nosie current in the DC bus. (c) CM noise current in the CAN cable. (d) Receiver output voltage.

In practice, a CM noise is non-ideally converted to a DM noise in the CAN system, which is called mode conversion [88], [94]. Mode conversion is primarily due to the impedance imbalance of the differential communication lines (e.g., twisted pair cable, receiver IC, etc.). The CAN receiver converted differential signals in the CAN cable to a transistor–transistor logic (TTL) signal (0/5 V). Additionally, the communication signal was set to a recessive state, and the receiver output was to be maintained at 5 V during the measurement. However, in the receiver output, there were logical flips caused by the mode conversion, which resulted in communication failure.

4.3.2 Active Gate Driver Impacts on CAN Error Rate

The AGD controls voltage and current slopes through a power device by modulating the gate signal, which enables control of the switching speed of the device. Moreover, the AGD is one of the candidates for suppressing the EMI in CAN communication since the converter switching speed affects the noise waveform. However, many authors focus on the topology or the performance [11], [95], [96], and only a few address its practical applications [97]. Thus, this thesis presents a practical use of AGD with a focus on EMI suppression.

In this study, an AGD was implemented in the converter SiC MOSFET using a commercialized gate driver IC (1EDS20I12SV, Infineon) [98]. The design procedure of the peripheral circuit was based on the product datasheet. Figs. 4.12 (a)–(c) show the experimental turn-on waveforms of the AGD-applied MOSFET under the converter operation. The gate driver enabled the MOSFET to operate with 11 gate current levels and it changed the switching speed. Next, the CM noise current in the DC bus and the CAN receiver output were measured with the changing gate current level. As shown in Fig. 4.12 (a)–(c), the CM noise current amplitude varied with the gate current level, whose variation caused logical flips of the receiver output. These results indicted a strong correlation between the noise waveforms and the gate current control of AGD.

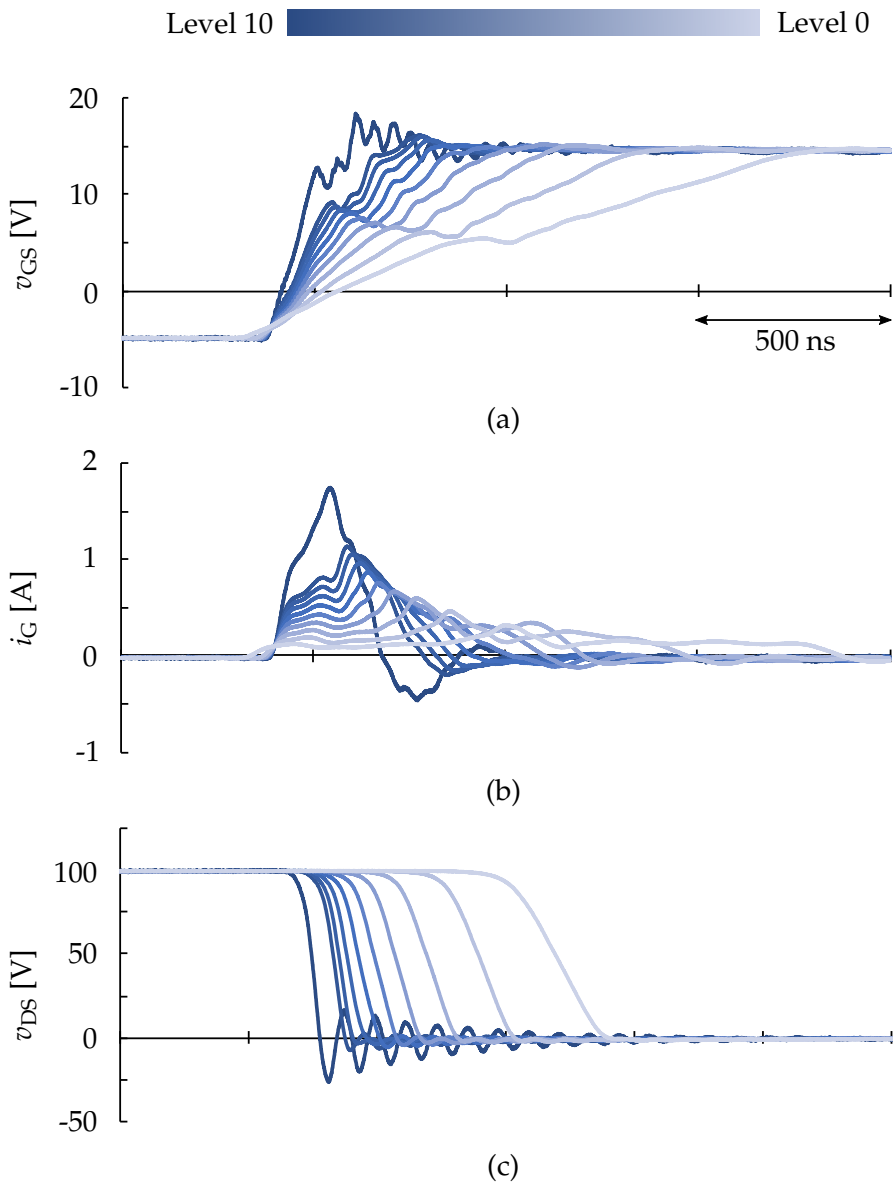

FIGURE 4.12: Measured turn-on waveforms with changing gate current level. (a) Gate-source voltage of MOSFET. (b) Gate current of MOSFET. (c) Drain-source voltage of MOSFET.

As further experimental verification, the CAN BER was measured by varying the DC bus voltage and gate current level of the AGD under the following converter operating conditions: a switching frequency of 30 kHz and constant duty ratio of 0.2. As shown in Fig. 4.13, the BER varied with the gate current level of the AGD. When the DC bus voltage was above 100 V, the BER was almost proportional to the gate current level and the switching speed of the MOSFET. In contrast, when the DC bus voltage was less than 100 V, the BER varied irregularly. This phenomenon resulted from the characteristic of the MOSFET output

capacitance.

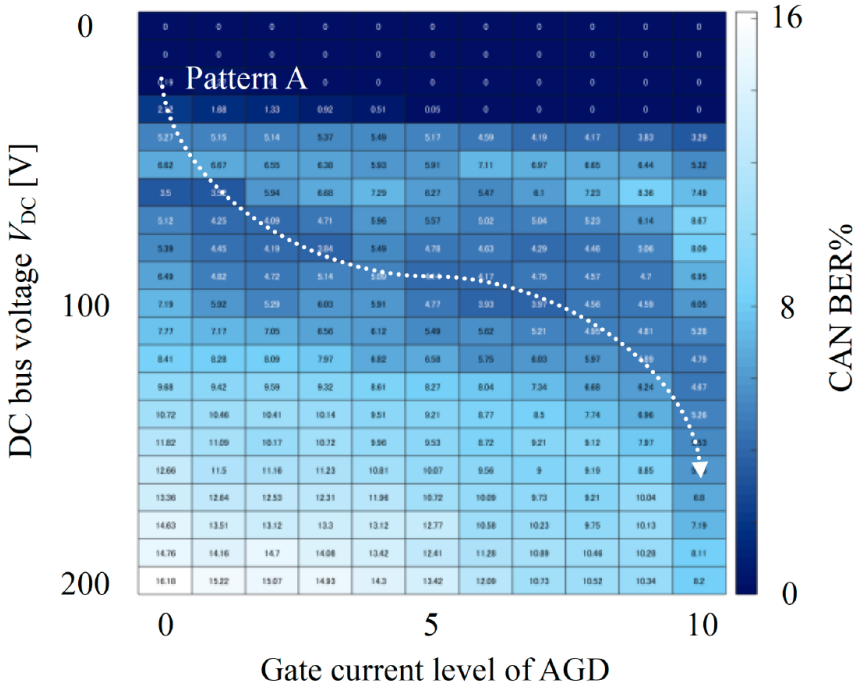

FIGURE 4.13: BER test with changing DC bus voltage and gate current level of the AGD

The output capacitance largely varied in relatively low voltage region, which impacted the noise amplitude and frequency in the DC bus and the communication cables. This will be detailed in the final paper. Based on the measurement result, the gate current level of AGD can be increased with the DC bus voltage (Fig. 4.13, Pattern A) to suppress the BER. Conventional gate drivers commonly drive a MOSFET with a constant gate resistor. Thus, such a typical driver cannot control the gate current level according to the DC bus voltage or other converter operating parameters. Hence, the AGD has the advantage of adjusting the gate current level for EMI suppression on the communication according to the converter operation.

4.4 Summary

This chapter presents experimental studies on switching waveform impacts on the EM disturbance and time series control as an EMI reduction approach. A waveform comparison between Si and SiC MOSFET shows that the dv/dt primarily impacts the CM noise waveform and CAN error rate. Derived from this phenomenon, the time series control of a variable-switching-speed gate driver can prevent communication errors. Additionally, the control method can suppress the switching loss of the device by changing the switching speed for a data transmission period and a bus idle period.

Moreover, a discrete AGD can dynamically suppress EM disturbance. A gate driver IC was applied to the noise injection system to verify the effects on the EMI. The AGD comprised a commercialized gate driver IC and it could drive a SiC MOSFET with 11 gate current levels. In the experimental verification, the gate current level of AGD corresponded to the switching speed of the MOSFET and it influenced the noise waveform in the CAN communication cables. The experimental results indicated that the CAN BER depends on the gate current level of the AGD. This correlation can be applied to an EMI suppression technique.

Chapter 5

Time-Dependent Control of a Buck Converter for EMI Reduction

This chapter describes a control method of the buck converter to reduce the EM disturbance on CAN communication. As a fundamental study, the start–stop synchronization method was used for error mitigation by avoiding a timing collision of a converter switching and a CAN sample. Subsequently, as a more practical approach, the timing-shift control was used to avoid the coincidence of a converter switching and CAN sample point at which a bit error occurs. An experimental verification indicated that the proposed method introduces a limitation to the output voltage of the buck converter. Accordingly, a compensation method to the timing-shift control suppresses the limitation. Finally, the experimental results indicated that the timing-shift control mitigates communication errors.

5.1 Start-Stop Synchronization Control

Generally, SMPSs and serial communication systems are not synchronized. Thus, a conducted noise of the communication line owing to a converter switching appears depending on the phase relation between them. In other words, a coincidence of a switching timing and a CAN sample occurs depending on the phase shift between the converter and communication signal. Focusing on the phase relation, signal synchronization between the buck converter and CAN system can prevent a timing collision. To realize the synchronization, we implemented a start–stop synchronization method to the DM noise injection system. The start–stop synchronization is a well-known technique for asynchronous communication systems [99], [100].

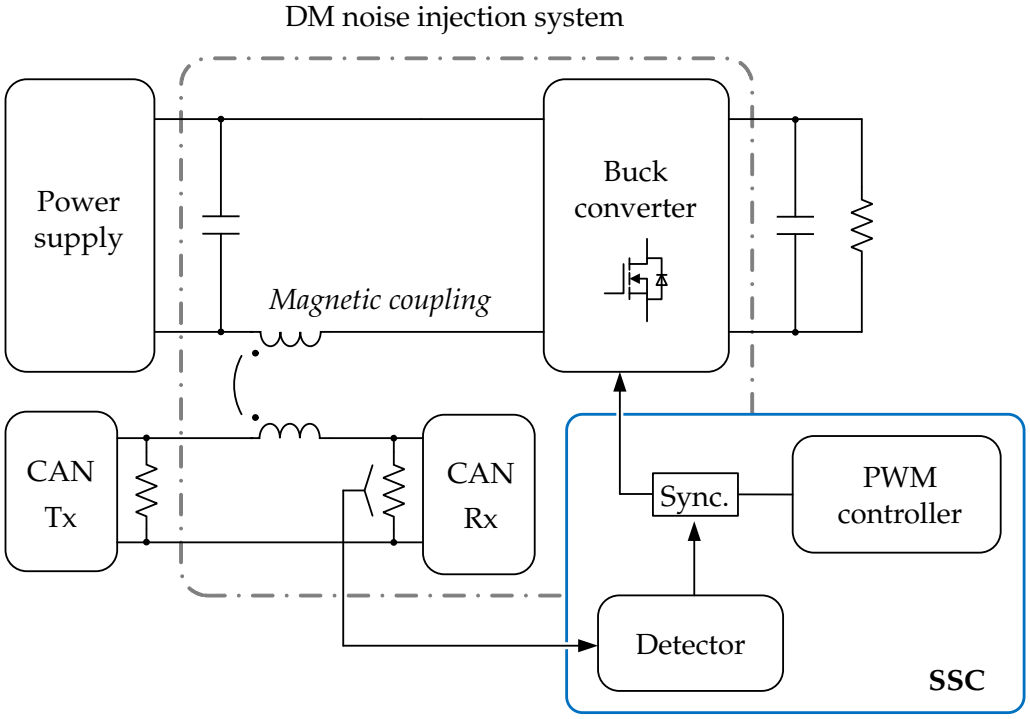

FIGURE 5.1: Configuration of the DM noise injection system with SSC controller

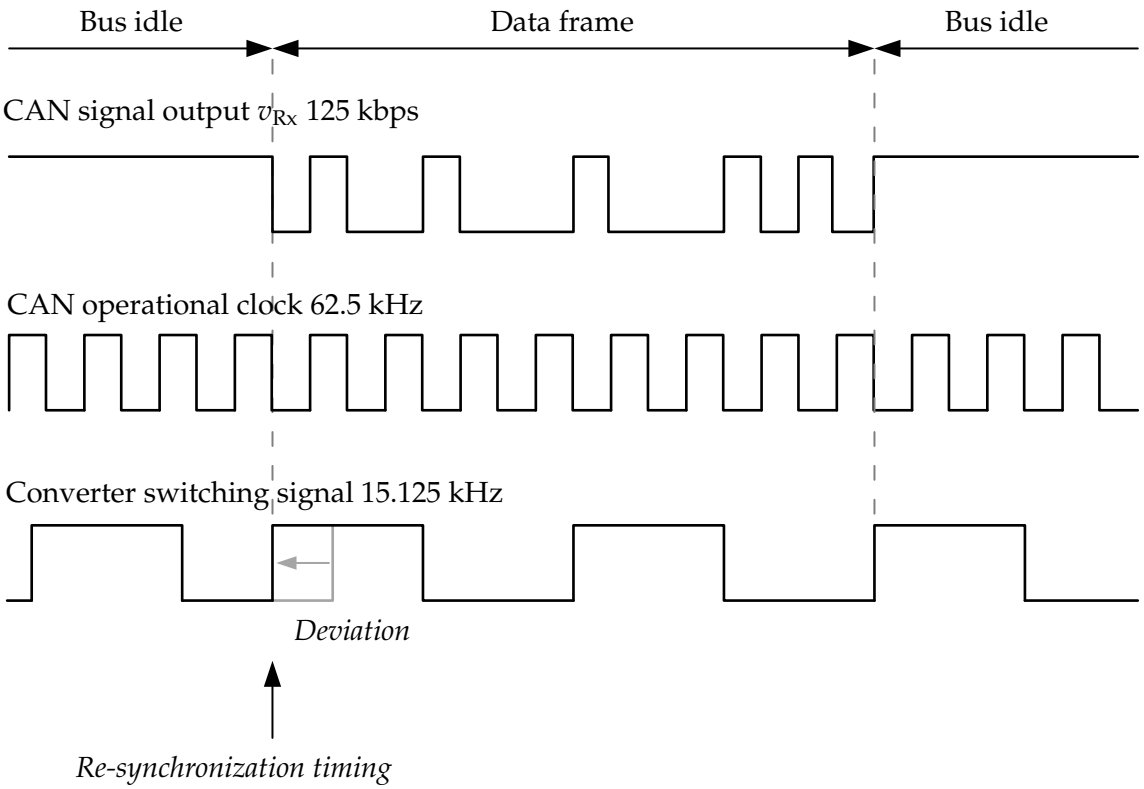

FIGURE 5.2: Timing chart of the SSC operation

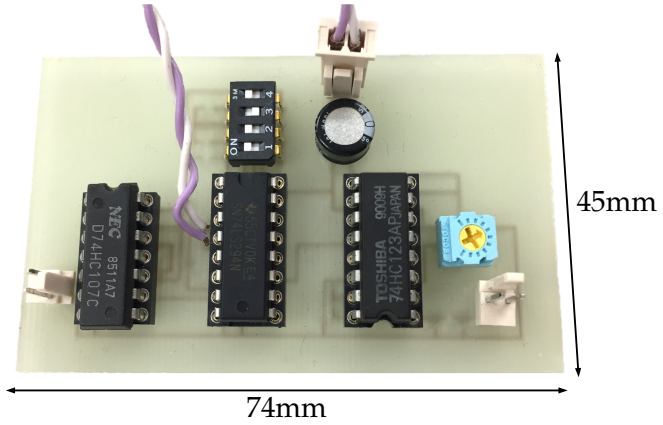

FIGURE 5.3: Prototype SSC board for the DM noise injection system

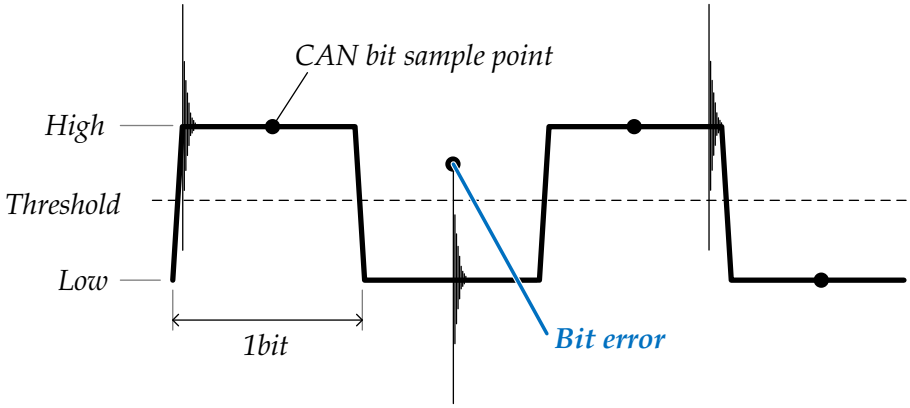

FIGURE 5.4: CAN signal without synchronizing with the buck converter

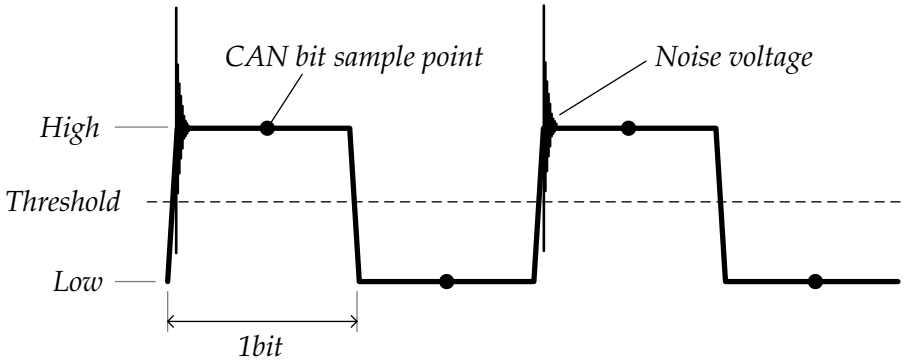

FIGURE 5.5: CAN signal under the SSC operation

Fig. 5.1 shows the configuration of the DM noise injection system with an embedded start–stop synchronization controller (SSC). Fig. 5.2 shows the timing chart describing the SSC operation scheme. When the start timing of a data frame

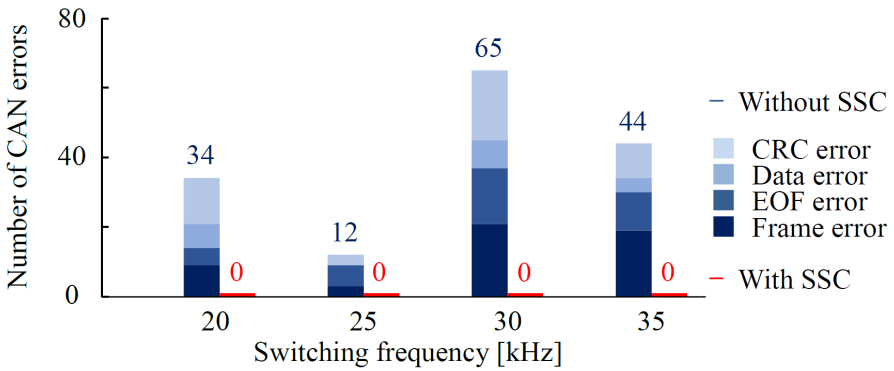

FIGURE 5.6: Measured number of errors

is detected in the communication line, a switching timing of the buck converter is re-synchronized with the operating clock of the communication signal. This maneuver ensures the synchronization between the PWM signal of the buck converter and communication signal. In this study, the switching frequency of the buck converter was set to 15.125 kHz, which was a quarter of the communication signal clock (62.5 kHz), because the switching frequency must be a common divisor of the operating frequency of the clock to synchronize.

Fig. 5.3 shows the prototype SSC board for the DM noise injection system. The controller board primarily consisted of a frequency divider and a monostable multivibrator. The frequency divider was used to generate a converter switching signal based on the CAN operational clock. The monostable multivibrator was used to detect the data frame and trigger a re-synchronization maneuver. Regarding the implementation, the board can be further downsized and integrated into the converter MCU.

Fig. 5.4 depicts a transceiver output signal with a bit error. As mentioned earlier, when a sample point coincides with a conducted noise, a bit error occurs and it results in communication failure. In contrast, Fig. 5.5 depicts the signal under the synchronized operation with the buck converter. Each conducted noise appears on bit edges away from sample points. Thus, the timing collision never occurs until the synchronization is active.

To verify that the start–stop synchronization control can effectively reduce frame errors in CAN communication, we analyzed the serial bus while applying start–stop synchronization control to the noise injection system. Fig. 5.6 shows the measured number of errors. The result indicated that CAN communications were successfully realized, and the FER was always 0%, irrespective of the DC

bus voltage V_{in}.

However, some limitations were introduced when start–stop synchronization control was applied. The switching frequency and duty ratio of the buck converter were restricted because switching cannot occur near a sample point. This restricts the flexibility of the switching timing of the power converter and affects the control performance.

5.2 Timing-Shift Control (TSC) of a Buck Converter

5.2.1 Operation Principle of TSC

As described in the previous section, the SSC achieves an effective EMI reduction, but it introduces restrictions on the converter control. This section presents the timing-shift control (TSC) as a more flexible and practical solution. Fig. 5.7 shows a timing chart of the TSC. The TSC prevents the coincidence of switching noise and a CAN sample point by slightly shifting the switching timing. Hence, it can realize EMI reduction without relying on conventional methods because noise amplitude is not considered. The gate signal of a MOSFET is typically obtained using PWM control. However, when the original switching timing occurs during a switching-prohibited period, where the switching noise can coincide with the CAN sample timing, the PWM output is slightly disarranged to prevent communication failure. Thus, the parameters for the switching-prohibited period should be set carefully.

As mentioned previously, CAN sample timing varies slightly for each bit and depends on the signaling status. Moreover, the logical flip can be multiple pulses per switching action. Considering these factors, the switching-prohibited time length is expressed as

$$T_{\text{SP}} = \frac{0.2}{\text{CAN baud rate [bps]}} + T_{\text{flip}} \tag{5.1}$$

where T_{SP} is the switching-prohibited time length, and T_{flip} is the maximum total time length of logical flips per switching action of the converter MOSFET. Equation (5.1) assumes that the variation of a sample point is 10% of the bit time length, and TSP is set after 60% of each bit. In this study, the CAN baud rate

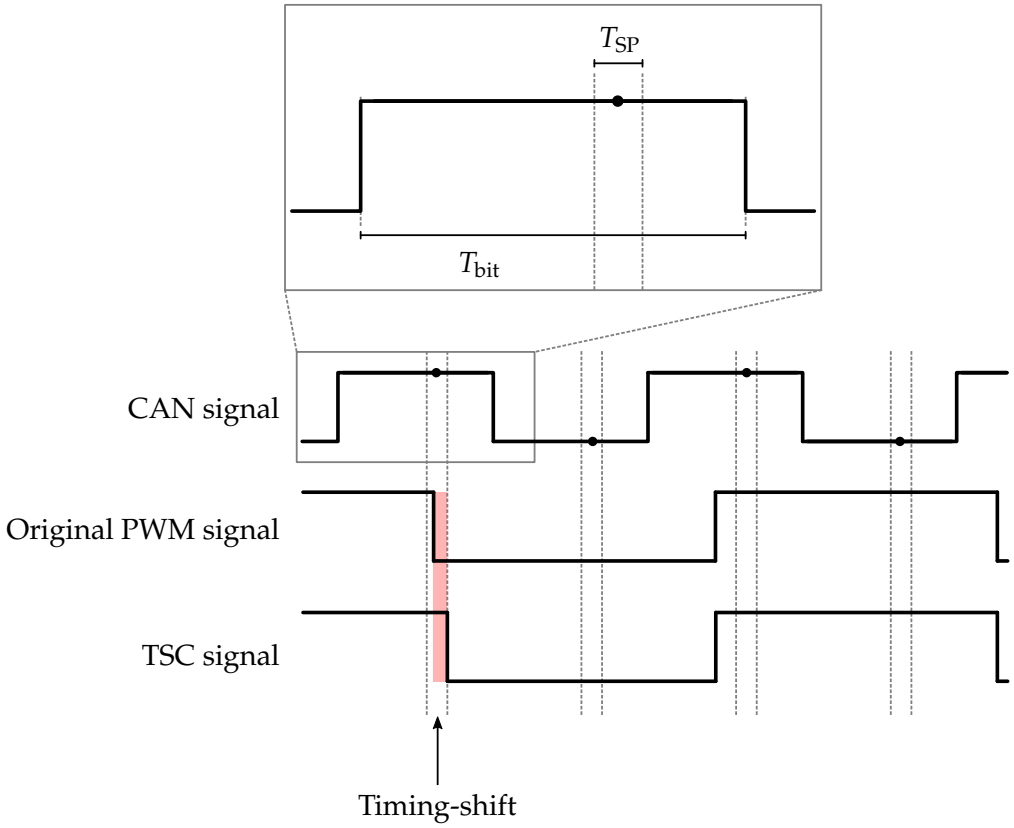

FIGURE 5.7: Timing chart of the TSC operation

was set to 125 kbps. Additionally, to employ TSC, the following relation must be satisfied:

$$T_{flip} < T_{bit} = \frac{2}{\text{CAN baud rate [bps]}} \tag{5.2}$$

where T_{bit} represents the bit time length, which can be obtained using the inverse of the halved CAN baud rate. In the noise injection system, T_{flip} was approximately 300 ns, as derived from the measurement waveform; it was sufficiently shorter than T_{bit} (8 µs). Therefore, TSC was observed to be applicable to the noise injection system, and T_{SP} was set to 1.1 μs following these criteria.

5.2.2 Experimental Verification

To apply TSC to the noise injection system, the FPGA-based converter controller was modified to implement the TSC function. The noise injection system configuration was not changed except for the FPGA program. Importantly, the noise

injection system did not incorporate additional EMI reduction methods, such as a filter circuit and shielded cable.

TABLE 5.1. Experimental results of the FER test

	Without TSC	With TSC
Test 1	4.6%	0.0%
Test 2	4.6%	0.0%
Test 3	6.1%	0.0%

The experimental results of the FER test are shown in Table 5.1. In this verification, the FER represents how many CAN errors occur as an index. The FER is calculated using

$$\text{FER}\,[\%] = \frac{\text{Error frames in Rx node}}{\text{Transmitted frames from Tx node}} \cdot 100 \tag{5.3}$$

When the CAN frame includes a bit error, the Rx node detects the error and processes it following the protocol. Hence, the Rx node controller can log the communication status. Because the FER fluctuates depending on the phase between the converter switching signal and communication signal, manifold frames are required to obtain statistical data. For the verification test, the Tx node sent 1,000 frames, which contained exactly the same data, at a constant 50-ms frame interval. Subsequently, the FER was obtained by extracting the number of frames that included an error bit from the log of the Rx node. The test was conducted three times. The converter operating conditions, with and without the TSC function, were as follows: a DC bus voltage of 100 V and a switching frequency of 30 kHz. In addition, the converter controller employed triangular modulation of the duty cycle between 0.2 and 0.8 at 10 Hz to demonstrate the effectiveness of TSC under a varying switching timing. According to the experimental results, the FER was noticeably suppressed when the TSC function operated in the noise injection system. Thus, the proposed method realizes effective EMI reduction without relying on conventional EMI methods.

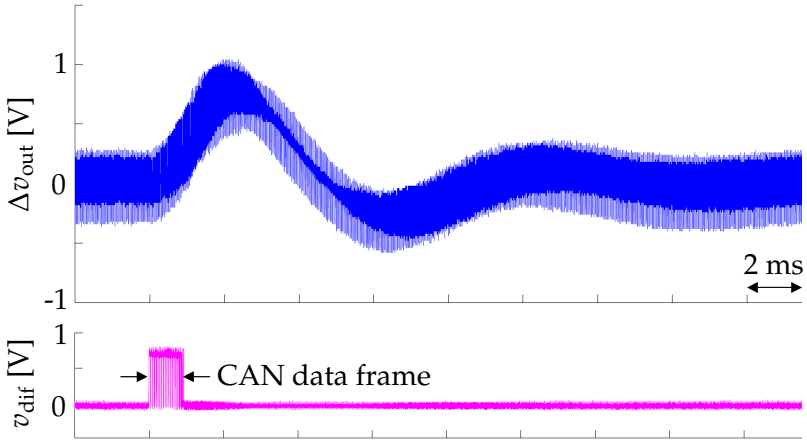

FIGURE 5.8: Timing chart of the compensated TSC operation

5.3 Timing-Shift Control with Pulse-Width Compensation Function

Although the experimental verification demonstrated that TSC suppresses communication failure, there is a concern regarding the converter control performance, because the TSC slides the switching timing regardless of the PWM control, and the switching duty ratio changes unintentionally. This results in an undesirable pulsation of the output voltage and may affect the lifetime of the load. In addition to the feedback control of the output voltage that is straightforward and effective, this paper proposes a duty cycle compensation scheme to compensate the shifted duty ratio immediately as an approach to suppress disturbances in advance.

The duty cycle compensation for suppressing the converter output disturbance owing to TSC operation is shown in Fig. 5.8. When converter switching timing is delayed to avoid a coincidence with a CAN sample point, the next switching timing is adjusted to maintain the original duty ratio. The compensation control equalizes the shifted time length (T_{sft}) and compensated time length (T_{cmp}). This function was built into the FPGA-based controller of the noise injection system.

The converter output voltage is a simple index for evaluating the control performance because the voltage pulse characteristics depend on how the PWM control is disturbed by the TSC function. Thus, the proposed method was verified by comparing the converter output voltage during the TSC operation. Because

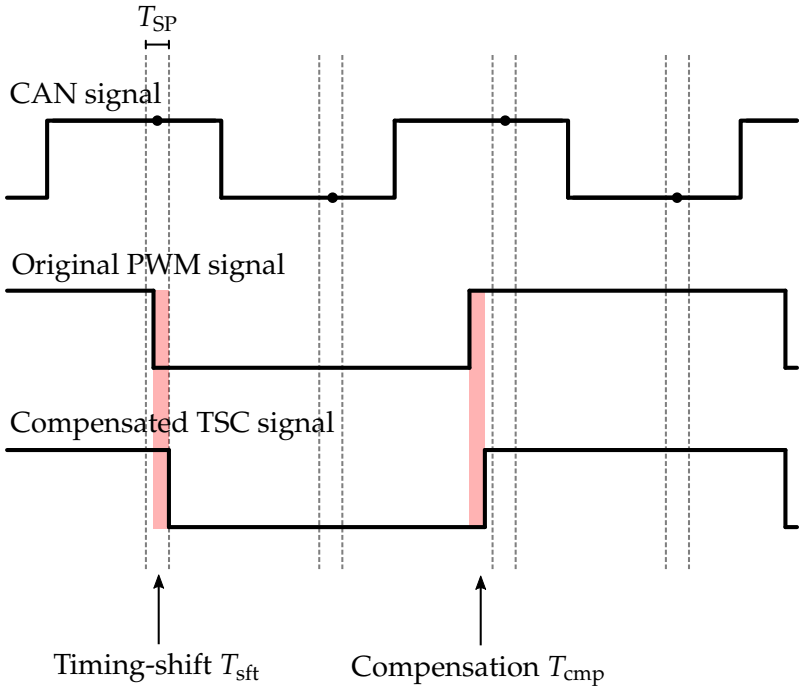

FIGURE 5.9: Timing chart of the compensated TSC operation

timing shifts occur randomly, the voltage amplitude of disturbances varies. Accordingly, the maximum amplitudes of a disturbance with and without the compensation technique were compared for experimental verification. The converter operating conditions, with and without the TSC function, were as follows: a DC bus voltage of 100 V, switching frequency of 30 kHz, and constant duty cycle of 0.5.

The measured waveform of the converter output voltage and the Rx output signal of the transceiver were recorded as shown in Fig. 5.10 to verify the compensation method under TSC operation. To measure the output voltage accurately, we observed only the AC components. The comparison results of the peak voltage indicated that the pulsation peak decreased by 64% without including a DC component. Although the peak value depends on the total shifted time length by the TSC function and the converter impedance, this compensation method is effective in reducing the disturbance. In addition, as the FER tests shown in Table 5.2 indicate, the modified TSC still suppresses the FER sufficiently.

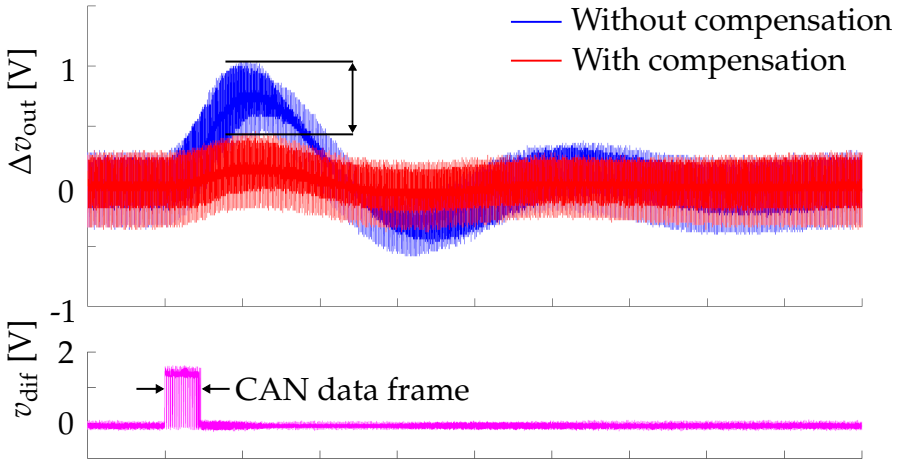

FIGURE 5.10: Measured waveform of the converter output voltage v_{out} and Rx output voltage v_{Rx} to compare the performance of the compensation method under TSC operation

TABLE 5.2. Experimental results of the FER test

	Without TSC	With modified TSC
Test 1	5.1%	0.0%
Test 2	5.3%	0.0%
Test 3	4.1%	0.0%

5.4 Summary

This chapter presents techniques for time-dependent error mitigation for the buck converter. The SSC method reduces EMI by synchronizing a converter switching signal and a CAN communication signal, but it introduces limitations in the converter control.

Subsequently, the TSC method is developed as a more practical approach of reducing the EM disturbance. The TSC avoids a timing collision between a converter switching and a CAN sample by slightly sliding the converter switching. Since a timing-shift control changes the switching duty ratio irrespective of the target value, a converter output disturbance can occur. A compensation technique was applied to the TSC to solve the problem. The compensation method maintains an original duty ratio and suppresses the output disturbance. Importantly, the experimental verification shows that the TSC perfectly prevents communication errors.

Chapter 6

Digital Denoising Methods for the CAN Communication System

This chapter describes a digital denoising method for the CAN communication system that prevents communication errors without conventional EMI reduction methods. As the first step to developing the method, the synchronous denoising method retrieves an error pulse based on a converter switching timing. Moreover, the autonomous denoising method realizes the error retrieval without monitoring a converter switching signal.

6.1 Synchronous Digital Denoising Method

For preventing the logical flip event in a CAN sample, this section presents a synchronous digital denoising (SDD) method that is feasible in the CAN communication system. Fig. 6.1 depicts a timing chart for describing the operation of the synchronous denoising. In the generic CAN physical layer, the controller samples a single point per bit of communication signal via a transceiver IC, which converts a differential signal to a digital signal. Moreover, an induced CM noise in the CAN bus barely flows to the receiver output (v_{Rx}) that is read by the controller. Hence, by eliminating a logical flip of the receiver output when a converter switching occurs, the controller receives a communication signal without an error signal. This function can be realized by changing the CAN signal process. However, modifications of the CAN protocol will not be practical for conventional systems.

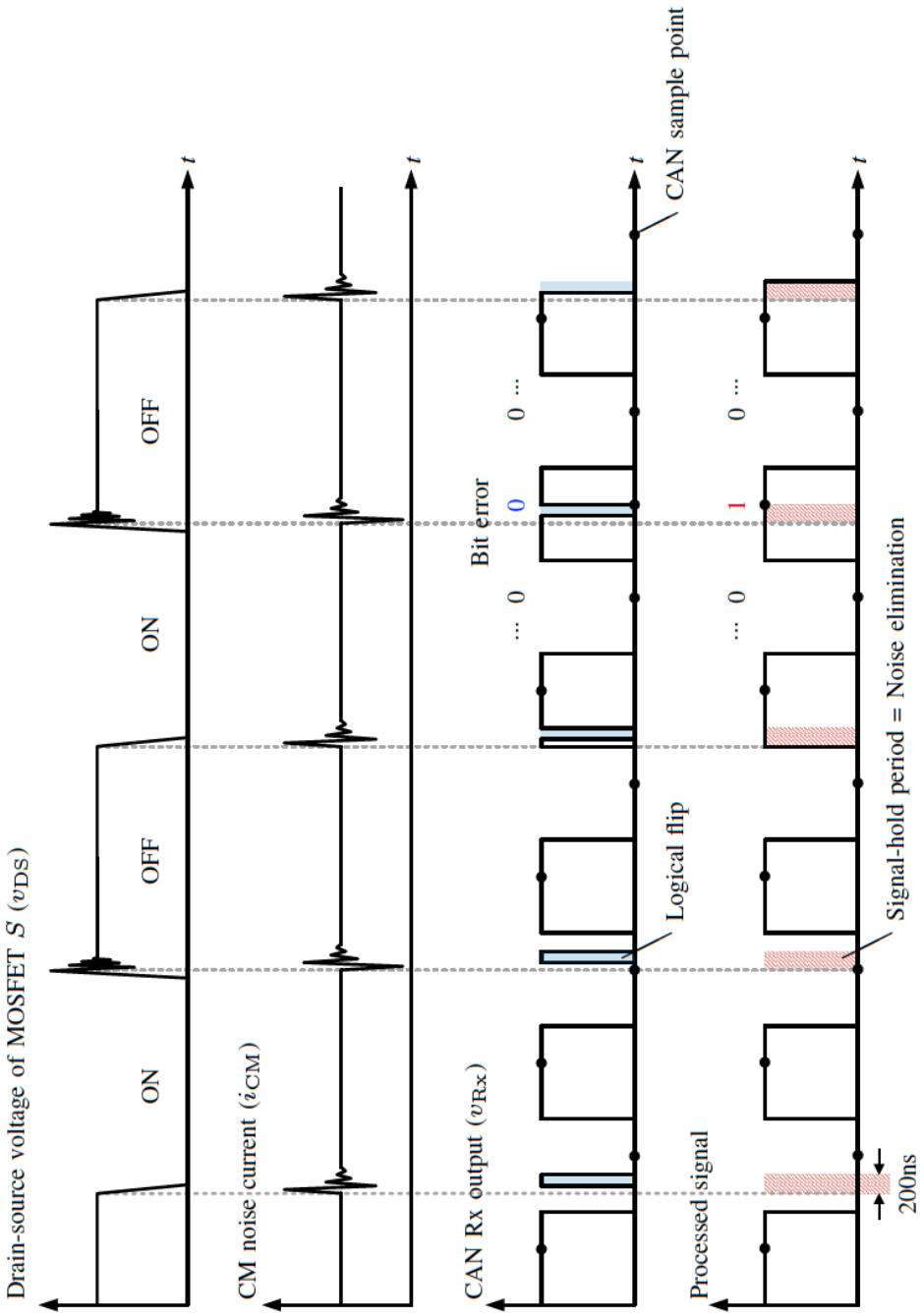

FIGURE 6.1: Timing chart to describe the operation of the CAN synchronous denoising method

Therefore, to implement the proposed method to the test system, the receiver is connected to the controller via the FPGA that generates converter switching signal assuming that the controller and the FPGA operate as a single processor. Owing to this configuration, the controller operates without changing the protocol, which facilitates embedding of the proposed method even to conventional systems. Hence, no additional hardware is required to apply this method to the test system, which may results in a cost reduction of the system.

The FPGA processes the Rx output signal (v_{Rx}) to prevent logical flips based on a converter switching timing. As depicted in Fig. 6.1, v_{Rx} is held for 200 ns after every converter switching action. The hold time may cause timing jitters of the communication signal, but it does not deteriorate the signal integrity as the hold time is sufficiently short. The hold time width derives from the time length of the logical flip that is observed in the receiver output.

The CAN Rx error counter value is suitable for tracking the number of errors due to the converter EMI noise [101]. The Rx error counter function is built into the protocol for error confinement of CAN bus traffic. Several rules govern the incrementation of error counters when the controller detects an error or their decrease during successful data transmission. When the Rx error counter is over a 127, the Rx node first assumes an "error passive" state, and when the Rx counter reaches 255, it transfers to the "bus off" state which means that the Rx node does not participate in the communication. Therefore, the Rx error counter should be suppressed to ensure slew-rate and reliable communications. Accordingly, as the first verification of the proposed method, the Rx error counter value was monitored by transmitting 1000 data frames from the Tx (transmitter) node. The CAN system operated at 125 kbps and transmitted frames every 50 ms. For the converter operating condition, the switching frequency was set to 30 kHz and the duty ratio was kept constant at 0.5. Figs. 6.2(a) and (b) show the measured Rx error counter value with a time series number of CAN data frames. The results confirmed that the proposed method is effective in suppressing the Rx error counter value and it makes the communications more robust.

Furthermore, CAN FLR tests were performed under the same converter operation as monitoring the Rx error counter value. The FER is an index corresponding to a slew rate of CAN communication. If the CAN loses a data frame owing to an EMI noise, the Tx node sends the same data frame again, which results in almost doubling data transmission time. Notably, the slew rate is a significant

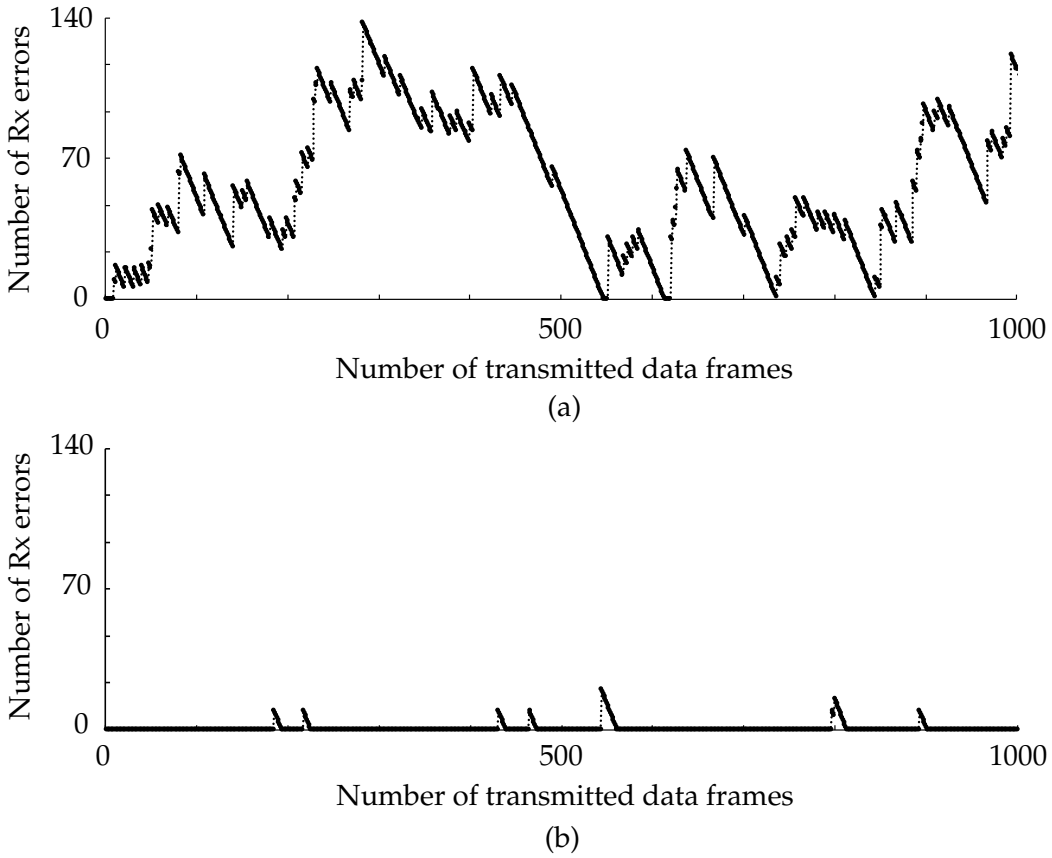

FIGURE 6.2: Measured Rx error counter value (a) Without the synchronous denoising. (b) With the synchronous denoising.

concern in systems where real-time performance is required. Again, by transmitting 1000 data frames from the Tx node, lost frames were counted to calculate the FLR in the Rx node. As shown in Table 6.1, the FLR was suppressed by 5.68% compared with that without the synchronous denoising. Therefore, the proposed method makes the communications more robust against the converter EMI noise.

TABLE. 6.1. Measured CAN frame loss rate

	Without synchronous denoising	With synchronous denoising
CAN FLR	6.68%	1.00%

6.2 Autonomous Digital Denoising Method

6.2.1 Implementation of the Denoising Method

An error in CAN communication occurs when the CAN controller reads the logic flip that occurs in the output voltage of the transceiver during switching of the

buck chopper circuit. This section presents an autonomous digital denoising (ADD) method that can detect the timing of the logic flip using the noise voltage on the communication bus and correct the flip signal using digital signal processing. When the noise voltage is detected by measuring the midpoint voltage on the bus, the noise voltage is superimposed on the communication signal; therefore, it is necessary to separate the signal from the noise.

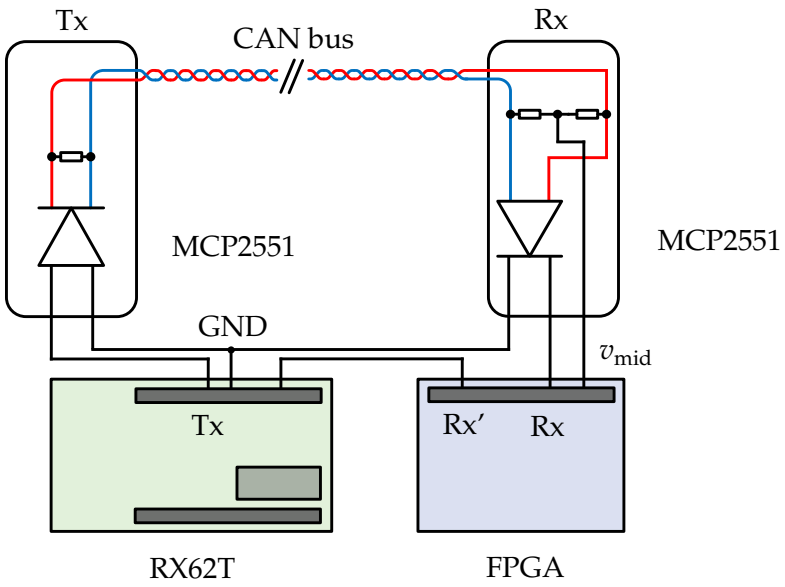

FIGURE 6.3: Configuration of the bit error rate test circuit with the ADD function

In the CAN communication system, it is common to divide the termination resistor and connect a capacitor for the common mode filter to the midpoint; thus, the midpoint potential can be easily obtained. Fig. 6.3 shows the configuration of a CAN communication system that applies the ADD method. In the target CAN node, the communication signal (output voltage of the transceiver IC) and the midpoint potential of the bus are input to the standard I/O pins of the FPGA. Fig. 6.4 shows the timing chart of ADD. When a noise-induced voltage is generated at the bus midpoint potential (v_{mid}) owing to the operation of the step-down chopper circuit, a logic reversal signal is generated in the communication signal Rx. In response to this, the logic reversal signal is removed in the FPGA, and the signal Rx' is transmitted to the BER measurement device to realize a series of operations. However, if the noise voltage detection and error correction processing for the communication signal are to be performed in real time, it is not practical to perform the process from noise voltage detection to error processing within 10 to 50 ns. Therefore, a delay of 100 ns or more is always input to the communication

signal in the FPGA to allocate sufficient time for error correction processing. In addition, the intentional delay may make it easier to apply this method without using a high-performance processor such as an FPGA.

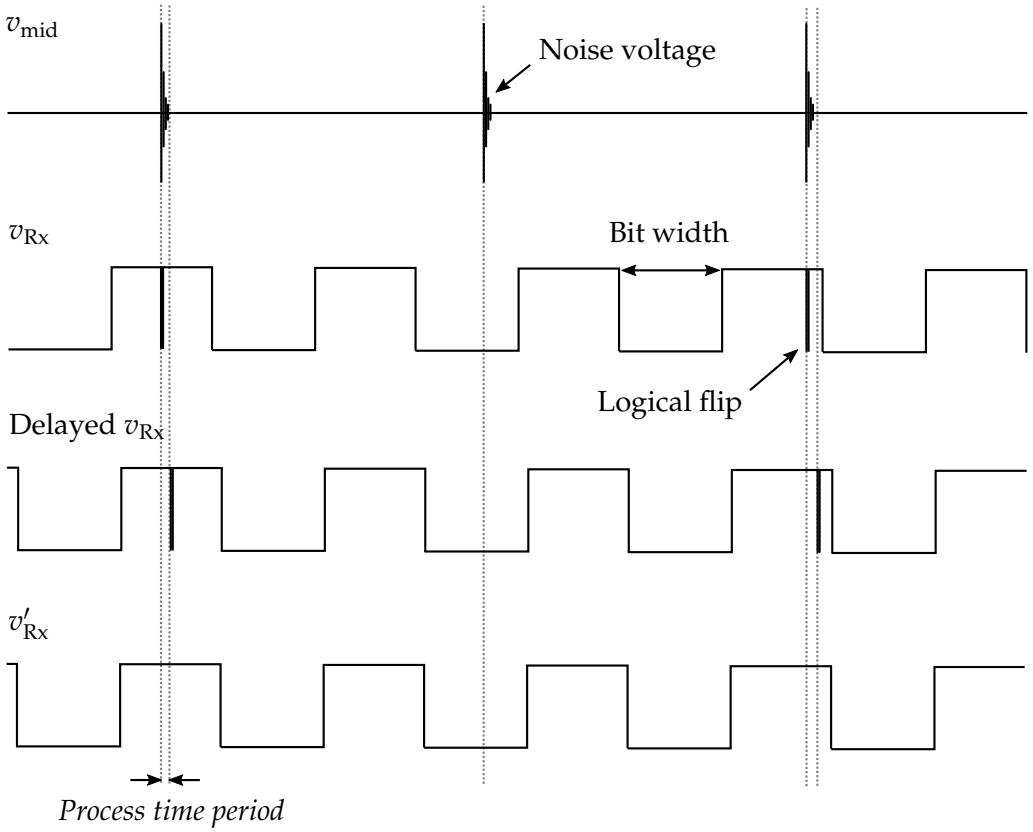

FIGURE 6.4: Timing chart of ADD operation

6.2.2 Experimental Verification

In a noise injection system using the ADD method, the BER was measured to verify the reduction effect of electromagnetic interference. The operating conditions of the buck chopper circuit were set to an input voltage of 100 V, switching frequency of 100 kHz, and constant switching duty ratio of 0.5. Table 6.2 shows the measured BER when the ADD technique was applied; the error rate was significantly suppressed compared with the condition without ADD. The BER changed irregularly with the load current, and the principle in which the error cannot be completely reduced will be investigated in the future.

TABLE 6.2: Bit error rate measurement result

Load current [A]	2.0	2.5	3.0	3.5	4.0	4.5	5.0
Without ADD	16.3%	16.3%	18.4%	19.4%	21.5%	22.4%	23.5%
With ADD	0.13%	0.06%	0.06%	0.11%	0.10%	0.14%	0.15%

6.3 Summary

First, this chapter describes a CAN synchronous denoising method to suppress the EMI on the communication based on the EMI analysis of the communication near a buck converter. In the test system, the buck converter generates a CM noise with a switching action and induces a ringing noise in the communication cables. The induced noise results in a CAN bit error when the noise timing coincides with a sample point. For prevention of the coincidence, the synchronous denoising method is proposed and was verified through an experiment. Under the synchronization with the buck converter, the method eliminates logical flips of the Rx output by holding the signal in a moment without using additional hardware components.

Second, the autonomous denoising technique is introduced. Owing to the noise detecting function, the method enables a CAN node to eliminate error signals independently. An experimental verification demonstrated that it effectively reduces communication errors. Furthermore, from the implementation perspective, the ADD method has a remarkable feature in that synchronization between the buck converter and the CAN communication system is unnecessary.

Chapter 7

Conclusion and Outlook

7.1 Conclusions of the Research

Chapter 1 clarifies the background and motivations of the research. Reviewing the actual incidents caused by EMI noise of the SMPSs, the technical problems that this research addressed are stated.

Chapter 2 provides a literature survey related to EMC of SMPSs and CAN systems. The review reveals that, for solving EM disturbance on CAN, the time-domain phenomenon is a significant factor in understanding the physics underlying the disturbance and developing effective solutions.

Chapter 3 presents the time-domain analysis of the disturbance caused by a buck converter on CAN communication. Using experimental and simulation verification, we analyzed the noise propagation and CAN error occasion mechanisms. Furthermore, the error rate tests quantified the EM disturbance, which indicated that the noise waveform of the communication line corresponds to the operating condition of the buck converter.

Chapter 4 proposes the time series control of an AGD to balance EM disturbance mitigation and converter performance. The proposed control of the AGD realized an effective EMI reduction with a focus on the CAN data transmission behavior.

Chapter 5 describes the timing-shift control of the buck converter that realizes the EMI reduction using converter control. Unlike the conventional EMI reduction approaches, the control method prevents communication error even if the buck converter induces a noise to the communication line. Despite the control

suppressing an EM disturbance, shifting a switching timing potentially undermines the converter control stability. To solve the problem, a duty compensation method is added to the control and it improves the converter control stability.

Chapter 6, in contrast to the timing-shift control on the converter side, proposes the digital denoising technique that enables a CAN processor to remove error signals digitally. The denoising methods achieve effective EMI reduction only by the digital maneuver. In the entire work, this thesis has presented primarily three approaches, which are shown in Table 7.1.

7.2 Future Outlook

This research focused on the EM disturbance on CAN caused by a buck converter. Accordingly, the time-domain analysis approach and proposed EMI reduction methods can be extended to various applications. Moreover, the following are the technical challenges that remain:

Future Work

- Extending the time-domain analysis approach and proposed EMI reduction methods to other PE converters, communication protocols, and various topologies.
- Detailed study of EM coupling mechanism between PE converters and serial communication systems.
- Clarifying the design criteria and technical restrictions of the proposed EMI reduction methods.

TABLE 7.1: Proposed EMI reduction approaches of the study

Proposed approach	Chapter 4 Time-series control of active gate driver	Chapter 5 Timing-shift control of buck converter	Chapter 6 Digital denoising methods
Additional hardware cost	-	+++	++
Converter performance	-	-	+++
Multi-CAN nodes	+++	+	+++
Converter switching frequency	+++	+	+
Communication baud rate	+++	+	+
Possible applications	Low-traffic communication	High-power applications	Communication systems with high-performance CPUs

Bibliography

[1] L. Tihanyi, *EMC in Power Electronics*, en. Newnes, Apr. 1995.

[2] T. Williams, *EMC for Product Designers*. Elsevier, Sep. 2016.

[3] G. Engelmann, A. Sewergin, M. Neubert, and R. W. D. Doncker, "Design challenges of sic devices for low- and medium-voltage dc-dc converters," *IEEJ Journal of Industry Applications*, vol. 8, no. 3, pp. 505–511, 2019.

[4] B. Zhang and S. Wang, "A survey of EMI research in power electronics systems with Wide-Bandgap semiconductor devices," *IEEE Journal of Emerging and Selected Topics in Power Electronics*, vol. 8, no. 1, pp. 626–643, Mar. 2020.

[5] K. Mainali and R. Oruganti, "Conducted EMI mitigation techniques for Switch-Mode power converters: A survey," *IEEE Trans. Power Electron.*, vol. 25, no. 9, pp. 2344–2356, Sep. 2010.

[6] Japan Transport Safety Board, "Railway accident investigation report," JP, 2009.

[7] Honda Motor Co. , Ltd., "Recall information," Tech. Rep., Oct. 2014.

[8] *In compliance magazine*, EN, `https://incompliancemag.com/`, Accessed: 2021-11-4, Jan. 2020.

[9] D. Hristu-Varsakelis and W. S. Levine, Eds., *Handbook of Networked and Embedded Control Systems*. Birkhäuser Boston, 2005.

[10] International Organization for Standardization, "Road vehicles — controller area network (CAN) — part 2: High-speed medium access unit," Tech. Rep. ISO 11898-2:2016, Dec. 2016.

[11] Y. S. Cheng, T. Mannen, K. Wada, K. Miyazaki, M. Takamiya, and T. Sakurai, "Optimization platform to find a switching pattern of digital active gate drive for reducing both switching loss and surge voltage," *IEEE Trans. Ind. Appl.*, vol. 55, no. 5, pp. 5023–5031, Sep. 2019.

[12] H. Obara, K. Wada, K. Miyazaki, M. Takamiya, and T. Sakurai, "Active gate control in Half-Bridge inverters using programmable gate driver ICs

to improve both surge voltage and converter efficiency," *IEEE Trans. Ind. Appl.*, vol. 54, no. 5, pp. 4603–4611, Sep. 2018.

[13] Y. Chen, F. Zhuo, W. Pan, F. Zhang, and L. Feng, "A novel active gate driver for static and dynamic current balancing of parallel-connected IGBTs," in *2017 IEEE Applied Power Electronics Conference and Exposition (APEC)*, Mar. 2017, pp. 795–799.

[14] P. Bogónez-Franco and J. B. Sendra, "EMI comparison between si and SiC technology in a boost converter," in *International Symposium on Electromagnetic Compatibility - EMC EUROPE*, Sep. 2012, pp. 1–4.

[15] S. Yin, K. J. Tseng, P. Tu, R. Simanjorang, and A. K. Gupta, "Design considerations and comparison of high-speed gate drivers for si IGBT and SiC MOSFET modules," in *2016 IEEE Energy Conversion Congress and Exposition (ECCE)*, Sep. 2016, pp. 1–8.

[16] X. Gong and J. A. Ferreira, "Comparison and reduction of conducted EMI in SiC JFET and si IGBT-Based motor drives," *IEEE Trans. Power Electron.*, vol. 29, no. 4, pp. 1757–1767, Apr. 2014.

[17] L. Middelstaedt, B. Strauss, and A. Lindemann, "Analyzing EMI issues in a DC DC converter using GaN instead of si power transistors," in *23rd European Conference on Power Electronics and Applications (EPE'21 ECCE Europe)*, 2021.

[18] H. Wang and F. Blaabjerg, "Power electronics reliability: State of the art and outlook," *IEEE Journal of Emerging and Selected Topics in Power Electronics*, vol. 9, no. 6, pp. 6476–6493, Dec. 2021.

[19] J. Wyss and J. Biela, "Optimal design of bidirectional PFC rectifiers and inverters considering 2L and 3L topologies with si, SiC, and GaN switches," en, *IEEJ j. ind. appl.*, vol. 8, no. 6, pp. 975–983, Nov. 2019.

[20] W. Perdikakis, M. J. Scott, K. J. Yost, C. Kitzmiller, B. Hall, and K. A. Sheets, "Comparison of si and SiC EMI and efficiency in a Two-Level aerospace motor drive application," *IEEE Transactions on Transportation Electrification*, vol. 6, no. 4, pp. 1401–1411, Dec. 2020.

[21] M. R. Yazdani, H. Farzanehfard, and J. Faiz, "Classification and comparison of EMI mitigation techniques in switching power converters - a review," *J. power electron.*, vol. 11, no. 5, pp. 767–777, Sep. 2011.

[22] R. Yamada, R. Araumi, S. Fujita, and K. Wada, "Conductive noise suppression with cancelling for miniaturization of EMI filters in PFC converter," *IEEJ Journal of Industry Applications*, vol. advpub, 2021.

[23] R. Goswami, S. Wang, E. Solodovnik, and K. J. Karimi, "Differential mode active EMI filter design for a boost power factor correction AC/DC converter," *IEEE Journal of Emerging and Selected Topics in Power Electronics*, vol. 7, no. 1, pp. 576–590, Mar. 2019.

[24] B. Narayanasamy and F. Luo, "A survey of active EMI filters for conducted EMI noise reduction in power electronic converters," *IEEE Trans. Electromagn. Compat.*, vol. 61, no. 6, pp. 2040–2049, Dec. 2019.

[25] D. Shin, S. Jeong, Y. Baek, C. Park, G. Park, and J. Kim, "A balanced feedforward Current-Sense Current-Compensation active EMI filter for Common-Mode noise reduction," *IEEE Trans. Electromagn. Compat.*, vol. 62, no. 2, pp. 386–397, Apr. 2020.

[26] D. Shin, S. Kim, G. Jeong, *et al.*, "Analysis and design guide of active EMI filter in a compact package for reduction of Common-Mode conducted emissions," *IEEE Trans. Electromagn. Compat.*, vol. 57, no. 4, pp. 660–671, Aug. 2015.

[27] Y. Chu, S. Wang, and Q. Wang, "Modeling and stability analysis of Active/Hybrid Common-Mode EMI filters for DC/DC power converters," *IEEE Trans. Power Electron.*, vol. 31, no. 9, pp. 6254–6263, Sep. 2016.

[28] M. L. Heldwein and J. W. Kolar, "Impact of EMC filters on the power density of modern Three-Phase PWM converters," *IEEE Trans. Power Electron.*, vol. 24, no. 6, pp. 1577–1588, Jun. 2009.

[29] F. Musolino and P. S. Crovetti, "Interference of Spread-Spectrum modulated disturbances on digital communication channels," *IEEE Access*, vol. 7, pp. 158 969–158 980, 2019.

[30] A. Bendicks, S. Frei, N. Hees, and M. Wiegand, "Systematic reduction of peak and average emissions of power electronic converters by the application of spread spectrum," *IEEE Trans. Electromagn. Compat.*, vol. 60, no. 5, pp. 1571–1580, Oct. 2018.

[31] F. Pareschi, R. Rovatti, and G. Setti, "EMI reduction via spread spectrum in DC/DC converters: State of the art, optimization, and tradeoffs," *IEEE Access*, vol. 3, pp. 2857–2874, 2015.

[32] R. Mukherjee, A. Patra, and S. Banerjee, "Impact of a frequency modulated pulsewidth modulation (PWM) switching converter on the input power system quality," *IEEE Trans. Power Electron.*, vol. 25, no. 6, pp. 1450–1459, Jun. 2010.

[33] P. Lezynski, "Random modulation in inverters with respect to electromagnetic compatibility and power quality," *IEEE Journal of Emerging and Selected Topics in Power Electronics*, vol. 6, no. 2, pp. 782–790, Jun. 2018.

[34] S. Ohn, J. Yu, R. Burgos, D. Boroyevich, and H. Suryanarayana, "Reduced Common-Mode voltage PWM scheme for Full-SiC Three-Level uninterruptible power supply with small DC-Link capacitors," *IEEE Trans. Power Electron.*, vol. 35, no. 8, pp. 8638–8651, Aug. 2020.

[35] M. Liang, Y. Li, Q. Chen, *et al.*, "Research on an improved DC-side snubber for suppressing the turn-off overvoltage and oscillation in high speed SiC MOSFET application," in *2017 IEEE Energy Conversion Congress and Exposition (ECCE)*, Oct. 2017, pp. 1358–1365.

[36] A. P. Camacho, V. Sala, H. Ghorbani, and J. L. R. Martinez, "A novel active gate driver for improving SiC MOSFET switching trajectory," *IEEE Trans. Ind. Electron.*, vol. 64, no. 11, pp. 9032–9042, Nov. 2017.

[37] P. Nayak and K. Hatua, "Active gate driving technique for a 1200 V SiC MOSFET to minimize detrimental effects of parasitic inductance in the converter layout," *IEEE Trans. Ind. Appl.*, vol. 54, no. 2, pp. 1622–1633, Mar. 2018.

[38] Y. Yang, Y. Wen, and Y. Gao, "A novel active gate driver for improving switching performance of High-Power SiC MOSFET modules," *IEEE Trans. Power Electron.*, vol. 34, no. 8, pp. 7775–7787, Aug. 2019.

[39] M. Farsi, M. Barbosa, and K. Ratcliff, "An overview of controller area network," en, *Comput. control eng. j.*, vol. 10, no. 3, pp. 113–120, Jun. 1999.

[40] Robert Bosch GmbH, *CAN specification version 2.0*, 1991.

[41] F. Ruan, S. Sun, T. Dlugosz, and L. Zhang, "Some consideration on electromagnetic compitibility in can bus design of automobile," *2010 Asia-Pacific International Symposium on Electromagnetic Compatibility*, 2010.

[42] M. Ohara, M. Arai, and S. Fukumoto, "A note on influence of DC-DC converter noise in CAN networks," in *2013 IEEE 19th Pacific Rim International Symposium on Dependable Computing*, Dec. 2013, pp. 134–135.

[43] W. Xing, H. Chen, and H. Ding, "The application of controller area network on vehicle," *Proceedings of the IEEE International Vehicle Electronics Conference (IVEC'99) (Cat. No.99EX257)*, 1999.

[44] F. Ren, Y. R. Zheng, M. Zawodniok, and J. Sarangapani, *Effects of electromagnetic interference on control area network performance*, 2007.

[45] M. Fontana, F. G. Canavero, and R. Perraud, "Integrated circuit modeling for noise susceptibility prediction in communication networks," *IEEE Trans. Electromagn. Compat.*, vol. 57, no. 3, pp. 339–348, Jun. 2015.

[46] Microchip Technology Inc, *High-Speed CAN transceiver MCP2551*, 2010. [Online]. Available: `http://ww1.microchip.com/downloads/en/devicedoc/21667e.pdf`.

[47] TDK Corporation Magnetics Business Group, "EMC countermeasures for In-Vehicle communication networks,"

[48] M. Robertson, "Simplify CAN bus implementations with chokeless transceivers," [Online]. Available: `https://www.ti.com/lit/wp/slly020/slly020.pdf?ts=1647779799981&ref_url=https%253A%252F%252Fwww.google.com%252F`.

[49] *NXP® semiconductors official site*, Accessed: 2022-1-28. [Online]. Available: `https://www.nxp.com`.

[50] F. Klotz, M. Roebl, B. Koerber, and N. Mueller, "New standardized EMC evaluation methods for communication transceivers," *IEEE Letters on Electromagnetic Compatibility Practice and Applications*, vol. 1, no. 1, pp. 14–19, Mar. 2019.

[51] International Electrotechnical Commission, "Integrated circuits – EMC evaluation of transceivers – part 3: CAN transceivers," Tech. Rep. IEC 62228-3:2019, 2019.

[52] S. Matsushima, T. Matsushima, T. Hisakado, and O. Wada, "Trends of EMC standards for automotive network devices and communication quality of ethernet in relation to parameters of pulse disturbances," *IEEE Electromagn. Compat. Mag.*, vol. 7, no. 1, pp. 46–50, 2018.

[53] International Organization for Standardization, "Road vehicles — electrical disturbances from conduction and coupling — part 3: Electrical transient transmission by capacitive and inductive coupling via lines other than supply lines," Tech. Rep. ISO 7637-3:2016, 2016.

[54] *EMC test equipment catalog 2021-2022*, Noise Laboratory Co., Ltd.

[55] Ford Motor Company, "Electromagnetic compatibility specification for Electrical/Electronic components and subsystems," Tech. Rep. EMC-CS-2009.1, 2009.

[56] S. Jeschke, J. Loos, M. Kleinen, *et al.*, *Susceptibility of 100Base-T1 communication lines to coupled fast switching High-Voltage pulses*, 2020.

[57] T. Matsushima, O. Wada, K. Takaya, and Y. Okugawa, *Mode conversion and transfer characteristics of conducted disturbance to ethernet device from power supply cable*, 2015.

[58] S. Mortazavi, D. Schleicher, A. Stieler, A. Sinai, F. Gerfers, and M. Hampe, *EMC analysis of shielded twisted pair and shielded parallel pair transmission lines for automotive Multi-Gig ethernet*, 2019.

[59] H. Ogura, R. Isshiki, K. Iokibe, Y. Kodera, T. Kusaka, and Y. Nogami, "Electrical falsification of CAN data by magnetic coupling," in *2020 35th International Technical Conference on Circuits/Systems, Computers and Communications (ITC-CSCC)*, Jul. 2020, pp. 348–353.

[60] C. Juexiao, G. Minjie, L. Feng, and S. Zechang, *EMC comparison of unshielded twisted pair and shielded twist pair in automotive CAN-bus*, 2009.

[61] H. Chen and T. Wang, "Estimation of Common-Mode current coupled to the communication cable in a motor drive system," *IEEE Trans. Electromagn. Compat.*, vol. 60, no. 6, pp. 1777–1785, Dec. 2018.

[62] H. Chen, Y. Yan, and H. Zhao, "Extraction of Common-Mode impedance of an Inverter-Fed induction motor," *IEEE Trans. Electromagn. Compat.*, vol. 58, no. 2, pp. 599–606, Apr. 2016.

[63] K. Niewiadomski, P. Leżyński, R. Smoleński, J. Bojarski, M. Sumner, and D. W. P. Thomas, "Time-domain assessment of data transmission errors in systems with multiple DC/DC converters," in *2020 International Symposium on Electromagnetic Compatibility - EMC EUROPE*, Sep. 2020, pp. 1–6.

[64] K. L. Kaiser, *Transmission Lines, Matching, and Crosstalk*. CRC Press, 2005.

[65] M. Fontana and T. H. Hubing, "Characterization of CAN network susceptibility to EFT transient noise," *IEEE Transactions on Electromagnetic Compatibility*, vol. 57, no. 2, pp. 188–194, 2015, ISSN: 00189375.

[66] W. Prodanov, M. Valle, and R. Buzas, "A Controller Area Network Bus Transceiver Behavioral Model for Network Design and Simulation," *IEEE Transactions on Industrial Electronics*, vol. 56, no. 9, pp. 3762–3771, 2009.

[67] A. N. Lemmon, R. Cuzner, J. Gafford, R. Hosseini, A. D. Brovont, and M. S. Mazzola, "Methodology for characterization of Common-Mode conducted electromagnetic emissions in Wide-Bandgap converters for ungrounded shipboard applications," *IEEE Journal of Emerging and Selected Topics in Power Electronics*, vol. 6, no. 1, pp. 300–314, Mar. 2018.

[68] M. L. Heldwein and J. W. Kolar, "Winding capacitance cancellation forThree-Phase EMC input filters," *IEEE Trans. Power Electron.*, vol. 23, no. 4, pp. 2062–2074, Jul. 2008.

[69] D. N. Dalal, N. Christensen, A. B. Jørgensen, *et al.*, "Impact of power module parasitic capacitances on Medium-Voltage SiC MOSFETs switching transients," *IEEE Journal of Emerging and Selected Topics in Power Electronics*, vol. 8, no. 1, pp. 298–310, Mar. 2020.

[70] Q. Zhang, N. Sinenian, and R. Huang, "Investigations on electrolytic capacitors to improve reliability under Assembly-Level impact conditions," in *2019 20th International Conference on Electronic Packaging Technology(ICEPT)*, Aug. 2019, pp. 1–4.

[71] International Electrotechnical Commission, "Railway applications - rolling stock equipment - capacitors for power electronics - part 2: Aluminium electrolytic capacitors with non-solid electrolyte," Tech. Rep. IEC 61881-2:2012, 2012.

[72] *Aluminum electrolytic capacitors*, Nippon Chemi-Con, 2021. [Online]. Available: `https://www.chemi-con.co.jp/en/catalog/pdf/al-e/al-all-e1001u-2020.pdf`.

[73] M. Tamate, T. Sasaki, and A. Toba, "Quantitative estimation of conducted emission from an inverter system," *IEEJ Transactions on Industry Applications*, vol. 128, no. 3, pp. 193–200, 2008.

[74] S. Omata and T. Shimizu, *Study on an accurate calculation of the conducted EMI noise of the power converters*, 2014.

[75] A. K. Morya, M. C. Gardner, B. Anvari, *et al.*, "Wide bandgap devices in AC electric drives: Opportunities and challenges," *IEEE Transactions on Transportation Electrification*, vol. 5, no. 1, pp. 3–20, Mar. 2019.

[76] T. Liu, T. T. Y. Wong, and Z. J. Shen, "A survey on switching oscillations in power converters," *IEEE Journal of Emerging and Selected Topics in Power Electronics*, vol. 8, no. 1, pp. 893–908, Mar. 2020.

[77] C. Bi, R. Lu, and H. Li, "Prediction of electromagnetic interference noise in SiC MOSFET module," *IEEE Trans. Circuits Syst. Express Briefs*, vol. 66, no. 5, pp. 853–857, May 2019.

[78] T. Liu, R. Ning, T. T. Y. Wong, and Z. J. Shen, "Modeling and analysis of SiC MOSFET switching oscillations," *IEEE Journal of Emerging and Selected Topics in Power Electronics*, vol. 4, no. 3, pp. 747–756, Sep. 2016.

[79] K. Kim, H.-W. Shim, A. C. Scogna, and C. Hwang, "SMPS ringing noise modeling and managing methodology for RFI solutions in mobile platforms," *IEEE Trans. Compon. Packaging Manuf. Technol.*, vol. 8, no. 4, pp. 554–561, Apr. 2018.

[80] M. S. Nikoo, A. Jafari, N. Perera, and E. Matioli, "New insights on output capacitance losses in Wide-Band-Gap transistors," *IEEE Trans. Power Electron.*, vol. 35, no. 7, pp. 6663–6667, Jul. 2020.

[81] A. Raciti, S. A. Rizzo, N. Salerno, G. Susinni, R. Scollo, and A. Scuto, "Modeling the hysteresis power losses of the output parasitic capacitance in super junction MOSFETs," in *2018 International Symposium on Power Electronics, Electrical Drives, Automation and Motion (SPEEDAM)*, Jun. 2018, pp. 527–532.

[82] S. Franz, A.-R. Sam, and S. Ken, *Application note: 600 V CoolMOS™ C7 design guide*, Infineon Technologies, May 2015. [Online]. Available: `https://www.st.com/resource/en/application_note/an5252-lowvoltage-power-mosfet-switching-behavior-and-performance-evaluation-in-motor-control-application-topologies-stmicroelectronics.pdf`.

[83] *Application note: Low-voltage power MOSFET switching behavior and performance evaluation in motor control application topologies*, STMicroelectronics, Nov. 2018. [Online]. Available: `https://www.st.com/resource/en/application_note/an5252-lowvoltage-power-mosfet-switching-behavior-and-performance-evaluation-in-motor-control-application-topologies-stmicroelectronics.pdf`.

[84] M. S. Nikoo, A. Jafari, N. Perera, and E. Matioli, "Output capacitance losses in Wide-Band-Gap transistors: A Small-Signal modeling approach," in *2020 32nd International Symposium on Power Semiconductor Devices and ICs (ISPSD)*, Sep. 2020, pp. 190–193.

[85] J. Chen, X. Du, Q. Luo, X. Zhang, P. Sun, and L. Zhou, "A review of switching oscillations of wide bandgap semiconductor devices," *IEEE Trans. Power Electron.*, vol. 35, no. 12, pp. 13 182–13 199, Dec. 2020.

[86] J. Lautner and B. Piepenbreier, "Impact of current measurement on switching characterization of GaN transistors," in *2014 IEEE Workshop on Wide Bandgap Power Devices and Applications*, Oct. 2014, pp. 98–102.

[87] T. Shimizu, G. Kimura, and J. Hirose, "High frequency leakage current caused by the transistor module and its suppression technique," *IEEJ Transactions on Industry Applications*, vol. 116, no. 7, pp. 758–766, 1996.

[88] S. Wang and F. C. Lee, "Investigation of the transformation between Differential-Mode and Common-Mode noises in an EMI filter due to unbalance," *IEEE Trans. Electromagn. Compat.*, vol. 52, no. 3, pp. 578–587, Aug. 2010.

[89] E. Choi, S. Han, J. Lee, S. Kang, and J.-W. Choi, "Ber analysis of can under bpsk passband can-hd interference," in *2016 Eighth International Conference on Ubiquitous and Future Networks (ICUFN)*, 2016, pp. 178–180. DOI: 10.1109/ICUFN.2016.7537012.

[90] B. Shen, X. Zhou, and R. Wang, "Ber analysis for controller area network impaired by the impulse noise in cyber-physical systems," in *2014 IEEE International Conference on Computer and Information Technology*, 2014, pp. 425–429. DOI: 10.1109/CIT.2014.99.

[91] X. Jia, B. Dong, H. Wang, C. Hu, and D. Xu, "Characteristics of SiC inverter powertrains on common-mode EMI noise," *Journal of Power Electronics*, vol. 21, no. 2, pp. 354–363, Feb. 2021.

[92] M. J. Rogers, E. R. Motto, and M. Steiner, "Performance comparison of State-of-the-Art 300A/1700V si IGBT and SiC MOSFET power modules," *IEEE Power Electronics Magazine*, vol. 7, no. 3, pp. 44–51, Sep. 2020.

[93] L. Zhang, X. Yuan, X. Wu, C. Shi, J. Zhang, and Y. Zhang, "Performance evaluation of High-Power SiC MOSFET modules in comparison to si IGBT modules," *IEEE Trans. Power Electron.*, vol. 34, no. 2, pp. 1181–1196, Feb. 2019.

[94] A. Vukicevic, M. Rubinstein, F. Rachidi, and J.-L. Bermudez, "On the mechanisms of differential-mode to common-mode conversion in the broadband over power line (BPL) frequency band," in *2006 17th International Zurich Symposium on Electromagnetic Compatibility*, Feb. 2006, pp. 658–661.

[95] H. C. P. Dymond, J. Wang, D. Liu, *et al.*, "A 6.7-GHz active gate driver for GaN FETs to combat overshoot, ringing, and EMI," *IEEE Trans. Power Electron.*, vol. 33, no. 1, pp. 581–594, Jan. 2018.

[96] H. C. P. Dymond, D. Liu, J. Wang, J. J. O. Dalton, and B. H. Stark, *Multi-level active gate driver for SiC MOSFETs*, 2017.

[97] S. Mahmodicherati, N. Ganesan, L. Ravi, and R. Tallam, *Application of active gate driver in variable frequency drives*, 2018.

[98] *EiceDRIVER 1EDS-SRC family*, Infineon, Jan. 2020. [Online]. Available: https://www.dianyuan.com/upload/seminar/2019/10/10/1570687994-85942.pdf.

[99] L. Thompson, *Industrial Data Communications*, ser. Resources for Measurement and Control Series. ISA, 2008, ISBN: 9781934394243.

[100] D. Morris, *Communication for Command and Control Systems: International Series on Systems and Control*. Elsevier Science, 2014, ISBN: 9781483155197.

[101] "CAN bus error handling," [Online]. Available: `https://www.kvaser.com/about-can/the-can-protocol/can-error-handling/`.